Faculté des Sciences
Département de Physique

MAGNETOCAPILLARY SELF-ASSEMBLIES

Interfacial Locomotion at Low Reynolds Number

Dissertation présentée par
Galien Grosjean
en vue de l'obtention du titre de
Docteur en Sciences

Année académique 2018-2019

Cover image. – Magnetocapillary self-assembly rotating on a liquid bath. Black ink can be used to visualise the entrainment of fluid. Credits: Jean Louis Wertz.

Bottom right corners. – Deformation and motion of a triangular magnetocapillary swimmer. Flip the pages in order to see the motion. The images are spaced by one tenth of a second.

I would first like to give a heartfelt thank to each of the jury members for accepting to read my thesis and attend the defence. Thank you Pietro Tierno, Jens Harting, Thierry Bastin, Stéphane Dorbolo and Geoffroy Lumay, I hope it is as much a pleasure to read as it was to write.

Thank you to all scientists, young and old, who shared their thoughts and experience with me. Many a good idea was had between two pints in a pub, in an overcrowded airbnb or gathered around the fire of a barbecue. A special thanks to the groups of Ana-Sunčana Smith and Jens Harting at the FAU, to Alexander, Sebastian, Oleg, Thomas, Jayant, for the many fruitful discussions, even in the most remote locations.

Je souhaiterais remercier chaudement mon promoteur Nicolas Vandewalle, pour son soutien, sa sagesse et sa patience. Un chef aussi cool, c'est aussi rare qu'un Ardennais qui ne s'appelle pas Léonard.

Je n'aurais pas pû rêver mieux comme endroit que le GRASP pour faire une thèse, et c'est surtout parce qu'il est peuplé d'une foutue belle bande. Merci à Charlotte, grâce à qui ce manuscript contient un peu moin de fotes. Merci à Guillaume, qui a su m'apprendre les ficelles du métier avant de disparaître tragiquement dans la jungle. Merci à Maximouze pour son aide sur les équations du premier degré. Merci à Nick Darras pour le ronronnement de son frigo à deux balles. Merci à SN-Séba pour les devinettes et les fruits frais. Merci à Bori-san pour la destruction totale de mon système digestif. Merci à Josépine pour m'avoir foutu Gérard Lenorman en tête. Merci à Chouaib pour les bons légumes du jardin. Merci à l'Équipe Internationale d'Overcooked et à tous les membres de la Ligue de Bureau-Ball. Merci à tous les colocataires passés et présents du 3.15, avec qui j'ai vécu d'excellents moments et même parfois un peu travaillé, j'ai nommé Gloriane Weber Truscott, Martin Matin l'homme vert, la petite Bernadette Yloco et Antonellama Guanaco. Merci à l'autre vieux briscard du labo, Stéphane Drobloblo, dont le discernement n'a d'égal que la soif. De connaissance, j'entends. Merci au -1 et aux temps de midi bière spé. Un tout grand merci

aussi à Florampoule Lumignolet, au Schtroumpf Lumbago et à sa Chouffette, à Shocklien Jumelle, à Soso Tunisiano, au Christophe de 11h30, à Geoff Ça Roule, à Ricopsi, à RV, à Mim, à Jean-Dago, à Tauline Poussin, au Macochère, au Vigneron, à Zorba le Grec et à Salvaporc Pillipoutri. Merci à tous les bandits de l'atelier, DJ Soif, Mich-Mich, Oli, Sam, Alice et Praline.

Merci également à tous mes proches qui me soutiennent. Merci à mes chers parents pour l'ADN et tout le reste. Merci à mes frères et sœurs de ne pas me faire la bise. Merci à Zizal, Dr. Love et Fétus pour les madriers de 6 m bien droits. Merci aux astros et matérialistes sympas et à toute la promo 2014, Jude, Clem, Oli, Joseph, Lyne, Martin, Élo, Alain, Antoine, Lulu, Marie-Ju, Florence et j'en oublie sûrement. Merci au Prince de la Fête, à l'officier Puertoricano, à Riton, à Loubite, à Martinez, à Sully et à Brice. Merci à Kéké pour la pédale, à Robite pour les tomates et à Rav-4 pour le plancher du salon. Merci à la Coach de m'avoir prêté son couloir. Merci à Smyggy les Bons Tuyaux et à tonton Jean-No. Merci à Antoine Clinquart pour le covoiturage. Merci aux anciens de Bernardfagne, Kef-Kef, Vic, Réglisse et compagnie. Merci à ma pote Liv Tyler, tu es le contraire d'une assiette de petits pois-carottes. Merci à EVR, à Silent Cat, à toute la Meubite, aux Gils, au Que Calor. Et doublement merci à ceux que j'ai oublié!

Cordialement,
Papa Gâteau Mbappé
Le Boulanger
Vésuve

Abstract

Magnetocapillary self-assemblies form when soft-ferromagnetic particles are deposited on a liquid surface under an induction field. They emerge from the competition of a magnetic dipolar interaction and the Cheerios effect, an attractive force due to the deformation of the meniscus. Under dynamic fields, these self-assembled structures swim along the interface. Due to their conceptual simplicity, they allow to verify and expand our general knowledge of microswimmers. Different arrangements of particles can be built with different goals in mind: from simple one-dimensional swimmers to complex bio-inspired structures; from fast, controllable swimmers to cargo transporters and fluid mixers.

RÉSUMÉ

Les auto-assemblages magnétocapillaires se forment lorsque des particules ferromagnétiques douces sont déposées sur la surface d'un liquide et soumises à un champ d'induction. Ils émergent de la compétition entre une interaction dipolaire magnétique et l'effet Cheerios, une force attractive due à la déformation du ménisque. Sous des champs variables, ces structures auto-assemblées nagent le long de l'interface. Grâce à leur simplicité conceptuelle, ils permettent de vérifier et d'étendre notre compréhension générale des micronageurs. Différents arrangements de particules peuvent être réalisés dans le but d'accomplir divers objectifs : du plus simple nageur unidimensionel à la plus complexe structure inspirée du vivant ; d'un nageur rapide et contrôlable à un transporteur de cargaison ou mélangeur de fluides.

TABLE OF CONTENTS

1 Introduction

Why do sperm cells have flagella and not fins? Macroscopic and microscopic swimmers visibly differ in their locomotion mechanisms. The fish and the flagellated protozoa depicted in Fig. 1.1 both swim in water, so why are their swimming strategies so different?

Will we ever be able to navigate inside the human body to destroy tumours or blood clots? Since Richard Fleischer's 1966 movie The Fantastic Voyage, and its novelisation by Isaac Asimov, science-fiction authors have been fascinated by the idea of meandering through blood vessels, the inner ear or even the brain, to treat various disorders, perform microsurgery or deliver drugs locally. Shrink rays are obviously a physical impossibility. But if we were to build a tiny unmanned *Proteus*, what kind of propulsion would she use?

Speaking of building microscopic submarines, how could we assemble such tiny components with macroscopic tools? Despite constant innovation in microfabrication techniques, complex structures are still technologically challenging, if even possible. Even something as trivial as a football requires many parts to be precisely put together in the right order, 12 pentagons and 20 hexagons for the emblematic truncated icosahedron. Figure 1.2 contrasts this labour-intensive process with the self-assembly of an icosahedron from proteins and a polyelectrolyte. This process is an important step in the formation of some viruses and macrophages [1, 2].

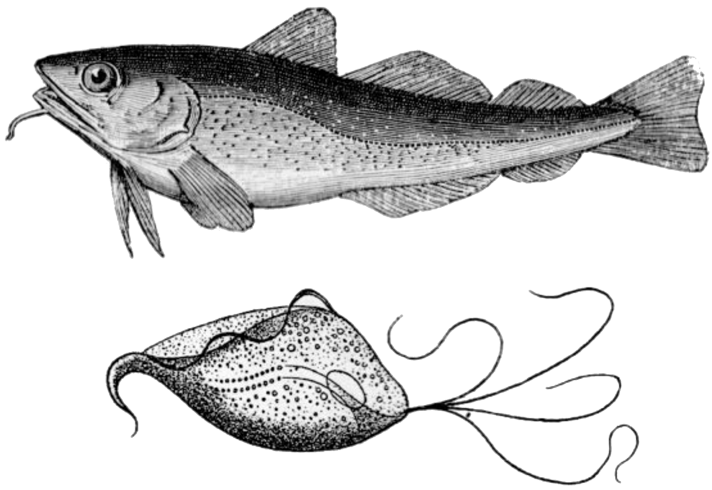

Fig. 1.1 Swimming strategies. – On top, the common cod (*Gadus morhua*) has a typical size of 1 m and swims in an inertia-dominated regime. Below, the protist *Trichomonas* is approximately 10 µm in length. It swims in a viscosity-dominated regime using several flagella and an undulating membrane called axostyle. Adapted from [3].

Could we not learn from the intricate structures that form in nature at even the smallest scales?

These questions embody some of the motivations behind the study of microswimmers. In microscopic flows, viscous dissipations dominate over inertia. However, swimming in a viscosity-dominated regime is far from a trivial task. Any attempt at coasting is instantaneously lost to friction. Microbes and microrobots must develop specific strategies, with a strict necessary condition: breaking time reversibility [4]. In other words, their succession of adopted configurations must be oriented in time. But assembling microscopic moving parts to form a structure with multiple independent degrees of freedom is challenging. Hence, a system able to build itself from independent components is enticing. A structure that spontaneously breaks time reversibility even more.

Fig. 1.2 Assembling polyhedra. – On top, Pakistani man stitching pentagons and hexagons in a truncated icosahedron pattern to form a football [5]. Below, coarse-grained simulation of the self-assembly of an icosahedral viral capside, typically 10 nm in diameter, adapted from [2].

This kind of spontaneous arrangement into ordered structures is called self-assembly. It emerges from specific and reversible interactions between individual components [6]. In this thesis, steel spheres floating on water self-assemble thanks to the magnetocapillary interaction. As the name implies, it combines a capillary force with a controllable magnetic force. More specifically, the deformation of the interface surrounding floating objects can cause lateral forces to appear. This explains why breakfast cereals tend to cluster in a bowl of milk, and was therefore nicknamed the Cheerios effect [7]. Similarly, floating steel spheres form disorganised aggregates. To obtain reversible and controllable self-assembly, a second force is required, a magnetic dipole-dipole interaction. Under a magnetic induction field, the particles magnetise. They behave like soft magnets, which means that the direction and intensity of the magnetisation are imposed by the external field. The combined effect of these two forces can

lead to the formation of small two-dimensional crystals, whose geometry and size are a function of the external field [8, 9].

These crystal-like assemblies of particles can be submitted to dynamic magnetic fields, allowing to probe the complex energy landscape of the magnetocapillary interaction. This causes oscillations that can break time-reversal symmetry, leading to locomotion along the interface [10]. This work will attempt to answer interrogations about the physics of these assemblies, from the process of their formation to the emergence of locomotion. There is a lot to uncover in order to fully grasp these mechanisms, however this is a necessary step in order to control these tiny swimmers. It is also crucial to place this system in the general framework of microswimmers, from the most fundamental aspects to the study of possible future applications. This thesis will therefore proceed with a discussion of microswimmers in general, with a particular emphasis on the possible role that interfaces can play. The following chapter will then introduce magnetocapillary self-assemblies under static magnetic fields. The remaining chapters will study the dynamics of these assemblies in a variety of configurations.

2 Research Context

This chapter presents an overview of the literature and introduces the concepts that will be necessary throughout this thesis. We first discuss the generalities of locomotion in a fluid at low Reynolds number. Microscopic swimmers such as bacteria and sperm cells move in a regime where viscous dissipation dominates over inertia, a fact that dictates their methods of locomotion. We then review some of the possible implications of the presence of an interface. In particular, a variety of systems that make use of interfacial phenomena to self-propel are presented and discussed.

Partially published as

- G. Grosjean, M. Hubert, Y. Collard, S. Pillitteri, N. Vandewalle, Eur. Phys. J. E (in press)

2.1 Scallops, Interfaces and Symmetry

2.1.1 Swimming in the Bulk

We generally have a good enough intuition about what it means to swim in a fluid at our scale. Water is pushed away in a given direction, and motion ensues in the opposite direction by conservation of momentum [12]. Sustain the motion by repeating this periodically and we obtain a working swimming strategy. However, as is often the case in nature, the physics of swimming is highly influenced by the relevant length and time scales [4, 12, 13]. Consider the general case of a body that is able to actively deform, moving in an infinite fluid volume. The conservation of momentum at each point in the fluid is described by the Navier-Stokes equation [14, 15] which, for an incompressible fluid, submitted to gravity, of density ρ_l and kinematic viscosity ν, reads

$$\frac{\partial \vec{u}}{\partial t} + \vec{u} \cdot \nabla \vec{u} = -\frac{1}{\rho_l} \nabla p + \nu \nabla^2 \vec{u} + \vec{g}. \tag{2.1}$$

This equation must be completed with the continuity equation $\nabla \cdot \vec{u} = 0$ and with the appropriate boundary conditions, taking into account the position at all times of the surface of the deformable body. For example, no-slip boundary conditions stipulate that $\vec{u}_{\text{fluid}} = \vec{u}_{\text{body}}$ at each point on the surface of the body.

It is often appropriate to compare the magnitude of the various terms in Eq. (2.1), in order to identify the relevant effects and provide some simplification. Let L and U be a typical length and a typical speed of the flow, respectively. For example, this could be the body length and speed of the swimmer, although it is sometimes more useful to look at the dimensions associated with what is producing the flow, like a beating fin or a rotating flagellum. The left member of Eq. (2.1) represents inertial forces and contains the unsteady term $\partial \vec{u}/\partial t$ and the advection term $\vec{u} \cdot \nabla \vec{u}$. Both terms

have the units of U^2/L. The viscous forces per unit mass $\nu\nabla^2\vec{u}$ scale like $\nu U/L^2$. Therefore, the ratio of inertial and viscous forces in the flow is given by the Reynolds number

$$\mathrm{Re} = \frac{UL}{\nu} \tag{2.2}$$

[16, 17]. This means that, for a given liquid, viscous forces tend to dominate over inertia at small scales. Water has a kinematic viscosity of about $\nu = 10^{-6}\,\mathrm{m^2\,s^{-1}}$, so that for a swimmer moving at one body length per second, *i.e.* $L/U = 1$ s, we would have $\mathrm{Re} < 1$ for $L < 1$ cm.

For Reynolds numbers close to zero, the left member of Eq. (2.1) can be neglected. This leads to the Stokes equation

$$-\frac{1}{\rho_l}\nabla p + \nu\nabla^2\vec{u} + \vec{g} = 0 \tag{2.3}$$

which is linear and independent of time. This has some serious consequences on the swimming mechanisms of microorganisms [4, 13]. The fact that time does not intervene in the Stokes equation means that flows are typically reversible and rate independent. Let a body composed of two segments linked by a hinge, as shown in Fig. 2.1 (i). The opening angle between the segments is the only degree of freedom. At high Reynolds number, this simple structure can swim by rapidly closing, expelling water, and then reopening slowly. This is a swimming strategy similar to what some scallops do, with valves in place of the segments, except that the water is expelled through small openings on either side of the hinge. However, the rate of closing and opening does not influence the flow in the Stokes regime, meaning that only the succession of geometric configurations adopted by the swimmer matters. With only one degree of freedom, our model scallop can only go back and forth between the open and close configurations. Even if water is pushed during the closing phase, it will always produce the inverse flow by reopening, so that the centre of mass is not displaced over one period.

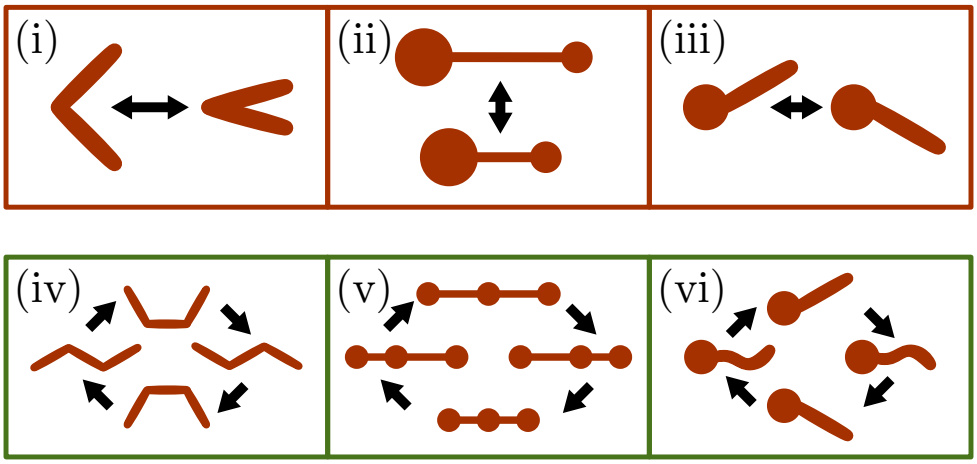

Fig. 2.1 Swimming strategies. – On top, reciprocal swimmers. This includes (i) a scallop-like swimmer [4], (ii) two oscillating spheres of different sizes [18], and (iii) a body with a rigid beating tail [19]. **Below, non-time-reversible swimmers.** The three-link swimmer (iv) has two hinges that move out of phase [4]. The two arms of the three-linked-spheres swimmer (v) also oscillate out of phase [23]. A deformable body such as a flexible magnetic tail (vi) can also produce a non-reciprocal motion [24].

This leads to what is colloquially known as the "scallop theorem", stating that, at Re = 0, if the succession of configurations adopted by the swimmer is unchanged by a time-reversal transformation, then it cannot produce a net motion [4]. Several other swimming strategies that have been proven to work at higher Reynolds number will fail for the same reasons. For instance, two spheres of different sizes linked by an oscillating spring, as shown in Fig. 2.1 (ii), would not be able to swim in the Stokes regime, as there is only one degree of freedom for deformation. Such a swimmer has been shown to produce virtually no net motion under a critical value for the Reynolds number, at around Re $\approx$ 20 [18]. Similarly, a beating rigid tail, shown in Fig. 2.1 (iii), can produce no net motion if the Reynolds number is smaller than unity [19]. Depending on the particular case, the onset of a net motion

for a reciprocal swimmer, following an increase in the Reynolds number, can occur either continuously or discontinuously [20].

Another way to discuss the implications of Eq. (2.3) is to consider that a swimmer, in the Stokes regime, is incapable of exerting a net force, or conversely, a net torque, on the surrounding fluid [13]. Indeed, considering that inertia is negligible when $\mathrm{Re} \approx 0$ is equivalent to stating that the swimmer experiences a resultant force from the fluid equal to zero at all times, granted that there is no external force pushing the swimmer. If the flow field around the swimmer is expressed as a multipole expansion, the term decaying like $1/r$, which corresponds to a point force and is called a stokeslet, is therefore zero. The leading term in the far-field flow is thus a symmetric force dipole at best, *i.e.* the flow generated by two opposite point forces, which decays like $1/r^2$. This is called a stresslet and is a useful tool for describing in general terms the motion of a microswimmer and its interactions with its environment [13, 21, 22]. In general, a swimmer generates a flow that is a combination of stresslets and higher order terms, such as the source dipole, whose velocity field decays like $1/r^3$.

For decades now, researchers have come up with swimming strategies that satisfy the conditions imposed by the scallop theorem [4, 13, 23, 24, 27, 28]. Such strategies already exist in nature and are used by motile bacteria and sperm cells. This includes the rotation of one or several helical flagella [4], the sequential motion of a series of cilia [13] or the transfer of mass by deformation of the whole cell membrane [29]. However, it is possible to devise strategies that are conceptually simpler, more adapted to analytical calculations or numerical simulations, and/or easier to implement experimentally with existing technologies. One early example, proposed by Purcell in 1976 [4], is the addition of one degree of freedom in the scallop-like system from Fig. 2.1 (i), which is now composed of two hinges and three segments, the so-called three-link swimmer, as shown in Fig. 2.1 (iv). This allows to move the external arms one after the other, lead-

ing to a sequence of configurations that is not time-reversible. As shown, the sequence leads to a net motion to the right. This is easier to understand when picturing this swimmer as standing on a sinusoidal wave travelling to the left, where every configuration change moves the wave by a quarter wavelength. Experimental implementations of this swimmer have been made, though they require macroscopic elements such as motors.

An arguably simpler, one-dimensional deformation sequence has been proposed by Najafi and Golestanian in 2004 [23]. Like the swimmer from Fig. 2.1 (ii), it consists of spheres linked by arms whose length can vary. In order to beat the scallop theorem, a minimum of three spheres and two independent arms is required. The sequence as depicted in Fig. 2.1 (v) leads to a net motion to the right. A lot of theoretical work has been based on this swimmer, sometimes using oscillating springs instead of arms [30–34]. This can be attributed in part to its one-dimensional nature which greatly facilitates analytical calculations. Notably, it can be shown that the speed of this swimmer over one period is proportional to the area of the cycle drawn by the swimmer in the plane defined by the two arms' lengths [30]. If the arms oscillate harmonically at a frequency ω, this can be expressed as the product of the amplitudes of oscillations of each spring with the sine of their phase difference ϕ, namely

$$V = \alpha A_a A_b \omega \sin\left(\phi\right) = \alpha \mathscr{W}, \tag{2.4}$$

where α is a geometrical prefactor with units m^{-1} that can be determined analytically, and we defined swimming efficiency $\mathscr{W}$.

Despite its simplicity, the three-linked-spheres swimmer is far from being the first to have been implemented experimentally. This honour goes to the work by Dreyfus *et al.* in 2005, which is often regarded as the first artificial microswimmer [24]. A magnetic tail, composed of superparamagnetic colloids linked by DNA strands, is attached to a red blood cell. In an oscillating magnetic field, the tail deforms and aligns itself periodi-

cally with the field, following a non-time-reversible sequence illustrated in Fig. 2.1 (vi).

2.1.2 Beyond the Scallop Theorem

While the scallop theorem has been the basis for many studies, there are several cases where it is not applicable. For instance, the independence in the rate of deformation of the body is only valid in a Newtonian fluid. In a shear thinning or shear thickening fluid, for example, the change in apparent viscosity can be used to produce a net displacement with a reciprocal motion [35, 36].

The proximity of another body can also be used to relax the condition imposed by the scallop theorem. For instance, two out-of-phase reciprocal swimmers can essentially act as one non-reciprocal swimmer [37]. A nearby interface, which is a common scenario in biological fluids or microfluidic devices, can also be used to beat the scallop theorem. In their 2008 paper, Trouilloud *et al.* studied the flow induced by a reciprocal swimmer near an interface, by looking at the flow in the far field as a superposition of stresslets and source dipoles [21]. In this case, while the proximity of a rigid wall can induce an additional velocity component, it does not allow to overcome the scallop theorem. However, a reciprocal swimmer can move when the interface in question is deformable, such as the interface between two fluids, or between a fluid and a deformable solid, like a membrane or a gel (see Fig. 2.2 (i)). Swimming is possible towards, away and parallel to the interface, depending on the stresslets and source dipoles considered. To generate a significant motion, the swimmer must be able to generate an important enough deformation of the interface. The swimmer exerts a typical viscous force ηUL on the interface, where L represents both the swimmer size and its distance to the interface, which must be compared to a typical restoring force, such as a capillary force γL in the case of an interface between two fluids. In this case, one obtains the capillary number

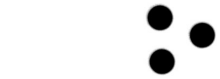

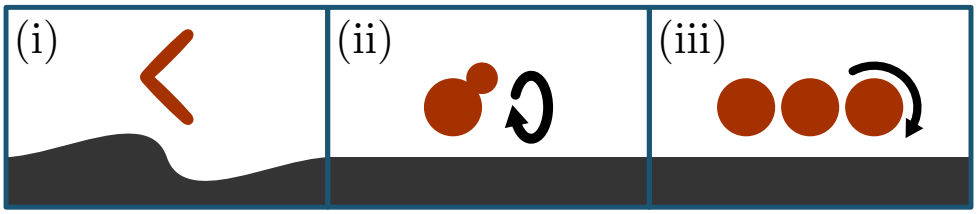

Fig. 2.2 Swimming strategies near a surface. – A reciprocal swimmer (i) can move in all directions when close to a deformable interface [21]. Two stacked spheres in a precession movement (ii) can move with an interface nearby [25]. Rotating spheres can also move close to an interface (iii), where they self-assemble into a colloidal conveyor belt under a combination of rotating and oscillating fields [26].

$\eta U/\gamma$ which must be larger than unity while keeping the Reynolds number small. This leads to a typical length scale $\eta^2/\rho_l\gamma$, the Ohnesorge length, under which this kind of propulsion is effective. In the case of water, we have $\eta^2/\rho_l\gamma \approx 14\,\text{nm}$. Note that for simplicity, two fluids of similar viscosity and density were considered.

While a deformable interface is required in the work by Trouilloud *et al.*, it is possible to generate motion parallel to a rigid interface with reciprocal motion. In experiments performed by Tierno *et al.*, a small paramagnetic sphere is attached to a larger one [25, 27, 38]. The doublet is then submitted to a precessing magnetic field, as illustrated in Fig. 2.2 (ii). Motion is induced in a direction perpendicular to the precession axis and parallel to the wall. Here, the presence of the wall creates a difference in viscous dissipation between each part of the rotation, far and close to the interface. Indeed, the "return stroke" experiences a lower viscous dissipation than the "forwards stroke", which is closer to the interface. This could be compared with the previously discussed reciprocal motion in a non-Newtonian fluid, except that the modulation in viscous dissipation is due to the proximity of the interface, and not the fluid itself. This asymmetry explains the apparition of a net motion that would not be observed in the bulk.

Similarly, a simple rotational motion in a plane perpendicular to a nearby interface can lead to propulsion, as the flows below and above the rotating body differ. On the other hand, several magnetic colloids rotating in a plane parallel to the interface can self-assemble into a two-dimensional colloidal carpet, as the time-averaged dipole-dipole interaction between the spheres is an attraction. By combining the two effects, it is possible to generate a colloidal carpet that moves along the interface [26]. This is illustrated in Fig. 2.2 (iii). The speed of the carpet increases with the number of particles and saturates around $N \approx 300$. This structure can work as a conveyor belt able to transport a cargo.

2.2 Swimming at the Interface

In the previous section, we discussed how the breaking of spatial symmetry provided by a nearby interface can allow to beat the scallop theorem. We will now show that interfacial phenomena, such as the Marangoni effect or surface waves, can also be used to generate microswimmers. The magnetocapillary swimmer that constitutes the bulk of this thesis falls in this category.

2.2.1 Autophoresis

In the scallop-theorem paradigm, it is assumed that the self-propulsion of the swimmer is achieved through the deformations of the body. However, it is also possible for a rigid body to achieve a force-free self-propulsion through a self-generated gradient. This is the basic principle behind autophoretic (self-phoretic) swimmers, which induce flows on their surface through gradients in concentration, temperature or electrostatic potential [46]. For example, self-diffusiophoresis can arise when a particle is partially covered with a catalyst for a chemical reaction that can occur in the surrounding fluid, locally creating a gradient in concentration [47, 48].

The asymmetry is not necessarily required, as a symmetry breaking can also spontaneously occur with isotropic particles [49]. The process is similar with self-thermophoresis [50] or self-electrophoresis [51].

Recently, it has been proposed to study the motion of self-diffusiophoretic swimmers trapped at interfaces [52–55]. This has the effect to reduce their rotational diffusion and therefore increase their persistence length and sometimes speed [52]. Spherical Janus colloids, composed of SiO_2 and partially coated with platinum, are deposited on the surface of a water and H_2O_2 mixture. The decomposition of H_2O_2 is catalysed on the Pt-coated region, causing the particles to move, with a speed that depends on the quantity of available "fuel", *i.e.* the concentration in H_2O_2. The experiment can also be performed at an oil-water interface, with similar results [54, 56]. Structures that typically form on interfaces, such as colloidal crystals, can provide additional confinement [55]. The presence of a nearby interface could also cause spherically symmetric particles to move thanks to a breaking of symmetry [57, 58]. In a sense, this is similar to the mechanisms discussed in Fig. 2.2, where the nearby interface allows to overcome the scallop theorem. Here, the chemical reaction occurring around the spherical swimmer generates Marangoni flows, causing a net motion that could, in theory, dominate over classical autophoresis [58].

2.2.2 Marangoni Effect

The principle of a self-generated gradient is also used for motion along an interface, in the case of propulsion by Marangoni effect. The camphor boat, which has been known for more than a century, is now used as a model system for low Reynolds locomotion [39, 59]. A piece of camphor is attached to a floating object. When it dissolves in the water, the camphor molecules adsorbed at the water surface locally lower surface tension, as illustrated in Fig. 2.3 (i). The resulting surface tension gradient propels the object forwards. While the camphor boat is the earliest and most well-

known example of propulsion by Marangoni effect, it is far from being the only one. For example, a body releasing a solvent in the surrounding liquid can generate a gradient in surface tension, as represented in Fig. 2.3 (ii). Examples of bodies placed on a water bath include a gel disk soaked in oxolane (tetrahydrofuran) [60] or ethanol [40], a droplet of aqueous ethanol coated with colloidal particles, called a liquid marble [41], and a soap disk at an oil-water interface [61]. This effect has also been observed with pure water droplets placed on an oil-surfactant bath [62]. Note that these objects can be isotropic, as any small anisotropy due to the initial conditions can increase when the object starts to move.

A variation on this principle is to generate a surface tension gradient by locally heating the fluid, for example by illuminating an object with intense light. This is illustrated in Fig. 2.3 (iii), where a light-absorbing element is placed at the back of an object heated with focused light [42]. Using a laser as heat source makes it possible to move isotropic objects such as steel spheres, as it allows light to hit the surface at a precise point [63]. Finally, stationary heated structures on a chip suspended above the surface can generate many types of behaviours by using point, line, annular or triangular heat sources [64].

2.2.3 Surface Waves

Another type of interfacial phenomenon that can be used for propulsion is surface waves. For instance, one can use Faraday waves, *i.e.* standing waves that appear on a vibrating bath, for locomotion. A famous example is the case of walking droplets, where an oil droplet bouncing on a vibrating bath, just below the onset of the Faraday instability, is pushed forwards as it falls on the slope of the wave that it triggers [65]. This does not technically qualify as swimming, as the droplet is never immersed in the bath.

It is possible, however, to produce a swimmer by using a similar system [43]. In this case, a water droplet is placed on a vibrating bath of silicon

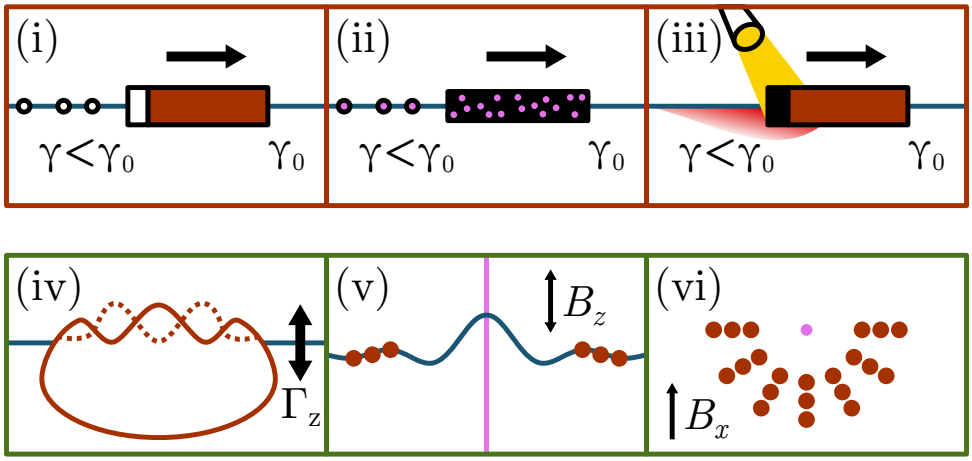

Fig. 2.3 Surface-bound swimmers. – On top, using surface tension gradients. In the classic camphor boat (i), surface tension is locally lowered by a piece of camphor dissolving at the stern [39]. Marangoni-driven propulsion can also be obtained by releasing a solvent (ii) contained in a gel [40] or in a droplet coated with colloids [41]. Note that motion can arise even with symmetric objects, as a spontaneous breaking of symmetry can be observed. The gradient in surface tension can also come from a temperature change (iii), for instance using a light source [42]. **Below, using surface waves.** A droplet placed on a vertically vibrating bath can be deformed by a Faraday standing wave (iv), leading to a net motion after a symmetry breaking in the position of the nodes [43]. Magnetic colloids (v) can also generate surface waves under a vertical oscillating field [44]. The particles arrange to form an aster (vi), which can swim if the spatial symmetry is broken [45].

oil. The droplet is mostly immersed, with a small cap peaking above the surface of the bath. Under a strong enough acceleration of vibration $\Gamma_z = A\omega^2$, a Faraday standing wave can appear on the surface of the water droplet, as depicted in Fig. 2.3 (iv). This generates a flow in the surrounding oil that can lead to motion. Depending on the forcing parameters, several types of motions are observed, including spinning, rotation on an orbit, zig-zag and translational motion. This is linked to the number and positions the standing wave nodes on the droplet. Indeed, if the nodes are in a straight line, the droplet is either stationary or spinning. Conversely, for some values of

the forcing parameters, a symmetry breaking in the position of the nodes can spontaneously appear, leading to a net motion. The Reynolds number for this system is typically around 0.1. With a less viscous bath, and thus a higher Reynolds numbers of around 10, another type of motion can be observed. In this case, the wave on the droplet is a travelling wave, leading to locomotion in the opposite direction. This resembles the squirming model for microswimmers, where a sphere deforms its surface to generate a flow, similarly to what is observed with some bacteria such as ciliates [66].

In a second example, ferromagnetic particles floating on water can produce waves when submitted to a vertical oscillating field B_z. Indeed, while the interaction between vertical dipoles on the surface is repulsive, nearby particles can form chains with a resulting moment in the plane of the interface. These chains can deform the interface as they try to align themselves with the vertical field, which leads to the formation of self-organised structures, such as "snakes" [44] and asters [45]. A side view of an aster is depicted in Fig. 2.3 (v). The colloidal chains stand on the slope of the standing wave they produce. The addition of a constant horizontal field B_x can break the circular symmetry of the aster, as shown in Fig. 2.3 (vi). The asymmetric aster generates a net fluid flow, leading to locomotion. Note that, while the particles have a typical size of 90 µm, inertia is not negligible in the flow, as the Reynolds number is of the order of 10.

2.2.4 Surface Effects at Larger Scales

While the systems described in this chapter mainly belong to the realm of low-Reynolds-number flows, it should be noted that interfacial effects are typically relevant up to the centimeter scale. In fact, the capillary length $l_c = \sqrt{\gamma/\rho_l g}$, below which surface tension dominates over gravity, is around 2.7 mm in water. This explains why some insects and other invertebrates rely on surface forces for propulsion. For instance, some small animals can ascend a meniscus by deforming the interface [68]. Water

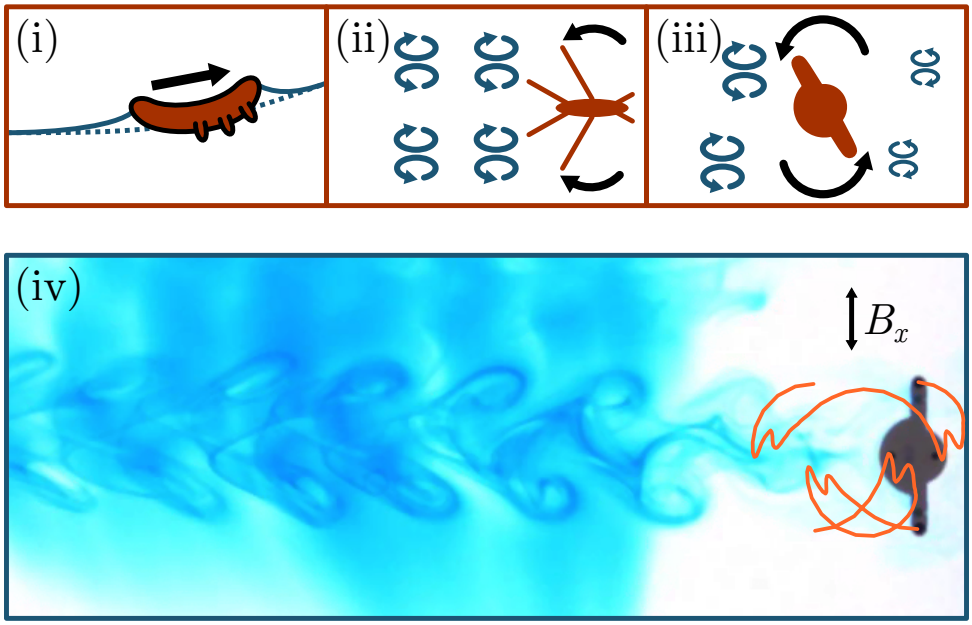

Fig. 2.4 Exemples of centimeter-scale surface locomotion. – The larva of the waterlily leaf beetle (i) can move upwards a meniscus by deforming to generate a Cheerios effect. Water striders (ii) float and propel vortices thanks to their hydrophobic legs [67]. A simple surface swimmer (iii) composed of two arms and an asymmetric body can swim by expelling vortices. There is a net motion to the right thanks to the asymmetry in momentum transfer to the fluid. Experimentally (iv), the oscillation of the piece is achieved thanks to embedded magnets in the arms and an external oscillating field.

treaders, a semiaquatic insect, achieve this by pulling the interface upwards with their legs. Because the interface is sloped, the resultant capillary force on the insect's legs has a horizontal component. This lateral capillary force is known as the Cheerios effect [7] and will be further discussed in the following chapter. Alternatively, some terrestrial insects such as beetle larvae can bend their whole body to generate the same effect, allowing them to reach land after an unintended fall onto water. Figure 2.4 (i) depicts a beetle larva climbing a meniscus. Millimeter-long nematodes, also called

roundworms, have been shown to not only climb a meniscus, but aggregate and remain grouped together thanks to the Cheerios effect [69].

Other invertebrates, such as water striders [67] and fisher spiders [70], float on water thanks to surface tension. They use their hydrophobic legs to transfer momentum to the liquid by generating U-shaped vortex rings attached to the interface, as represented in Fig. 2.4 (ii). This type of locomotion relies on a higher Reynolds number, typically around 100 or more [67]. To achieve this, water striders possess three pairs of legs that secrete a hydrophobic wax. They are covered with microscopic needles, called setae, which themselves are marked with a multitude of nanogrooves [71]. Only the middle pair of legs is used for propulsion. This motion resembles rowing, as the return stroke happens outside of water. In addition, some aquatic insects such as riffle bugs, smaller relatives of the water striders, can secrete surfactants to move by Marangoni effect [72]. This is based on the same principle that was depicted in Fig. 2.3 (ii). It generates a fast motion that is used as an escape mechanism.

It is possible to design artificial surface swimmers based on similar mechanisms. For instance, artificial water striders have been built using an elastic thread [67], piezoelectric actuators [73] or small dc motors [74] to power the legs. A larger number of supporting legs can allow such robots to support heavier loads [73, 74]. Using 3D-printing technology, we can design a very simple structure that captures the basics of this swimming strategy, *i.e.* floating on water and transferring momentum to the fluid by producing vortices. This swimmer is composed of a body that has the shape of a disk, with a pair of arms attached, as shown in Fig. 2.4 (iii). Thanks to the interface, the oscillation of the piece is constrained in a plane. Without the interface, the piece would most likely flip around the principal axis with the smallest moment of inertia, which is along the length of the arms. To generate propulsion, the fore-aft symmetry of the piece must be broken. Therefore, the central disk has a small radius on one side (fore) and a larger

radius on the other (aft). In the example shown in Fig. 2.4 (iv), the arm reach of the piece is 2 cm and the radii of the body are 0.35 cm (fore) and 0.50 cm (aft). When this object oscillates, it can generate vortex half-rings on each side. Thanks to the geometric asymmetry of the piece, the expulsion of vortices itself is asymmetric. This leads to a net motion of about 1.8 cm per period of oscillation. Figure 2.4 (iv) shows the trail left by such a swimmer in coloured water. One can see the rather large vortices on the side with the larger radius (aft).

In practice, a permanent magnet is embedded in each arm, oriented perpendicular to it. The oscillation of the piece is powered by a magnetic field oscillating parallel to the interface which creates a time-dependent torque. The field is sinusoidal, of amplitude 2.8 mT and frequency 0.5 Hz and oscillates perpendicular to the swimming direction. A small offset of 0.28 mT is added perpendicular to the oscillation, which prevents the piece from performing a full turn. Figure 2.4 (iv) also shows the trajectory of the arms' ends over one period of oscillation. One can see that the piece swings back and forth between $-\pi$ and π radians.

The Reynolds number of this system is typically of a few hundreds. Another useful dimensionless number to describe vortex shedding is the Strouhal number, often written $\mathrm{St} = Af/U$ where A is the stroke amplitude, f its frequency and U is the swimming speed [75, 76]. In the case of undulatory propulsion of fish, the optimal Strouhal number has been theoretically predicted, and ranges between 0.15 for large animals like cetaceans up to 0.8 for small animals such as tadpoles [77]. An oscillating piece like the one in Fig. 2.4 (iv) has a Strouhal number of about 0.55, suggesting that vortex shedding is the relevant swimming mechanism. This type of swimmer could be optimised for efficiency by varying the geometrical parameters as well as the applied field. This could provide a model structure to study the laws that govern biolocomotion, as well as a basic element to construct untethered swimming robots.

2.3 Summary

Swimming at low Reynolds number, in the absence of inertia, is far from a trivial task. Microswimmers must develop strategies that break time-reversal symmetry, as the flows themselves are time-independent. Many strategies either already exist in nature, have been engineered in the hope of developing biomedical or industrial applications, or have been theorised to study the particular physics of microswimmers.

The presence of an interface can be beneficial to the locomotion. Indeed, it can allow the necessary breaking of symmetry, provide forces that are inexistant in the bulk, or geometrically constrain the system, causing motions that might not be allowed otherwise. Mesoscale animals, larger than microswimmers but still dominated by surface forces, have developed a rich panel of strategies that make use of interfacial physics for locomotion. This intermediate scale is seldom explored and potentially offers some interesting physics, as demonstrated by the fabrication of a small oscillating piece that swims by vortex shedding.

The type of swimmer that will be the main focus of this thesis, the magnetocapillary swimmer, also takes advantage of surface effects. Floating particles are surrounded by a meniscus whose slope can cause lateral forces to appear. This so-called Cheerios effect, combined with a magnetic dipole-dipole force, leads to the spontaneous and reversible formation of organised structures. This kind of autonomous formation process, the first step towards magnetocapillary swimmers, is called self-assembly.

3 Magnetocapillary Self-Assemblies

This chapter will briefly introduce the notion of self-assembly, then discuss the forces at the origin of magnetocapillary self-assemblies. These forces are a lateral capillary force, known as the Cheerios effect, and an interaction between magnetic dipoles. The basic experimental setup is also introduced. Finally, some characteristics of magnetocapillary self-assemblies under static fields are discussed.

Partially published as

- G. Grosjean, M. Hubert, N. Vandewalle, Adv. Colloid Interface Sci. **255**, 84 (2018)

3.1 Self-Assembly

Self-assembly is often used in a rather vague way to label any sort of process where order spontaneously emerges from disorganised elements. However, in order to fully grasp the interest of self-assembled systems, which spans from microfabrication to the study of living processes, a more restricted definition is necessary [6]. The formation of a structure should therefore be qualified as self-assembly if it fulfils the three following conditions. First, self-assembly must be reversible. For instance, molecules forming covalent bonds do not qualify [79]. Secondly, self-assembly must come from separate components. For example, fluid instabilities should not, in general, be considered to be self-assemblies. However, instabilities can be used to form self-assemblies, such as when evaporating a solution leaves behind particles in well-organised structures [80]. Finally, self-assembly must be somewhat controllable or, at the very least, result in structures whose characteristics are governed by the individual properties of the components. For example, the formation of the Solar System is sometimes naively given as an example of self-assembly, but the end result is solely a function of the position and movement of the initial molecular cloud. On the other hand, the self-assembly of certain viruses is dictated by the precise non-covalent interactions between a specific RNA branch and proteins, which can lead to a variety of shapes from spiral rods [81] to icosahedra [1].

As a way of simplifying the handling of microscopic objects, self-assembly has been intensely studied in recent years [82–86]. In particular, supramolecular self-assembly has allowed to undertake an impressive number of complex tasks in microfluidic and nanofluidic systems, including low-Reynolds-number mixing [87], drug delivery [88], assay of drugs [89], microfabrication [90], cargo transport [91], photonics [92] or sensoring [93]. The particular system discussed in this thesis uses magnetic spheres suspended at an interface to form reversible clusters called magnetocapillary

self-assemblies [8, 9]. These assemblies differ from other magnetic floating crystals [94–96] in that they can form outside of a confining potential. These particles experience a pairwise lateral capillary attractive force [7, 97] as well as a magnetic dipole-dipole repulsive force. The latter allows to tune the size and shape of the assemblies. The resulting interaction potential resembles the Derjaguin-Landau-Verwey-Overbeek (DLVO) potential used in colloidal science and adsorption, with a primary minimum corresponding to the generally irreversible contact between the particles, and a secondary minimum corresponding to an equilibrium distance where the particles can be reversibly trapped [8].

3.1.1 Lateral Capillary Force

Particles floating at an interface can interact and form aggregates [7, 97–99]. This is a well-known effect originating from the deformation of the surface around each particle. Indeed, a single floating particle is often surrounded by a meniscus that is a function of its shape, buoyancy, and wetting properties [97, 100, 101]. For instance, a heavy and/or hydrophobic sphere will create a concave depression on a water surface. When floating on a sloped surface, it can experience a lateral force, as it minimises its potential energy [98]. Depending on whether the particle is buoyant or not, it will tend to move up or down the slope, respectively. Two neighbouring particles will therefore attract or repel, as each particle experiences an inclination of the interface caused by the other [97]. Two heavy spheres will thus attract and cluster, as they are each dragged by gravity in the depression around the other. This phenomenon of agglomeration is colloquially known as the Cheerios effect, as it can be observed with breakfast cereals floating in a bowl of milk [7].

The capillary interaction potential can be simplified by the assumption that the deformation of the surface in the presence of two particles is the sum of the deformations caused by each particle individually. This

approximation holds for a low number of particles separated by a large distance $d \gg D$ [102]. For small particles compared to the capillary length l_c, the meniscus profile $z(d)$ around a particle is given by the Young-Laplace equation whose solution reads

$$\frac{2z}{D} = AK_0(d/l_c), \tag{3.1}$$

where A is given by the boundary conditions at the contact line and K_0 is the zero order modified Bessel function of the second kind [103]. In the approximation of small particles, the capillary interaction energy is given by the product of the resultant force of weight and buoyancy acting on one particle with the vertical displacement caused by the second particle. The potential energy between two identical spheres separated by d is therefore given by

$$U_c = -2\pi\gamma q^2 K_0(d/l_c), \tag{3.2}$$

where γ denotes the surface tension and $q = a\sin\psi$ is a typical deformation length called the capillary charge, by analogy with the Coulomb interaction potential [97]. It is a function of the contact line radius a and the meniscus slope angle ψ. Contrary to electric charges, like capillary charges attract and unlike charges repel.

3.1.2 Magnetic Interaction

It has been proposed to use magnetic floating particles to generate self-assemblies [8, 9, 44, 94–96, 104]. When a magnetisation is induced perpendicular to the interface, the particles experience a repulsive dipole-dipole interaction at short range, opposing the capillary attraction and preventing clustering [8, 9, 95]. This can lead to the appearance of a finite equilibrium distance, so that the particles self-organise into a triangular lattice, which would be the expected symmetry on a flat surface [105]. Other planar crystal symmetries have also been observed [95] as well as defects,

such as fivefold symmetries in polydisperse assemblies [95] or in heavy assemblies, when a large curvature of the surface is reached due to the combined weight of the particles [8, 9]. Similar structures have been reached with vanishing capillary interaction, using a non-uniform magnetic field for confinement instead [94, 96]. Floating magnetic particles can also form structures outside of thermodynamic equilibrium, called dynamic self-assemblies [44, 45, 104]. Such structures rely on a constant supply of energy, for instance using time-dependent magnetic fields. Examples of forces driving these dynamic assemblies include the self-induced surface waves shown in Figs 2.3 (v) and (vi) [44, 45] as well as hydrodynamic interactions induced by the rapid rotation of the particles [104].

To generate magnetocapillary assemblies, metallic spheres are placed on a water bath. The steels or alloys used (mainly UNS S42000 and G52986) and the spherical shape of the particles allow for a linear magnetisation, with little residual magnetism [102]. The magnetic moment of a particle exposed to an induction field $\vec{B}$ is expressed by $\vec{m} = \chi V \vec{B}/\mu_0$, where μ_0 is the vacuum permeability, V the volume of a sphere and χ its effective susceptibility. For a spherical object, it is linked to the bulk susceptibility χ_{bulk} by the relation $\chi = \chi_{\text{bulk}}/(1+\chi_{\text{bulk}}/3)$, such that for materials with a large susceptibility, we have $\chi \approx 3$ [103]. The materials used herein have a bulk susceptibility $\chi_{\text{bulk}} > 300$. The magnetic dipole-dipole potential between two identical spheres separated by a distance d is given by

$$U_m = \frac{\mu_0 \left[m_z^2 + m_x^2 \left(1 - 3\cos^2\theta\right)\right]}{4\pi d^3}, \tag{3.3}$$

where θ is the angle between the relative position of the pair and the horizontal magnetic field that we call here $\vec{B}_x$, but could very well point to any direction in the (x, y) plane. Vertical and horizontal components of the magnetic moments m_z and m_x have been separated, as m_z can only generate a repulsion and is usually kept constant in the course of an experiment.

Figure 3.1 illustrates the experimental setup. The magnetic induction fields are generated using three orthogonal pairs of Helmholtz coils. A direct current power supply provides the z coils with a current i_z. A multichannel arbitrary function generator going through a pairs of linear amplifiers feeds the x and y coils with currents $i_x(t)$ and $i_y(t)$. The water bath is at the centre of the coils. It is lit from below through a diffuser and filmed from above using a CCD video camera and a macro lens. A more thorough description of the experimental setup is given in Appendix A.

The materials used have a density ρ_s of approximately $7800\,\mathrm{kg\,m^{-3}}$ and thus would not float without surface tension. This places an upper bound on the diameter D of the spheres around 1 mm on water. For most experiments, we have monodisperse assemblies with 397 µm, 500 µm or 793 µm, meaning that thermal agitation is considered negligible. At room temperature, the diameter under which thermal agitation overcomes the capillary attraction for a pair of particles is 3.4 µm, as can be calculated from Eq. (3.2). This gives a lower bound on D that we will further discuss later on. Indeed, this bound could be further lowered by relying on other forces than gravity to generate the surface deformation, such as wetting [97] or a magnetic force [106], or by using another geometry for the interface [99, 107].

3.1.3 Pair Potential

One can compare the magnetic and capillary energies by defining a magnetocapillary number [102, 108]. Let $\mathscr{M}(B)$ denote the magnetocapillary number associated with a given magnetic induction field of amplitude B. We have

$$\mathscr{M}(B) = \frac{\chi^2 V^2 B^2}{8\pi^2 \mu_0 \gamma q^2 l_c^3}. \tag{3.4}$$

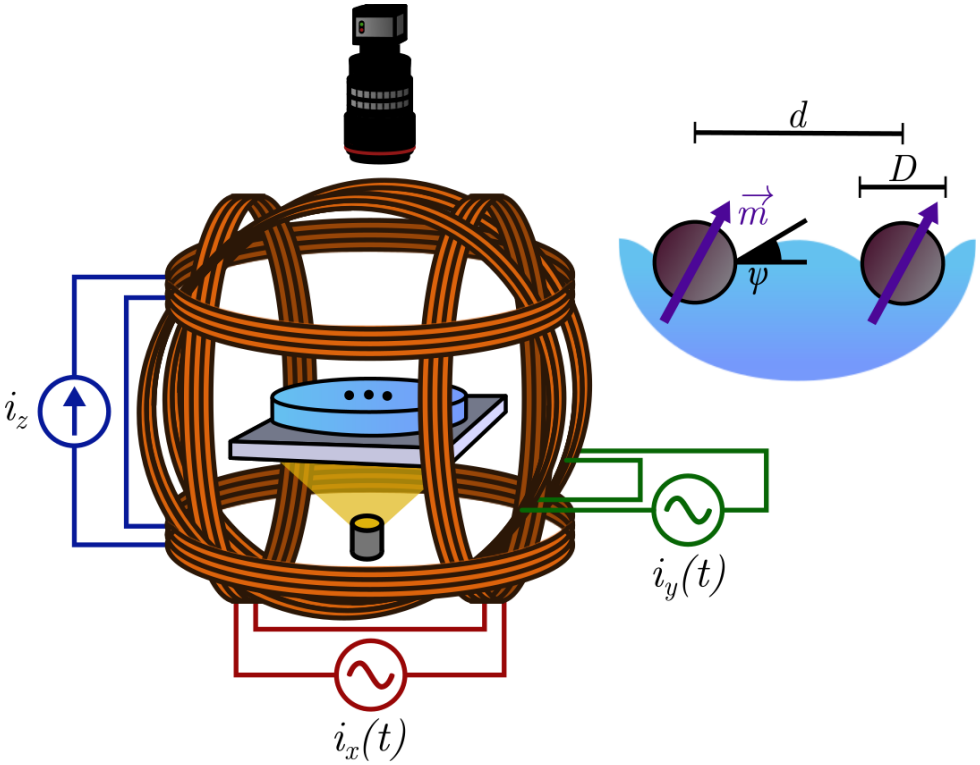

Fig. 3.1 Experimental setup of magnetocapillary self-assemblies. – A water bath is placed in the centre of a tri-axis Helmholtz coil system. A direct current i_z is injected in the z coils to generate a constant vertical magnetic induction field B_z. Currents $i_x(t)$ and $i_y(t)$ are injected in the horizontal coils to generate time-dependent horizontal magnetic fields $B_x(t)$ and $B_y(t)$. Steel spheres of diameter D floating on the bath possess a magnetic induced moment $\vec{m}$ proportional to the total magnetic field in the centre of the coils.

Using this expression, we can write the potential energy of interaction for a pair of particles as

$$\begin{aligned} U &= U_m + U_c \\ &= \Gamma \left[\frac{\mathscr{M}(B_z) + \mathscr{M}(B_x)\left(1 - 3\cos^2\theta\right)}{d^3/l_c^3} - K_0\left(d/l_c\right) \right] \end{aligned} \tag{3.5}$$

where we defined $\Gamma = 2\pi\gamma q^2$. When $B_x = 0$, the potential shows a competition between the attractive capillary force and a repulsive dipole-dipole interaction. One can differentiate Eq. (3.5) to find an expression of the forces acting on the particles. As Γ has the dimensions of an energy, Γl_c has the dimensions of a force. We can therefore define a dimensionless force

$$F(d/l_c) = \frac{3\mathscr{M}(B_z)}{d^4/l_c^4} - K_1\left(d/l_c\right) \tag{3.6}$$

where K_1 is the first order modified Bessel function of the second kind, obtained by differentiating K_0. When a horizontal component B_x is added, a preferential orientation appears, as the interaction energy is minimal for $\theta = 0$, *i.e.* when the pair is aligned with B_x. Furthermore, the contribution of B_x leads to either an attractive or a repulsive force depending on the sign of $\left(1 - 3\cos^2\theta\right)$.

3.2 Static Magnetic Induction

Depending on the number of particles N, the values of B_z and B_x, and the initial conditions, a wide variety of configurations can be observed. When $B_x = 0$ and granted that B_z is large enough to overcome the capillary attraction, a triangular lattice is typically observed. If the weight of the assembly is enough to significantly curve the interface, fivefold symmetries can also be observed [8, 9]. Figure 3.2 shows the configurations obtained for various number of particles N, with $B_x = 0$ and $B_z = 4.9\,\mathrm{mT}$. Starting

at $N = 2$, the first few structures are a line, a regular triangle, a rhombus, and an isosceles trapezoid. The 3 collinear particles that would constitute the large base of the latter are not perfectly aligned, though, and typically make an angle of 173°. For $N = 6$ and $N = 7$, the structures are a regular pentagon and a regular hexagon, respectively, with a central particle. At $N > 7$, the particles start forming an outer layer, surrounding the first few basic shapes.

The addition of a horizontal field B_x can significantly change the symmetry of the assemblies. Different configurations can coexist, and hysteresis is observed [9]. In particular, contact between particles is not always reversible, as a capillary bridge can form between two spheres, significantly increasing the energy required to separate them again.

In the case of a pair of particles, the minimum of Eq. (3.5) leads to an expression for the equilibrium distance d_{eq}. We have

$$\frac{d_{\text{eq}}^4}{l_c^4} K_1(d_{\text{eq}}/l_c) = 3\mathcal{M}(B_z) - 6\mathcal{M}(B_x) \tag{3.7}$$

as well as $\theta = 0$ if $B_x \neq 0$. A simpler expression can be obtained by considering that $K_1(d/l_c) \approx l_c/d$, which holds for $d \ll l_c$. This leads to

$$\frac{d_{\text{eq}}^3}{l_c^3} = 3\mathcal{M}(B_z) - 6\mathcal{M}(B_x). \tag{3.8}$$

Using Eq. (3.6), we can rather easily find the equilibrium distance in a three-particle assembly [108]. Let us assume that $B_x = 0$. If the particles lay on an equilateral triangle, balancing the forces exerted on each particle is equivalent to balancing each pairwise force. In other words, equilibrium is achieved when $F(d_{ij}/l_c)\,\vec{e}_{ij} = \vec{0}$ for each pair of particles (i, j), leading to the same expression for the equilibrium distance as in the two-particle

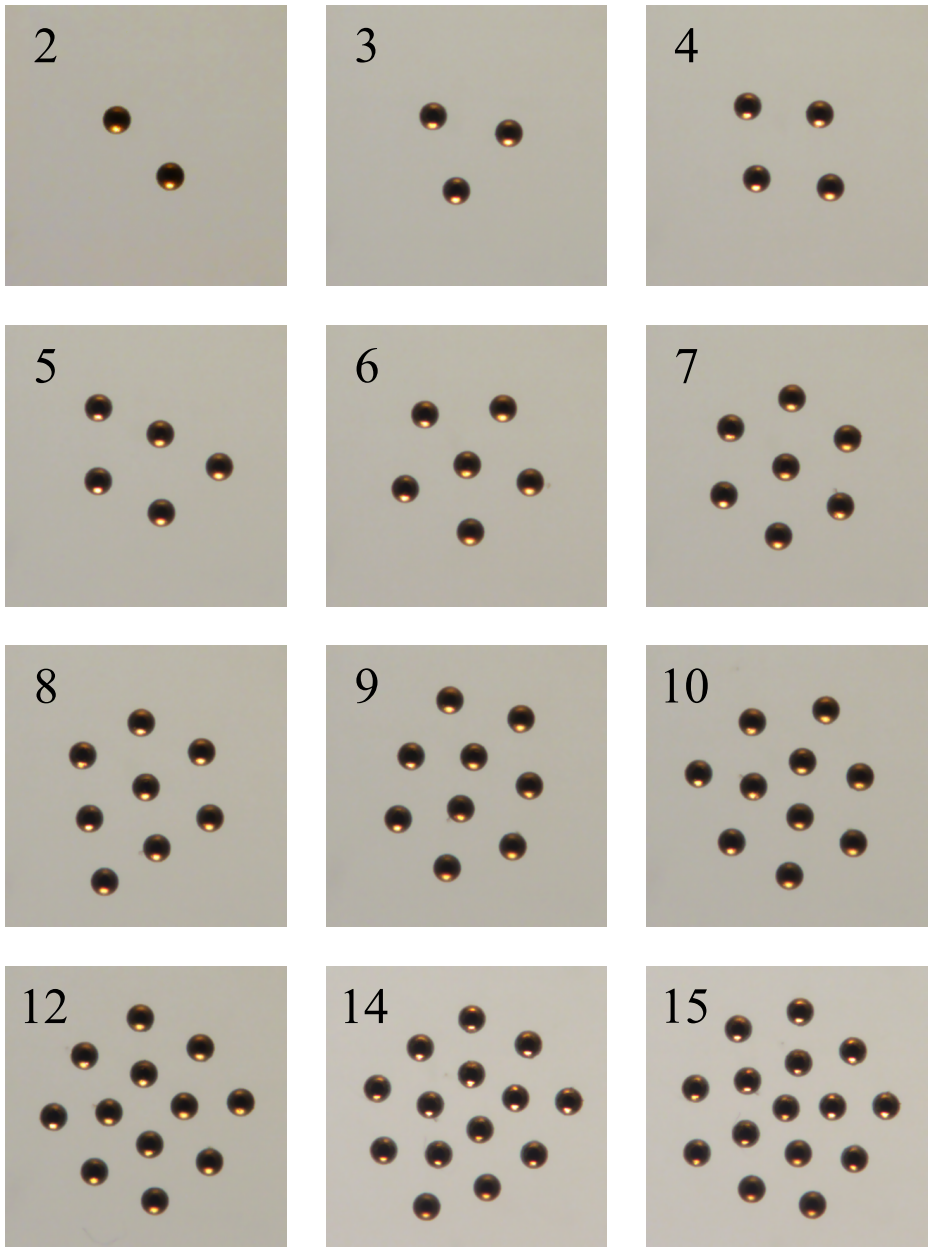

Fig. 3.2 Static assemblies. – Configurations up to 15 particles are shown, under a uniform vertical field of 4.9 mT. The first few structures build up to a 7-particle hexagon. Additional particles begin to form an outer layer, while the basic shapes are recovered in the centre.

case, *i.e.*

$$\frac{d_{\text{eq}}^3}{l_c^3} = 3\mathscr{M}(B_z). \tag{3.9}$$

However, another equilibrium exists when $F(d/l_c) + F(2d/l_c) = 0$, which corresponds to the case where the three particles form a line. Still using the approximation that $K_1(d/l_c) \approx l_c/d$, one finds a slightly lower equilibrium distance

$$\frac{d_{\text{eq}}^3}{l_c^3} = \frac{17}{8}\mathscr{M}(B_z). \tag{3.10}$$

This collinear state is not always stable, and is in fact never observed when $B_x = 0$. A linear stability analysis of the equilibrium allows to find the critical value for which the collinear state is stable to transverse perturbations [108]. Let us denote $\tilde{d}$ the value of d/l_c that satisfies $F(\tilde{d}) + F(2\tilde{d}) = 0$, in other words the dimensionless equilibrium distance in the absence of B_x. The critical value for stability is given by

$$\left(\frac{B_x}{B_z}\right)^{\text{collinear}} = \sqrt{\frac{16\tilde{d}^5}{3\mathscr{M}(B_z)} \frac{F(\tilde{d})\left(F'(\tilde{d}) + 2F'(2\tilde{d})\right)}{17F(\tilde{d}) + \tilde{d}\left(15F'(\tilde{d}) + 64F'(2\tilde{d})\right)}}. \tag{3.11}$$

Note that this calculation was done for an oscillating B_x whose effect was time-averaged, not for a static B_x [108]. For typical experimental values we have $B_x \approx 0.586\, B_z$.

The upper bound on B_x corresponds to the value for which $d_{\text{eq}} = D$, *i.e.* the particles come into contact. Going back to a pair of particles, by injecting this into Eq. (3.8), we find a critical ratio of B_x and B_z at which contact occurs, namely

$$\left(\frac{B_x}{B_z}\right)^{\text{contact, 2}} = \sqrt{\frac{\mathscr{M}(B_x)}{\mathscr{M}(B_z)}} = \sqrt{\frac{1}{2}\left(1 - \frac{D^3}{l_c^3\mathscr{M}(B_z)}\right)}. \tag{3.12}$$

For large values of $\mathscr{M}(B_z)$, this corresponds to $B_x \approx B_z/\sqrt{2}$. In general, the larger the assembly, the earlier contact occurs. This is due to two distinct effects.

First, the distance is slightly lower when the particles form a line, as shown in Eq. (3.10) for the three-particle case. Indeed, the equilibrium in this case depends on $F(2d)$, and the attractive capillary force dominates over the magnetic force at long range. One can show that in this case [108], contact occurs for

$$\left(\frac{B_x}{B_z}\right)^{\text{contact, 3}} = \sqrt{\frac{1}{2}\left(1 - \frac{24}{17}\frac{D^3}{l_c^3 \mathscr{M}(B_z)}\right)}, \tag{3.13}$$

which is slightly lower than the critical value for a pair of particles.

Secondly, the increased weight of the assembly creates a curvature of the interface, lowering the distance between neighbouring particles at the centre of the assembly [109, 110]. For small clusters, where the dipole-dipole interaction energy is limited by the number of available neighbours, we have

$$\langle d \rangle \propto N^{-1/10}. \tag{3.14}$$

For large clusters, where the dipole-dipole interaction energy is limited by the decay of the potential, the average distance between first neighbours follows the scaling

$$\langle d \rangle \propto N^{-1/4}. \tag{3.15}$$

This means that, in given conditions, there exists a maximum number of particles N_c above which contact will occur. As shown in [9], by comparing the total weight of the assembly with the capillary force on the boundary of the assembly, a scaling of N_c is found, namely

$$N_c \propto \frac{\gamma^2}{(\rho_s - \rho_l)^2 g^2 D^4} \tag{3.16}$$

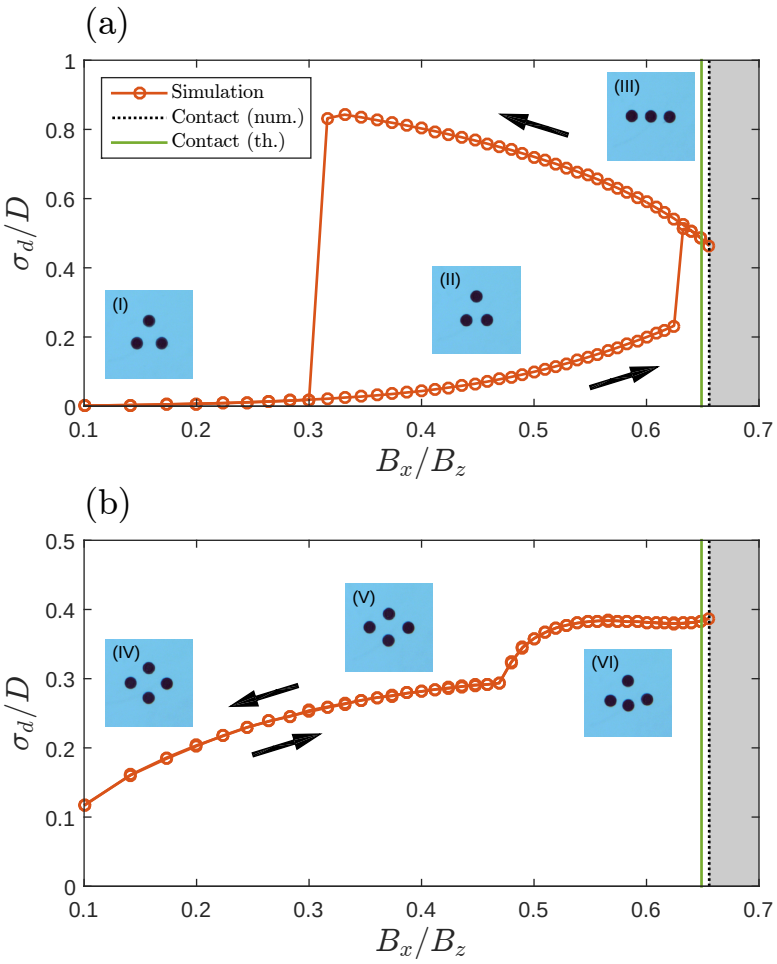

Fig. 3.3 Multiple configurations. – Standard deviation of the distances between the particles and the centre of mass during a quasistatic variation of B_x/B_z. The points are obtained by a Monte-Carlo simulation. The corresponding configurations are shown in the experiment. A green vertical line shows the contact threshold calculated from Eq. (3.13). **(a) The regular triangle** (I) formed by 3 particles deforms into an isosceles (II), then transitions into a collinear state (III). Hysteresis is observed. **(b) The rhombus** (IV) formed by 4 particles continuously deforms (V) then experiences a breaking of mirror symmetry perpendicularly to the field (VI), with no hysteresis.

where ρ_s and ρ_l denote the densities of the solid particles and the liquid, respectively. This global curvature is also at the origin of fivefold defects in the assemblies, as a triangular lattice would be expected on a flat surface.

As mentioned earlier, a horizontal field can drastically change the symmetry of an assembly. Figure 3.3 shows the structures obtained as a function of the ratio B_x/B_z, for assemblies of 3 and 4 particles. Different structures are identified by plotting the standard deviation σ_d of the distances between the particles and the centre of mass, or

$$\frac{\sigma_d}{D} = \sqrt{\frac{1}{N}\sum_{i=1}^{N}\frac{(d_i - \overline{d})^2}{D^2}} \tag{3.17}$$

where d_i denotes the distance between particle i and the centre of mass and $\overline{d}$ is the average distance to the centre of mass. The curve was obtained through a Monte-Carlo simulation based on the pair potential of Eq. (3.5). Horizontal field B_x is increased quasistatically from 0 to the point of contact, then decreased to zero, while B_z is kept constant at about 3 mT. The insets show the structures obtained in the experiment, next to the corresponding branch in the simulation. While contact between particles is generally not reversible in the experiment, the same configurations and hysteretic behaviours are observed.

In the 3-particle case, the equilibrium configuration at $B_x = 0$ is a regular triangle. When B_x/B_z is increased, the triangle gradually deforms into an isosceles. Close to the contact event, the system transitions into a collinear configuration. Contact between particles occurs around $B_x/B_z \approx 0.65$, which is very close to the value obtained from Eq. (3.13). When B_x/B_z is decreased, the system remains in the collinear configuration down to $B_x/B_z \approx 0.3$, where it goes back to the isosceles configuration. This hysteresis loop demonstrates the coexistence of two stable configurations.

On the other hand, no hysteresis is observed in the 4-particle case. At $B_x/B_z = 0$, we have $\sigma_d/D \neq 0$. Indeed, the particles are not equidistant

to the centre of mass, as the assembly takes the shape of a rhombus with two particles closer to the centre, and the other two further away. When B_x/B_z is increased, this difference becomes larger. Around $B_x/B_z \approx 0.5$, the symmetry is further broken in the system when the two outermost particles align with one of the innermost ones. This transition happens continuously. Contact occurs when the three aligned particles touch, which also happens at $B_x/B_z \approx 0.65$.

Note that representing the deformation of the assemblies with a single variable, σ_d, does not allow to distinguish configurations that are too similar. For instance, two isosceles configurations can exist in the 3-particle case, depending on the initial conditions. However, they both produce similar values of σ_d. To distinguish these isosceles requires a more detailed study of the internal angles of the triangular states [28]. Nonetheless, this brief quasistatic analysis of the assemblies demonstrates the presence of several states with hysteresis loops, and continuous as well as discontinuous transitions. More importantly, the effect of N on the configurations is profound, meaning that what is known for assemblies of N particles cannot, in general, be transcribed to assemblies of $N' \neq N$ particles. Each N possesses its own energy landscape, so that the addition or removal of a particle has non-trivial consequences.

3.3 Summary

Self-assembly is a desirable way to reversibly assemble components into predetermined configurations. To achieve this, we rely first on an attractive force called the Cheerios effect, a lateral capillary force between floating particles that locally deform the interface. We prevent contact through a short-range magnetic dipole-dipole interaction, which can be tuned thanks to the soft-ferromagnetic properties of the chosen particles. A vertical field generates an isotropic interaction, causing the particles to assemble into

fivefold or sixfold symmetries. The strength of the field determines the size of the assembly. The addition of a horizontal component can deform the assembly, break symmetries and allow some new configurations to appear. The richness of the energy landscape will allow to design low-Reynolds-number swimmers that deform in a non-time-reversible way. A key parameter is the number of particles, which drastically changes the number and type of possible states and transitions. In each chapter of this thesis, we will therefore consider various configurations of particles and magnetic fields, starting with the simplest magnetocapillary self-assembly: a pair of particles.

4 Two-Particle Dynamics

In this chapter, we discuss the dynamics of the fundamental building block of magnetocapillary assemblies: a dimer composed of two particles. When submitted to oscillating fields, the pair vibrates. Two eigenmodes are identified, a stretching mode and a swinging mode. The associated resonance curves are measured and compared with theory.

Partially published as

- G. Lagubeau, G. Grosjean, A. Darras, G. Lumay, M. Hubert, N. Vandewalle, Phys. Rev. E **93**, 053117 (2016)

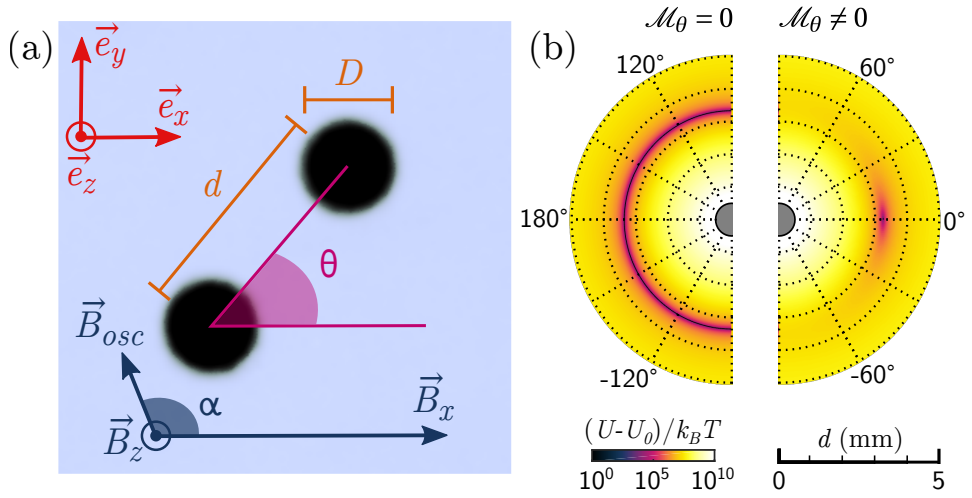

Fig. 4.1 Pair potential. – **(a) Notations.** Two beads are placed at a water surface and submitted to a constant induction $\vec{B} = B_x\vec{e}_x + B_z\vec{e}_z$ as well as a small oscillating induction $\vec{B}_{\text{osc}}$. Distance d and angle θ characterise the system. **(b) Magneto-capillary potential.** Interaction potential $U = U_c + U_m$ in polar coordinates (d,θ), as given by Eq. (4.3), for typical parameters of the experiment ($D = 500\,\mu$m, $B_z = 3$ mT). Darker zones indicate potential wells. $\mathcal{M}_\theta$ is the orthoradial magnetocapillary number introduced in Eq. (4.3), proportional to B_x^2. On the left half, vertical induction $\vec{B}_z$ generates an isotropic repulsion when $\mathcal{M}_\theta = 0$, which leads to a finite equilibrium distance $d_{\text{eq}} \approx 2.5$ mm. On the right half, cylindrical symmetry is broken when $\mathcal{M}_\theta \neq 0$, due to the addition of a horizontal field $B_x = 0.7$ mT.

4.1 Vibration Modes

We consider two floating beads of diameter D possessing identical magnetic moments $\vec{m} = m_x\vec{e}_x + m_z\vec{e}_z$, $\vec{e}_x$ and $\vec{e}_z$ being the horizontal and vertical unitary vectors, respectively, as defined in Fig. 4.1 (a). Their centre-to-centre vector is denoted $\vec{d} = d\vec{e}_r$, and the orientation of the pair relatively to $\vec{e}_x$ is θ. Their interaction can be modelled by a pair potential U, as defined in Eq. (3.5), composed of the sum of an attractive term due to capillarity

U_c and a magnetic dipole-dipole term U_m that is usually chosen to be repulsive.

For conciseness, we will define the following magnetocapillary numbers

$$\mathcal{M}_\theta = \mathcal{M}(3B_x) = 3\mu_0 m_x^2/4\pi\Gamma l_c^3 \tag{4.1}$$

$$\mathcal{M}_d = \mathcal{M}(\sqrt{B_z^2 - 2B_x^2}) = \mu_0(m_z^2 - 2m_x^2)/4\pi\Gamma l_c^3 \tag{4.2}$$

Let us define also define a nondimensional distance $\tilde{d} = d/l_c$. We can rewrite Eq. (3.5) as

$$U = \Gamma\left[-K_0(\tilde{d}) + \frac{\mathcal{M}_d}{\tilde{d}^3} + \frac{\mathcal{M}_\theta}{\tilde{d}^3}\sin^2\theta\right]. \tag{4.3}$$

We call $\mathcal{M}_d$ the radial magnetocapillary number and $\mathcal{M}_\theta$ the orthoradial magnetocapillary number.

While the magnetic terms of U are dominating at both short and long distances, it has a stable minimum provided that $\mathcal{M}_d < 1.11$. Thus, it forms a potential well around $\theta = 0$ and the equilibrium distance d_{eq}. With the definitions introduced in Eqs. (4.1) and (4.2), we can rewrite Eq. (3.7) as depending only on $\mathcal{M}_d$, such that

$$\tilde{d}_{\text{eq}}^4 K_1(\tilde{d}_{\text{eq}}) = 3\mathcal{M}_d. \tag{4.4}$$

If $\mathcal{M}_\theta = 0$, the potential is axisymmetric and every orientation θ is equivalent for the pair. Figure 4.1 (b) shows the interaction potential U in polar coordinates, with one bead at the axis origin, for typical values of the experiment. Because the potential is mirror symmetric around the 90° axis, the two halves of the graph are chosen to represent two cases. Case $\mathcal{M}_\theta = 0$ is on the left, with a minimum of energy at a given distance d_{eq}. On the right, the addition of a horizontal induction B_x of order 10^{-3} T ($\mathcal{M}_\theta \neq 0$) breaks axisymmetry and creates an equilibrium orientation at $\theta = 0$. Typical val-

ues for the experiment are $B_z \approx 5\,\mathrm{mT}$ and $B_x \approx 2\,\mathrm{mT}$, which gives a ratio $\mathscr{M}_\theta/\mathscr{M}_d \approx 0.8$.

Using a perturbative analysis of U, the stiffness of the potential well can be obtained for its two principal directions (radial k_d and orthoradial k_θ):

$$k_d = \frac{\Gamma}{l_c^2 \tilde{d}}\left[6K_1(\tilde{d}) - 2\tilde{d}K_0(\tilde{d})\right] \tag{4.5}$$

$$k_\theta = 4\frac{\Gamma \mathscr{M}_\theta^2}{l_c^2 \tilde{d}^5}. \tag{4.6}$$

In the case of two identical beads of mass $M_1 = M_2 = M$, the reduced mass is $M/2$. Added mass for a fully immersed sphere oscillating with small amplitudes is $M_{\text{added}} = 0.5\, M\rho_f/\rho_s$. For steel spheres on water, we have $\rho_s/\rho_f \approx 8$, so that $M_{\text{added}} \approx M/16$. We will therefore consider that the mass of entrained fluid is negligible.

Two frequencies can thus be associated with the magnetocapillary well: (i) a radial frequency

$$\omega_d = 2\pi f_d = \sqrt{2k_d/M} \approx \frac{2}{l_c}\sqrt{\frac{U_c(\tilde{d}_{\text{eq}})}{M} + \frac{9\mathscr{M}_d\Gamma}{M\tilde{d}_{\text{eq}}^5}}, \tag{4.7}$$

where we assumed $d \gg D$, that corresponds to a stretching mode and (ii) an orthoradial frequency

$$\omega_\theta = 2\pi f_\theta = \sqrt{2k_\theta/M} = \frac{2\mathscr{M}_\theta}{l_c}\sqrt{\frac{2\Gamma}{M\tilde{d}_{\text{eq}}^5}} \tag{4.8}$$

that corresponds to a swinging mode. At low Reynolds, the attenuation is due to the viscosity of the ambient fluid, so that attenuation time is

$$\tau = \frac{M}{C} \sim \frac{M}{\eta D} \tag{4.9}$$

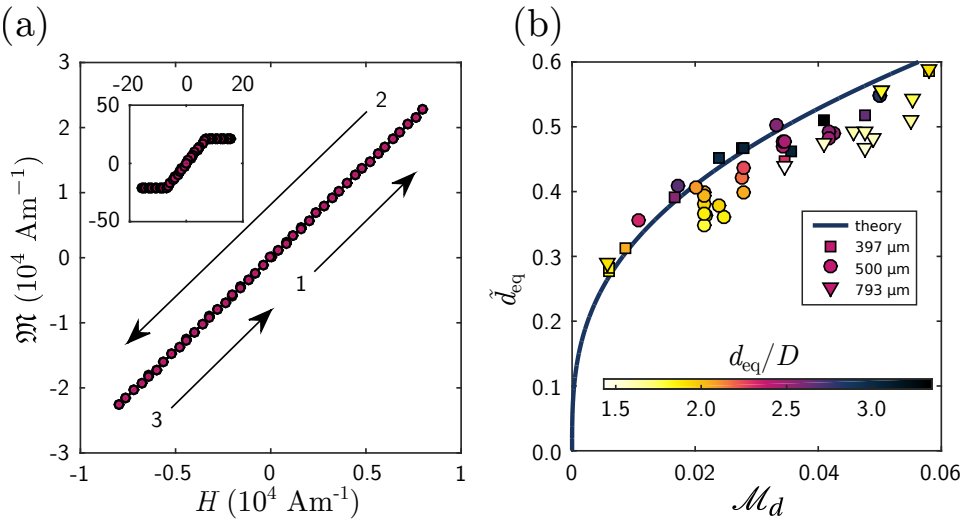

Fig. 4.2 Characterisation of the system. – (a) Beads magnetisation. Magnetic field H induces a magnetisation $\mathfrak{M}$ in a 500 µm bead with negligible hysteretic behaviour. H is successively increased from 0 (1), decreased (2) and increased back to 0 (3). Values of H are typical of the experiment. Inset shows a larger cycle up to saturation magnetisation, with same units. **(b) Equilibrium distance.** The dimensionless equilibrium distance $\tilde{d}_{eq}$ as a function of the radial magnetocapillary number $\mathcal{M}_d$. The colourmap shows distance d_{eq} over diameter D. Solid line corresponds to theoretical prediction without adjustable parameter, obtained by numerically solving Eq. (4.4). Symbols represent different bead diameters.

where C is the damping coefficient. We have $C_{\text{Stokes}} = 3\pi\eta D$ in the case of a fully immersed sphere [111, 112]. If $f_d\tau \geq 1$ or $f_\theta\tau \geq 1$, we can force harmonic resonances, even in the Stokes regime. This is of interest as frequency can thus be changed to adjust phase.

4.2 Experimental Results

Two identical submillimetric chrome steel beads are disposed at the water-air interface. The capillary charges of the beads, as introduced in Eq. (3.2), are calculated for a contact angle of 90°. We find 6 µm, 12 µm and 45 µm

for the respective particle diameters 397 µm, 500 µm and 793 µm. In the presence of a constant magnetic induction $\vec{B} = B_x\vec{e}_x + B_z\vec{e}_z$, the beads settle at an equilibrium distance d_{eq}. For vibration experiments, a small oscillating induction $\vec{B}_{\text{osc}} = B_{\text{osc}}(t)(\cos\alpha\,\vec{e}_x + \sin\alpha\,\vec{e}_y)$ is added. Angle α can be varied to produce different oscillating behaviours. The kinematics of the system is fully described by the beads centre-to-centre distance d and its rotation angle θ as defined in Fig. 4.1 (a).

The bulk material (UNS G52986) is ferromagnetic and has a large susceptibility χ, which depends on applied magnetic field $H = B/\mu_0$, such that $\chi(H) > 300$ [113]. However, a finite ferromagnetic body in a magnetic field produces a demagnetisation effect. An effective susceptibility χ_{eff} takes this effect into account, which for a sphere has the form $\chi_{\text{eff}} = \chi/\left(1+\chi/3\right)$ [103, 114]. For $\chi \gg 3$, the sphere will thus behave like a superparamagnetic particle of susceptibility $\chi_{\text{eff}} = 3$. In Fig. 4.2 (a), we plot the experimental magnetisation curve $\mathfrak{M}(H)$. Indeed, no hysteresis is observed, and the slope gives $\chi_{\text{eff}} \simeq 3$ as expected. A small magnetisation remains at zero field, of the order of $100\,\text{A}\,\text{m}^{-1}$, which is negligible for the fields used herein (typically $5000\,\text{A}\,\text{m}^{-1}$). Note that the dipole moment is simply the product of the magnetisation with the volume of the particle, or $m = \mathfrak{M}V$.

Equilibrium distance d_{eq} has been measured for 3 diameters D and various values of radial magnetocapillary number $\mathscr{M}_d$, changed by varying both B_x and B_z. As seen in Fig. 4.2 (b), the equilibrium distance calculated from the interaction potential, as defined in Eq. (4.4), is in good agreement with experimental values for large distance d_{eq} compared to diameter D. Indeed, for $d_{\text{eq}}/D \lesssim 2$ (light-coloured points in the graph), the superposition approximation no longer holds in the determination of capillary potential U_c [115]. In this case, the attraction is stronger. These low d_{eq}/D points are also more broadly distributed for a given $\mathscr{M}_d$, which might be due to a stronger influence, at short range, of anomalies in the contact line.

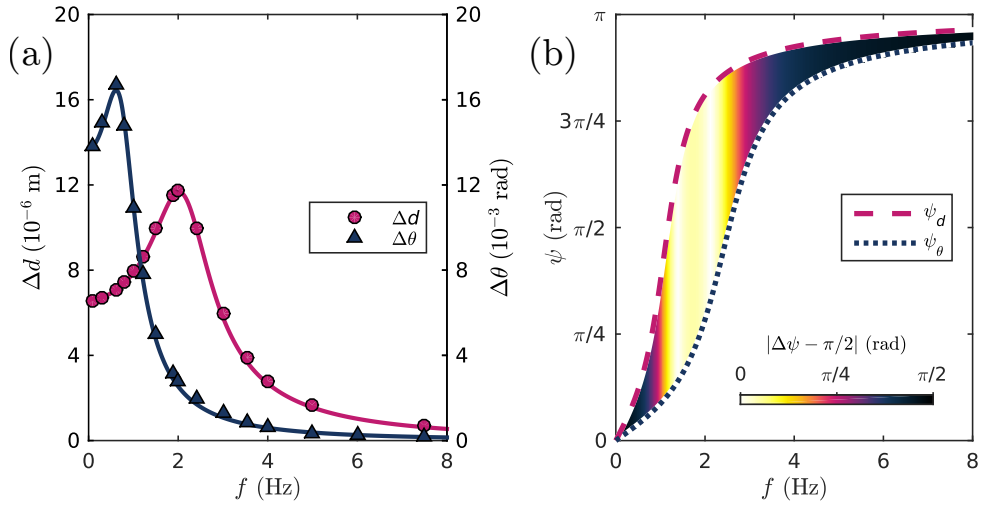

Fig. 4.3 Resonance spectrum. – (a) Amplitude. Frequency response of distance d and angle θ for typical values of the experimental parameters ($D = 500\,\mu$m, $\mathcal{M}_\theta/\mathcal{M}_d \approx 0.8$). Radial oscillation of amplitude Δd happens for $\alpha = 0°$, while orthoradial oscillation of amplitude $\Delta\theta$ happens for $\alpha = 90°$. Error bars are smaller than the symbols, with a typical error of $0.2\,\mu$m on the bead centre. Data have been fitted with a resonance curve (see Eq. (4.10)), represented by solid lines. **(b) Phase.** Theoretical prediction for the phase in both cases, given by Eq. (4.11). The colourmap indicates phase difference $\Delta\psi$.

In order to characterise the properties of the magnetocapillary well, a horizontal oscillating induction $\vec{B}_{\rm osc}(t)$ is added, with magnitude $B_{\rm osc}(t) = B_{\rm osc}\sin(2\pi f t)$ and making an angle α with $\vec{B}_x$. A small oscillation amplitude $B_{\rm osc} \ll |\vec{B}_x|$ is chosen, so that the system remains close to its equilibrium configuration. Perturbative analysis gives two oscillation modes in radial and orthoradial directions, that we will excite independently. Two values of angle α corresponding to both directions will thus be studied: $\alpha = 0°$ (radial) and $\alpha = 90°$ (orthoradial).

In Fig. 4.3 (a), oscillation amplitudes of distance d and angle θ are represented as a function of frequency. Each point was obtained by identifying the geometric centre of each bead, averaged over 10 oscillation periods,

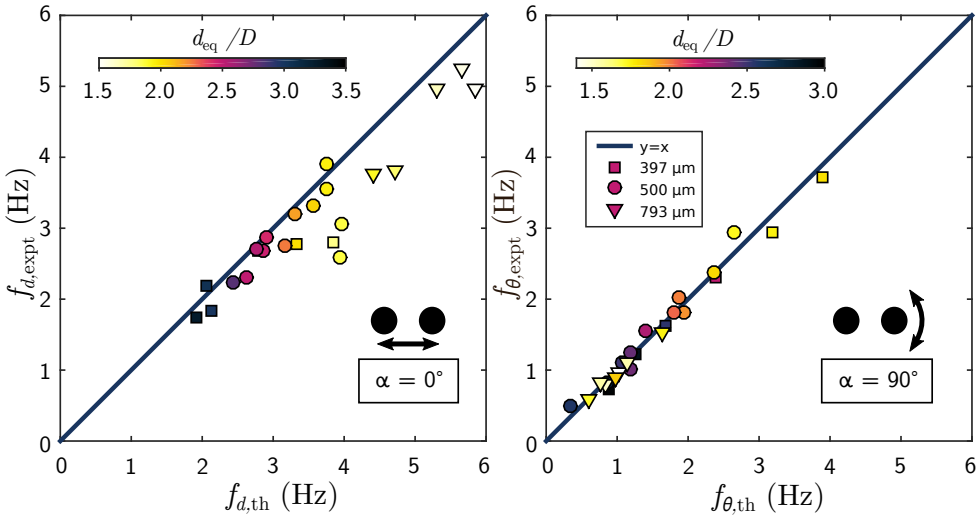

Fig. 4.4 Resonance frequencies. – Comparison between measured resonance frequency f_{exp} and theoretical prediction f_{th}, for several values of induction fields B_x, B_z and B_{osc} as well as several bead diameters. Two orientations α of $\vec{B}_{osc}$ are explored which correspond to radial and angular oscillations, respectively $\alpha = 0°$ on the left and $\alpha = 90°$ on the right. Theory and experiment agree well, with the exception of distances $d_{eq}/D \lesssim 2$ in case $\alpha = 0°$, corresponding to light-coloured points in the left graph.

in order to reach sub-pixel precision. Two independent oscillation modes can indeed be excited: a radial mode of amplitude Δd for $\alpha = 0°$, for which d oscillates around d_{eq} and $\theta = 0$ (stretching mode), and an orthoradial mode of amplitude $\Delta\theta$ for $\alpha = 90°$, called swinging mode, for which θ oscillates around 0 and $d = d_{eq}$. Both modes exhibit a resonance, with distinct resonance frequencies $f_d > f_\theta$ in this example.

The steady-state solution of a forced damped harmonic oscillator is usually defined as the real part of a complex number $z(t) = R(\omega)e^{i\omega t}$ with function $R(\omega) = A(\omega)e^{-i\psi(\omega)}$. If F_0/M is the driving force per unit mass, we have the following expressions for amplitude $A(\omega)$ and phase $\psi(\omega)$,

respectively

$$A(\omega) = \frac{F_0/M}{\sqrt{(\omega_0^2 - \omega^2)^2 + 4\omega^2/\tau^2}} \tag{4.10}$$

and

$$\psi(\omega) = \arctan\left(\frac{2\omega}{\tau(\omega_0^2 - \omega^2)}\right), \tag{4.11}$$

with angular frequency $\omega = 2\pi f$, resonance frequency $\omega_0 = 2\pi f_0$ and damping time τ. Data in Fig. 4.3 (a) are very well fitted by function $A(\omega)$, with fit parameters F_0/M, ω_0 and τ. The resonance curves correspond to underdamped harmonic oscillators as the quality factor $Q = \omega_0\tau/2$ ranged between 0.6 and 3.8. The resonance frequencies in all of the experiments ranged between 0.5 Hz and 5.2 Hz. Finally, the time scale τ given by the fit corresponds to an average viscous damping coefficient C that grows linearly with bead diameter D and is close to a Stokes damping $C_{\text{Stokes}} = 3\pi\eta D$, such that

$$\frac{C}{C_{\text{Stokes}}} = 0.86 \pm 0.04. \tag{4.12}$$

This seems consistent with the viscous damping of a partially immersed sphere [111, 112]. The dispersion of the values can be due to the interaction between the spheres, as well as slight variations of the wetting conditions. Note that this average value of C excludes radial oscillations for which $d_{\text{eq}}/D \lesssim 2$, which are discussed below. Figure 4.3 (b) represents the corresponding phases ψ. Because radial and orthoradial resonance frequencies are distinct, a phase difference $\Delta\psi$ can arise between modes. Close to resonance frequencies, we have $\Delta\psi \approx \pi/2$.

Radial and orthoradial resonance frequencies, respectively f_d and f_θ, are determined for different sets of parameters B_x, B_z, B_{osc} and D. Figure 4.4 compares experimental values $f_{d,\,\text{exp}}$ and $f_{\theta,\,\text{exp}}$ with theoretical predictions $f_{d,\,\text{th}}$ and $f_{\theta,\,\text{th}}$ as defined in Eqs. (4.7) and (4.8). Case $\alpha = 0°$ shows good agreement for large values of d_{eq}/D, but theory gives overall an overestimation of frequency f_d for distances $d_{\text{eq}}/D \lesssim 2$. This evidences

the limits of validation of the superposition approximation in capillary potential U_c. Furthermore, the points corresponding to $d_{\mathrm{eq}}/D \lesssim 2$ are more broadly distributed for a given value of $f_{d,\,\mathrm{th}}$. This might be due to irregularities in the contact line, caused by hysteresis or imperfections on the spheres. This effect would only be visible at short range, where reproducibility is reduced. In case $\alpha = 90°$, by contrast, theory and experiment agree well. Indeed, linear regression gives $f_{d,\,\mathrm{exp}} \approx f_{d,\,\mathrm{th}}$ down to about 1%. Because distance d is constant in the orthoradial case, capillarity does not act as a spring force, which explains why this limit of validation is not observed.

4.3 Interpretation

4.3.1 Quality Factor

Controlling the phase difference between degrees of freedom is the key ingredient for generating significant non-reciprocal deformations, which are necessary for low Reynolds propulsion [13]. Indeed, to propel itself, a body immersed in a fluid must produce a net flow over a time period. This means that low Reynolds swimmers must find a way around the time-reversal properties of Stokes flows, either by using the medium to break symmetry [27] or by undergoing non-reciprocal, *i.e.* non-time-reversible, deformations [10, 13]. Note that the field itself can be time-reversible, as the system spontaneously breaks time-reversal symmetry through magnetocapillary interactions [28].

In this chapter, we evidenced that for magnetocapillary bonds, even if the fluid is in a Stokes regime, the Reynolds number is not the only parameter driving the dynamics of this system, the inertia of the oscillators has to be taken into account. Indeed, the quality factor

$$Q = \omega_0 \tau / 2 \tag{4.13}$$

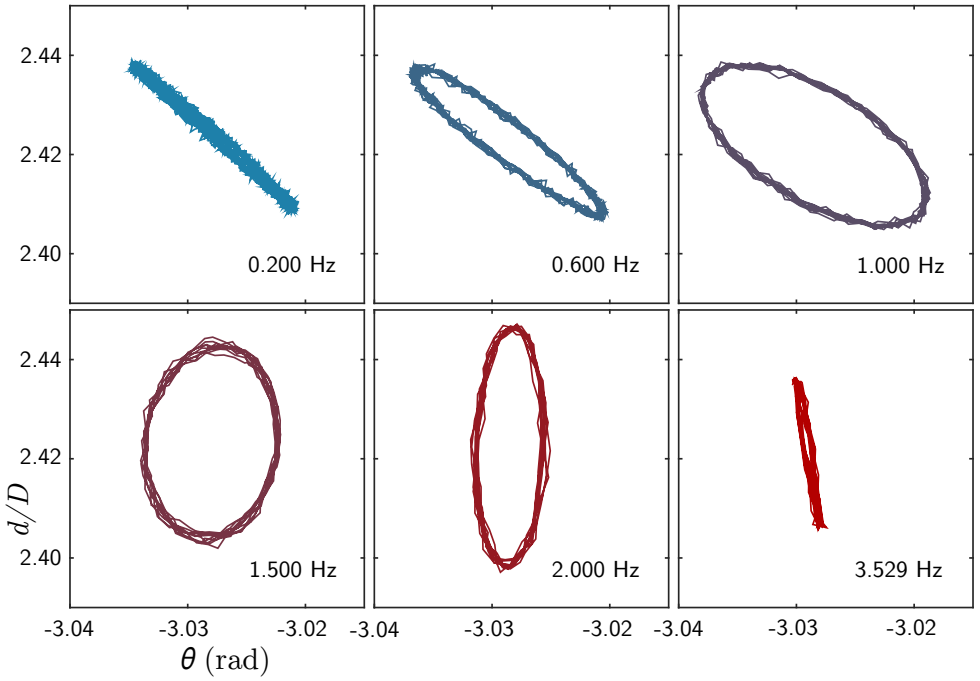

Fig. 4.5 Deformation cycles. – Trajectories in plane $(\theta, d/D)$ for 10 periods of the oscillating induction with $\alpha = 45°$. Below both resonance frequencies, in-phase oscillations produce no loop. When the frequency is increased, loops appear as oscillations get out of phase. Above both resonances, cycles disappear as phase difference decreases to zero.

can be over unity, meaning that the system is underdamped, granted that the stiffness of the potential and the particle mass are high enough. This is of interest for creating phase differences between stretching and swinging of the bonds. Each mode possesses a quality factor Q which gives the shape of the resonance curve, and the ratio of the frequency to the resonance frequency $\xi = \omega/\omega_0$ allows to distinguish between the well known regimes of a forced harmonic oscillator. Firstly, assuming $Q > 1$ (for $Q < 1$, the same discussion can be made using $1/Q$ instead of Q), if $\xi < 1/Q$ the oscillator follows the forcing in a quasistatic way, in phase. Then, if $Q > \xi > 1/Q$, the dynamics is limited by the viscous dissipation and the oscillation of the

system is in quadrature with the forcing. Finally, if $\xi > Q$ the oscillator is limited by inertia and oscillates in phase opposition with the forcing.

The stretching and swinging modes of the magnetocapillary bond are generally detuned ($f_d \neq f_\theta$). They can be both excited simultaneously using intermediate angles α (0° and 90° produce pure radial and orthoradial oscillations respectively). If the resonances are sufficiently separated i.e, $f_d/f_\theta < 1/Q$ or $f_d/f_\theta > Q$, the excitation frequency can be chosen so that one mode oscillates in quadrature and the other oscillates in phase or phase opposition with the excitation as was shown in Fig. 4.3. Therefore, the system can follow simple non-reciprocal Lissajous curves (ellipses) in the plane $(\theta, d/D)$ whose shape depends on control parameters f and α. Figure 4.5 represents six cycles for $\alpha = 45°$. For each cycle, 10 periods of the oscillating induction are represented. For frequencies below both resonances, *i.e.* $f < f_d$ and $f < f_\theta$, in-phase oscillations produce reciprocal deformations. When frequency is increased, cycles appear as oscillations get out of phase. Around resonance frequencies, phase difference is close to $\pi/2$. At frequencies higher than both resonances, *i.e.* $f > f_d$ and $f > f_\theta$, cycles disappear as phase difference decreases to zero.

4.3.2 Downscaling

Further decreasing the size of the system could prove useful for future applications, including low Reynolds swimming. To determine if a phase difference is achievable at smaller scale, we can look at the expressions of quality factors in radial and orthoradial directions. For a constant ratio D/d, we have

$$Q_\theta = \frac{\omega_\theta \tau}{2} \sim DB. \tag{4.14}$$

This means that orthoradial q factor can be kept constant, granted that induction field B is increased accordingly. As a matter of fact, at the centre of a Helmholtz system, we have $B \sim 1/R$ where R is the radius of the coils.

If coil size is decreased along with particle diameter D, with everything else kept constant, the orthoradial oscillator will behave similarly. In radial direction, however, we have

$$Q_d = \frac{\omega_d \tau}{2} \sim \frac{qD^2}{d} \sim \frac{D^5}{d} \tag{4.15}$$

since capillary charge $q \sim D^3$. With a constant ratio D/d, we have $Q_d \sim D^4$ meaning that radial oscillation is overdamped at smaller scales. As a result, for small scale systems, the only way to achieve non-reciprocal cycles is to use the orthoradial resonance frequency as excitation frequency. Of course, a capillary charge that is not powered by the weight of the particle, but by wetting [99] of geometrical effects [101], would change the scaling of Q_d and possibly allow a radial resonance at much smaller scales.

Magnetocapillary bonds in assemblies of more than 2 particles are usually not aligned, meaning that both modes are always excited. This may explain why a single oscillating sinusoidal field can generate efficient locomotion [10, 28]. Previous theoretical work on magnetocapillary systems [108] studied the Stokesian motion of particles in a magnetocapillary well, finding insufficient symmetry breaking to account for efficient low Reynolds locomotion in a three beads system. Lastly, it is obvious from Eq. (4.3) that for larger deformations, the potential becomes anharmonic. Stretching and swinging degrees of freedom become coupled, opening a rich variety of nonlinear behaviours.

4.4 Summary

A magnetocapillary dimer possesses two eigenmodes, as evidenced by an experimental perturbative analysis where the particles are submitted to low-amplitude magnetic oscillations. The modes correspond to a radial and an angular vibrations, each possessing their own stiffness and

resonance frequency. The existence of a resonance is possible because the oscillators are underdamped, even though the Reynolds number is low. Non-reciprocal deformations are observed due to the phase difference between the oscillations, however their central symmetry does not allow to distinguish a swimming direction. No net motion is, in fact, ever observed in an oscillating particle pair. Non-reciprocal deformations are indeed a necessary, but not sufficient condition for locomotion. To swim, a minimum of 3 particles is therefore required.

5 A Simple Swimmer

In this chapter, we present a one dimensional swimmer based on the kinematic model of a "simple swimmer at low Reynolds number" proposed by Najafi and Golestanian [23]. Three particles are placed on a line and submitted to oscillating fields. With particles of different sizes, this assembly behaves as two magnetocapillary dimers with each their own resonance frequency. This can create a phase shift between the oscillations, leading to locomotion at low Reynolds number.

Partially published as

- G. Grosjean, M. Hubert, G. Lagubeau, N. Vandewalle, Phys. Rev. E **94**, 021101 (2016)

5.1 Bottom-up Approach

Nature provides plenty of examples of efficient microswimmers. For instance, microbes use their flagella, cilia [13] or the deformations of their membrane [29] to propel themselves. Several strategies of propulsion have been studied experimentally, such as externally actuated flagella [24], rotating helical tails [117] or propulsion by chemical gradients [47]. However, a bottom-up approach, looking at the simplest ingredients needed to generate a microswimmer, can lead to a deeper understanding of the swimming problem. This approach could also end up providing us with designs more suited to technological or medical applications.

Simple kinematic models based on the idea of non-reciprocal deformations have been extensively studied. The most well-known are Purcell's three-link model [4], where three arms are linked by two hinges around which they can rotate (see Fig. 2.1 (iv)), and Najafi and Golestanian's three-linked-spheres model [23], where three in-line spheres are linked by two arms of varying lengths (see Fig. 2.1 (v)). The former resembles a discrete, simplified flagellum [118]. The latter moves by shifting mass forwards, mimicking ameboids [29] and recoil swimmers [119]. It has the added advantage of involving translational degrees of freedom in one dimension, which allows analytical studies [30].

While these kinematic models offer a convenient basis for theoretical studies, small-scale experimental implementations are scarce. Indeed, such models impose the shape of the swimmer at all times, as if controlled by micromotors and actuators, which leads to serious technological limitations. In the case of the three-linked-spheres model, Leoni *et al.* reproduced the deformation sequence using optical tweezers [120]. However, this has the consequence of pinning the swimmer in a potential well, meaning that a continued translational motion is impossible [120].

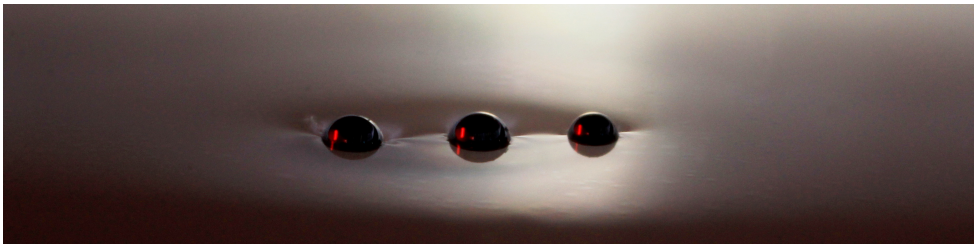

Fig. 5.1 Photograph of the collinear swimmer. – It is composed of two steel spheres of diameter 500 µm and one of 397 µm, partially immersed in water. The meniscus around the spheres allows flotation and generates an attraction.

This chapter examines an experimental realisation of the three-linked-spheres swimmer by self-assembly, using submillimetric spheres actuated by an external force. Instead of rigid, extensible arms, this model is based on harmonic oscillators [102]. The breaking of time-reversibility comes from a spontaneous phase shift between the oscillators.

5.2 Experiment

5.2.1 Principle

Three ferromagnetic steel spheres are placed at an air-water interface and exposed to magnetic induction fields, as seen on Fig. 5.1. In the presence of a vertical induction field B_z, large enough to counter the capillary attraction, the particles self-assemble [10, 102, 108]. This process is characterised by the magnetocapillary number $\mathcal{M}_z = \mathcal{M}(B_z)$, as introduced in Eq. (3.4). As shown in the Monte-Carlo simulations from Fig. 3.3 (a), the self-assembly can reach two possible configurations : an equilateral one and a collinear one. The latter is only stable with the addition of a horizontal field B_x larger than a critical value, as given in Eq. (3.11). A sketch of this configuration is shown in Fig. 5.2 (a). For a typical experimental value of $\mathcal{M}_z \approx 0.1$, the collinear state is stable for a relatively narrow range of parameters. Indeed,

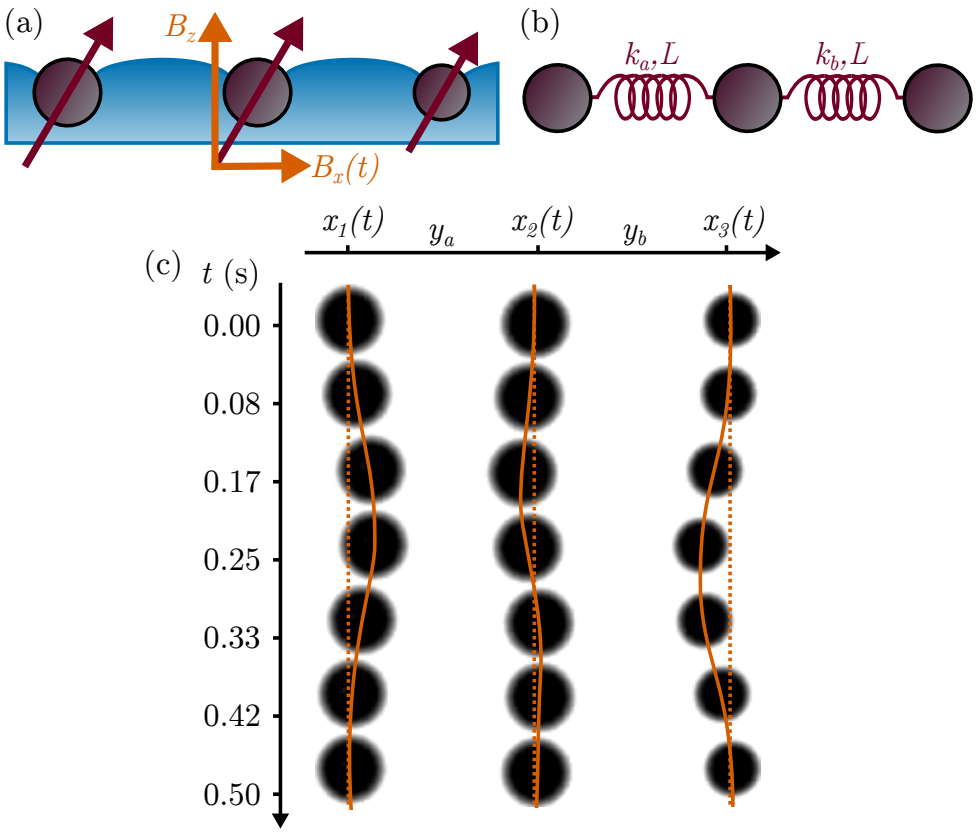

Fig. 5.2 Principle of the collinear swimmer. – (a) Configuration in the experiment. Three beads experience a combination of magnetic dipole-dipole interactions and an attraction due to surface deformation. **(b) Theoretical model.** Three aligned particles linked by two springs of rest length L and spring constants k_a and k_b. **(c) Deformation sequence.** A spatio-temporal montage shows a non-reciprocal deformation sequence in the experiment.

the critical B_x for stability as calculated in Eq. (3.11) is close to the value for which contact occurs between the particles, calculated in Eq. (3.13).

In the collinear state, particles are arranged similarly to the model shown in Fig. 5.2 (b). Indeed, the magnetocapillary interaction between two particles acts as a spring force for small displacements [102]. Let us consider two oscillators with two different natural frequencies f_a and f_b. The interaction between the two outermost spheres is neglected. This configuration allows to break time-reversal symmetry using a single excitation force, without needing independent forcings [30, 32, 33] or self-propelled components [121]. For this, particles of different diameters must be used. Two spheres of diameter $D_1 = D_2 = 500\,\mu\text{m}$ and one of $D_3 = 397\,\mu\text{m}$ are used throughout this chapter, but different combinations of sizes have been tried with similar results. We therefore have two magnetocapillary bonds: bond "500-500" of elongation y_a and spring constant k_a; and bond "500-397" of elongation y_b and spring constant k_b. The corresponding natural frequencies are $f_a = 1.810\,\text{Hz}$ and $f_b = 2.093\,\text{Hz}$. Rest lengths of the bonds are approximately equal, denoted L [9]. In the experiments, we typically have $L \approx 2D$. If each particle has a mass m and a viscous damping coefficient μ, we find $\mu/m = 14.6\,\text{s}^{-1}$ for 397 µm beads and $\mu/m = 9.2\,\text{s}^{-1}$ for 500 µm beads. The quality factor $Q = \pi f m/\mu$ associated with each oscillator is $Q_a = 1.09$ and $Q_b = 1.89$. Note that the quality factor must be non-zero for at least one of the oscillators, so that a phase difference that is not a multiple of π can appear around the resonance frequency.

When a time dependent horizontal field $B_x(t) = B_x + B_{\text{osc}}\sin(\omega t)$ is added, with $\omega = 2\pi f$, the interdistances change periodically, which can generate locomotion. A spatio-temporal diagram illustrating the dynamics is given in Fig. 5.2 (c). Please note the phase shift in the elongation of oscillators a and b. Thanks to this phase shift, locomotion on the surface is possible. Indeed, despite a reciprocal evolution of $B_x(t)$, the subsequent dynamics of the beads is non-reciprocal.

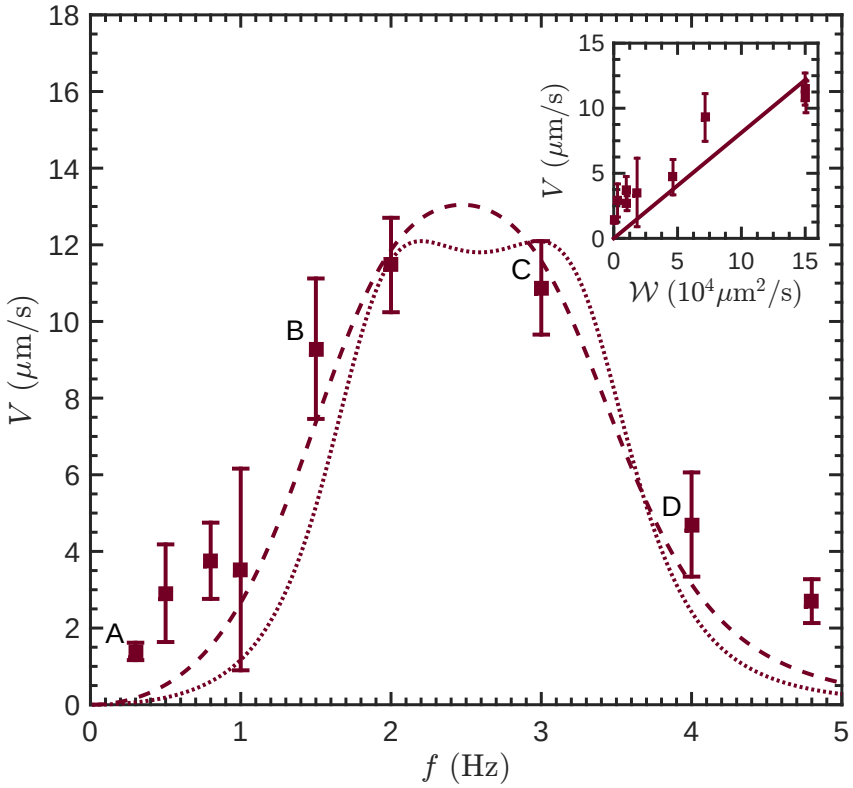

Fig. 5.3 Swimming speed. – The experimental speed V is plotted against the excitation frequency f. Error bars represent the standard deviation on three experiments. Dashed and dotted lines account for the model (Eq. (5.7)) with 397 µm spheres and 500 µm spheres respectively. The expected linear relationship between speed V and efficiency $\mathcal{W}$ is illustrated in the inset.

5.2.2 Results

Figure 5.3 shows the swimming speed as a function of the excitation frequency f. Each point is averaged over three independent experiments, for a total of 27 measurements. For each measurement, between 20 and 60 oscillation periods are recorded, depending on f. We have $B_z = 4.5\,\mathrm{mT}$, $B_{x,0} = 2.2\,\mathrm{mT}$ and $B_{\mathrm{osc}} \approx 0.5\,\mathrm{mT}$. For low frequencies, the speed is almost equal to zero. As the frequency f approaches the natural frequency of the oscillators, the speed increases. A maximum speed of around 12 µm/s is typically reached between 2 Hz and 3 Hz. Above 3 Hz, the speed drops drastically. Above 5 Hz, speed remains close to zero.

Note that if the amplitudes of the oscillating motions are too high, the swimmer can leave the region of stability of the collinear state, causing contact between the spheres or reaching the equilateral state [108]. This limits the possible values of amplitude B_{osc}, and, in turn, swimming speed. It is possible, however, to further increase B_{osc} by using a confinement potential to maintain the swimmer in the collinear state. By placing the swimmer in a rectangular dish, with a concave meniscus perpendicular to the swimming direction, we can obtain such a confinement. Higher speeds up to 76 µm/s were obtained in this case.

In the kinematic model of Najafi and Golestanian [23], the swimming speed is given by

$$V = \alpha A_a A_b \omega \sin\left(\phi_a - \phi_b\right) = \alpha \mathscr{W} \tag{5.1}$$

where A_a and A_b are the amplitudes of elongation and ϕ_a and ϕ_b are their respective phase relative to the external field. This means that the swimming direction is determined by the sign of $\phi_a - \phi_b$. We can define the swimming efficiency $\mathscr{W} = A_a A_b \omega \sin\left(\phi_a - \phi_b\right)$. The linear relationship between V and the experimentally measured value of $\mathscr{W}$ is plotted in the inset of Fig. 5.3. The proportionality coefficient α given by a fit on the

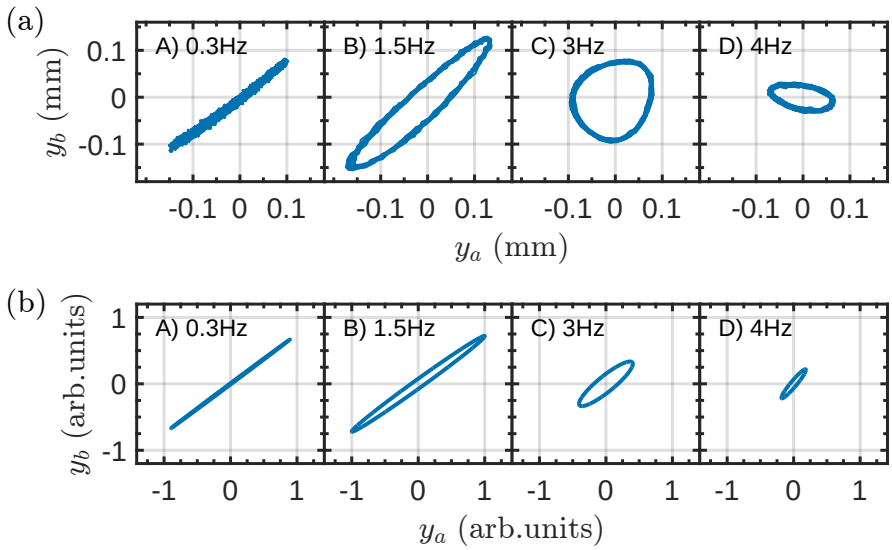

Fig. 5.4 Deformation cycles. – **(a) Experimental cycles** in the plane (y_a, y_b), for four values of the excitation frequency. **(b) Theoretical cycles** predicted by the model. Units are arbitrary, as the solutions depend linearly on the excitation amplitude.

experimental data is $\alpha_{\text{expt}} = 8.46 \pm 2.44 \times 10^{-5}$ μm^{-1}. According to [30], α can be expressed as a function of bead diameters and interdistances as

$$\begin{aligned} \alpha &= \frac{3D_1D_2D_3}{4\,(D_1+D_2+D_3)^2}\left[\frac{1}{L_a^2}+\frac{1}{L_b^2}-\frac{1}{(L_a+L_b)^2}\right] \\ &= \frac{21}{16}\frac{D_1D_2D_3}{(D_1+D_2+D_3)^2\,L^2} \end{aligned} \tag{5.2}$$

considering $L_a = L_b = L = 10^{-3}$ m. Using our experimental parameters, we find $\alpha_{\text{th}} = 6.68 \times 10^{-5}$ μm^{-1}, which lies in the 95 % confidence interval of the fit. As the spheres are partially immersed, we can correct the Stokes force by a factor 0.86 as determined in Eq. (4.12). By adding this correction to Eq. (5.2), we find $\alpha_{\text{th}} = 7.77 \times 10^{-5}$ μm^{-1}.

Experimental deformation cycles, in the plane defined by the elongations y_a and y_b, are depicted in Fig. 5.4 (a). The four cycles correspond to four points in Fig. 5.3. It can be shown that the area enclosed in the elliptical trajectory of the oscillators in the (y_a, y_b) plane is given by $\pi\mathscr{W}/\omega$ (see Appendix B). It is therefore proportional to the swimming speed. Cycle A shows that the oscillators are in phase at frequencies close to zero. This motion is reciprocal, such that the speed is also close to zero in Fig. 5.3. The cycles open up progressively, between 0.5 Hz and 3 Hz, resembling an ellipse as oscillators get out of phase. This is correlated with the increase in speed observed in Fig. 5.3. Around 3 Hz, oscillators are in quadrature and cycle C is approximately circular. This is the optimal phase for swimming, but not necessarily where the maximum speed is reached, as seen in Fig. 5.3. Indeed, oscillation amplitudes decrease with increasing frequency, which in turn decreases $\mathscr{W}$. At higher frequencies, the oscillators are close to being in phase opposition, as seen on cycle D. Furthermore, oscillation amplitudes decrease to zero, with the oscillation of bond 500-397 (y_b) decreasing faster than that of bond 500-500 (y_a). This is correlated with a decrease in speed in Fig. 5.3.

5.3 Model

Let us now investigate the model sketched in Fig. 5.2 (b), which consists of three particles linked by two linear springs. For the sake of simplicity, each particle has the same mass m and experiences the same viscous damping μ. Oscillators also have the same natural length. The Reynolds number in the experiment, as defined in Eq. (2.2), is typically comprised between 10^{-3} and 10^{-1}, meaning that the viscous dissipation dominates over inertia in the flow. However, the inertia of the particles is not neglected in the model. Indeed, the quality factor of each oscillator is close to 1, meaning that the oscillators are close to critical damping [102]. The equations of motion on

each particle are obtained via Newton's law

$$\begin{aligned} m\ddot{x}_1 + \mu\dot{x}_1 - k_a(x_2 - x_1 - L) &= -F\sin(\omega t), \\ m\ddot{x}_2 + \mu\dot{x}_2 + k_a(x_2 - x_1 - L) - k_b(x_3 - x_2 - L) &= 0, \\ m\ddot{x}_3 + \mu\dot{x}_3 + k_b(x_3 - x_2 - L) &= F\sin(\omega t), \end{aligned} \tag{5.3}$$

where $F\sin(\omega t)$ is the external forcing at angular frequency ω and amplitude F. This forcing is identical for each pair of beads. As expected, the central particle is not submitted to any net forcing. Please note that the sum of all internal and external forces is equal to zero. We will now study the oscillators in terms of the elongations y_a and y_b. Defining $\underline{t} = \omega t$, $\Omega_a = k_a/m\omega$, $\Omega_b = k_b/m\omega$ and $\beta = \mu/2m\omega$, one has

$$\begin{aligned} \overline{\overline{y}}_a + 2\beta\overline{y}_a + 2\Omega_a^2 y_a - \Omega_b^2 y_b &= \sin(\underline{t}), \\ \overline{\overline{y}}_b + 2\beta\overline{y}_b + 2\Omega_b^2 y_b - \Omega_a^2 y_a &= \sin(\underline{t}), \end{aligned} \tag{5.4}$$

where overlined symbols are differentiated by $\underline{t}$ and the elongations y are expressed in $m\omega^2/F$ units. The whole dynamics is described thanks to three dimensionless parameters: natural frequencies Ω_a and Ω_b, and viscous damping β. Those equations can be studied in a Fourier space by considering the complex amplitudes of oscillation $\hat{y}_a = A_a\exp(-i\phi_a)$ and $\hat{y}_b = A_b\exp(-i\phi_b)$. The solutions for both oscillators are

$$\hat{y}_{a,b} = \frac{3\Omega_{b,a}^2 - 1 - 2i\beta}{\left(2\Omega_a^2 - 1 - 2i\beta\right)\left(2\Omega_b^2 - 1 - 2i\beta\right) - \Omega_a^2\Omega_b^2}. \tag{5.5}$$

From this, we can find an expression for amplitude A and phase ϕ.

Figure 5.4 (b) shows cycles of deformation in the plane (y_a, y_b) for typical parameters encountered in the experiments [102]. Several features of the experimental cycles are recovered. Indeed, low frequency cycles are similar. Cycles gradually open up as frequency f is increased. The optimal phase difference is reached around 3 Hz. However, amplitude

decreases with f, such that speed is maximal between 2 Hz and 3 Hz, as will be shown below. At higher frequencies, the shape of the cycles are less accurately predicted, as can been seen on cycles C and D. However, the model considers three identical spheres and neglects hydrodynamic couplings. Indeed, around the resonance frequencies, there is typically a factor 10 between the hydrodynamic coupling and the restoring force. Both the effect of size on viscous drag and the presence of hydrodynamic interactions could explain why phase difference is larger in the experiment, especially at higher frequencies. It can be shown that the effect of the hydrodynamic coupling on the phase scales as ω. As observed experimentally, a non-reciprocal dynamics is observed despite the reciprocal evolution of the field $B_x(t)$. The toy model rationalises this observation: the distinct resonant frequencies f_a and f_b provide the spatial symmetry breaking required for the non-reciprocal deformation.

Let us quantify the velocity in the swimming regime as a function of the three dimensionless parameters. In the Fourier formalism, Eq. (5.1) reads

$$\mathscr{W} = \mathrm{Im}\left(\hat{y}_a^\dagger \hat{y}_b\right), \tag{5.6}$$

which leads to the following dimensionless expression

$$\mathscr{W} = \frac{6\beta\left(\Omega_b^2 - \Omega_a^2\right)}{\left|\Omega_a^2\Omega_b^2 - \left(\left(2\Omega_a^2 - 1\right) + 2i\beta\right)\left(\left(2\Omega_b^2 - 1\right) + 2i\beta\right)\right|^2}, \tag{5.7}$$

with i being the complex unit. Note that this equation is anti-symmetrical with respect to oscillators a and b and, consequently, leads to zero if both oscillators are identical. Indeed, in this case, the oscillations would be in phase. Note also that with no damping, *i.e.* with $\beta = 0$, the velocity is also zero, as expected. This equation also indicates the direction of motion, given by the sign of $\Omega_a^2 - \Omega_b^2$.

Figure 5.5 shows the effect of Ω_a and Ω_b on the efficiency $\mathscr{W}$ for two values of β. When β is close to zero, two sharp lines of high efficiency $\mathscr{W}$ are observed at $\Omega_{a,b} \approx 1/\sqrt{2} = \Omega_{a,b}^{\text{res}}$, due to the resonance of each oscillator. Speed is zero along the diagonal line $\Omega_a = \Omega_b$, corresponding to identical oscillators. As β increases, the maximum efficiency decreases roughly like β^{-2}. The optimal region widens and shifts towards higher values of Ω. This comes from the decrease in the oscillation amplitudes $\hat{y}_{a,b}$. Two points that correspond to two cycles of Fig. 5.4 are shown. They are in a diagonal line that is close, but distinct to the identity line. Each point is associated with a different value of β, as β is a function of the excitation frequency. As can been seen from their position in the graphs, cycles C and A correspond to an efficient and an inefficient swimmer, respectively.

The theoretical expression of $\mathscr{W}$ is compared to the experiment in Fig. 5.3. Experimental parameters are injected in Eq. (5.7), leaving no fitting parameter aside from a vertical scaling. One observes that the model reproduces correctly the experimental observations, despite the approximations made in order to reach an analytical expression for $\mathscr{W}$. As the model considers identical spheres, the predictions for both 397 µm and 500 µm spheres are shown.

The experiment was conducted with submillimeter-sized particles, which are on the larger end of the spectrum of low Reynolds swimming. One could wonder how efficiency $\mathscr{W}$ would be affected by a downscaling. Decreasing the size of the spheres and the distances between them changes the values of β as well as the resonance frequencies of the magnetocapillary bonds, as seen in Eq. (4.7) and Eq. (4.8). Let us assume that all length scales decrease with D and that forcing frequency remains close to the resonant frequencies. Thanks to dimensional analysis, one finds that the velocity of a magnetocapillary swimmer scales as $V \sim D^{-1}$. This suggests that a downscaled version of the swimmer would be able to propel itself effectively. However, particles smaller than 3.4 µm would experience a capillary

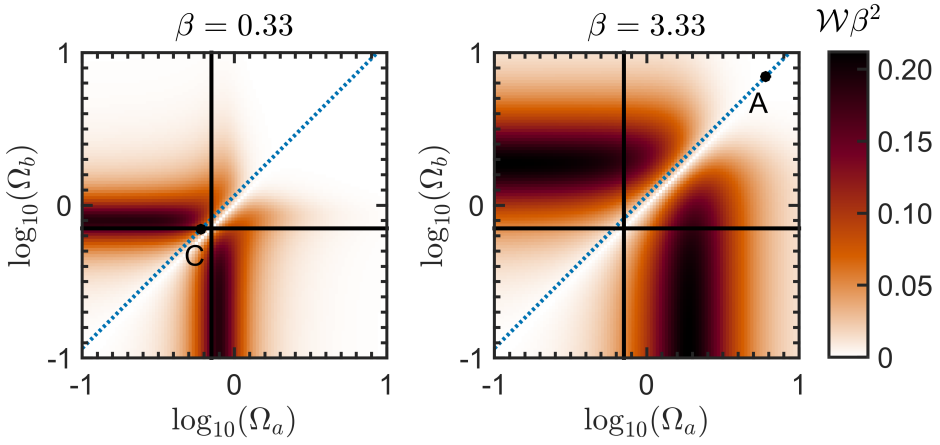

Fig. 5.5 Efficiency. – Theoretical prediction for efficiency $\mathcal{W}$ as a function of the dimensionless excitation frequencies. Two values of damping β are shown. The continuous lines represent the undamped resonance frequencies, while the dotted line represents a sweep of frequency f in the experiment. It is close, but distinct from the identity line. Two points corresponding to the cycles A and C of Fig. 5.4 are placed on each plot, as β is a function of f.

force weaker than thermal agitation, as discussed in Section 3.1.2. The deformation of the liquid surface around the particles could be enhanced to lower this bound, for instance through geometrical constraints, by using denser, more hydrophobic particles or by applying a vertical force other than gravity on the particles.

As linear springs are used to model the magnetocapillary bonds, the model remains general. The same approach could be applied to various systems, using other restoring forces. For instance, the same particles could be physically linked by an elastic material. This would allow experiments in the bulk and could prove more robust than a self-assembly. The model uses two different spring constants to generate the breaking of symmetry under a uniform forcing, which could also be obtained with materials of different elasticity. Furthermore, it can be shown that a similar spontaneous

phase shift can be obtained by using different viscous dampings and/or particle masses. This approach could serve to generate various assemblies more suited to technological applications requiring microswimmers, micromanipulators or micropumps.

5.4 Transient Regimes

As discussed in Chapter 3, the existence of an inertia-driven resonance in the oscillations of the particles is not necessarily in contradiction with the low-Reynolds-number approximation. Indeed, the Reynolds number of the flow (Eq. (2.2)) and the quality factor of the oscillator (Eq. (4.13)) are two distinct nondimensional numbers. One other way to phrase this is that a negligible fluid inertia is not the same as an infinite viscosity, such that the inertial forces of the harmonic oscillator can still be commensurable compared to viscous forces, even in the Stokes regime. In the case of magnetocapillary swimmers, one simple illustration of this is that the relatively high density of the particles compared to the surrounding fluid, *i.e.* $\rho_s/\rho_f \approx 8$, means that the inertia of the particles is about an order of magnitude higher than that of the fluid.

If we were to suddenly stop the driving force acting on a collinear swimmer, the particles could still oscillate slightly before going back to their equilibrium position. The residual stroke would translate into a residual speed. This is not the same as simply coasting in a fluid, and is in fact not incompatible with the hypothesis that we are in the Stokes regime. In order to measure this rather fine effect experimentally, it is necessary to improve the signal to noise ratio, as the speed of the collinear swimmer is typically quite small. To achieve this, several runs are performed on the same swimmer, submitted to the same oscillation for exactly 10 periods. The runs are then synchronised and the experimental variables averaged. Figures 5.6 (a) and (b) show the evolution of the distances of the outermost

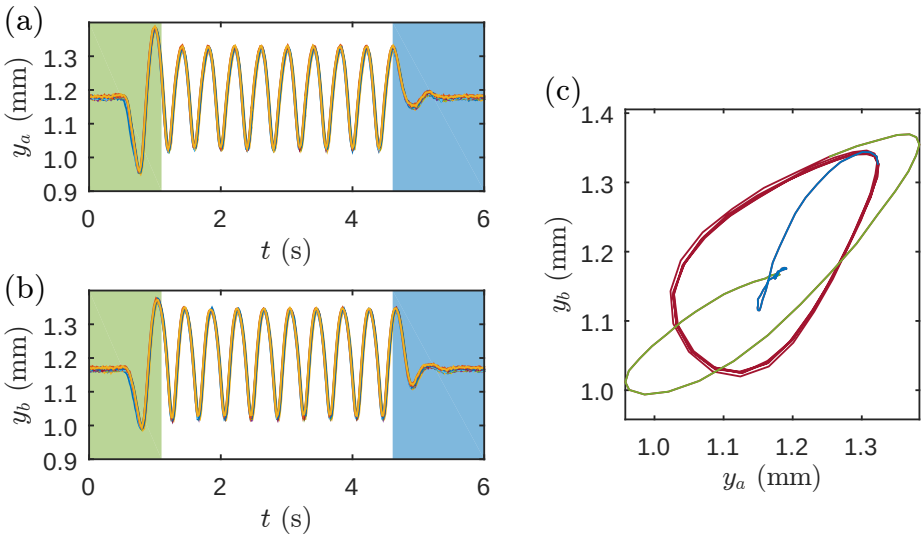

Fig. 5.6 Transient oscillations. – Oscillations of the arms of 10 collinear microswimmers submitted to exactly 10 oscillations of B_x. As seen in **(a)** and **(b)**, both arms experience a transient response. The cycle (y_a, y_b) for the average of the 10 swimmers is shown in **(c)**. The initial and final transient regimes are coloured green and blue, respectively.

beads to the central one, namely y_a and y_b. The 10 trajectories are almost identical. One can see that there is a slight phase difference between y_a and y_b. At the beginning of the 10 oscillations, which starts at $t \approx 0.5\,\mathrm{s}$, a transient regime can be observed, meaning that the oscillators are not completely overdamped.

In Fig. 5.6 (c), the trajectory in the plane (y_a, y_b) is shown for the average of the 10 experiments. The trajectory starts at the equilibrium position in the absence of oscillation, at the centre, then reaches the cycle for the 10 oscillations and finally goes back to the centre. The green curve corresponds to the green region in Figs. 5.6 (a) and (b), which is the initial transient regime. Conversely, the blue curve is the transient regime at the end of the oscillations and corresponds to the blue region in Figs. 5.6 (a) and (b). Overshoots are clearly visible during the transitions from static to

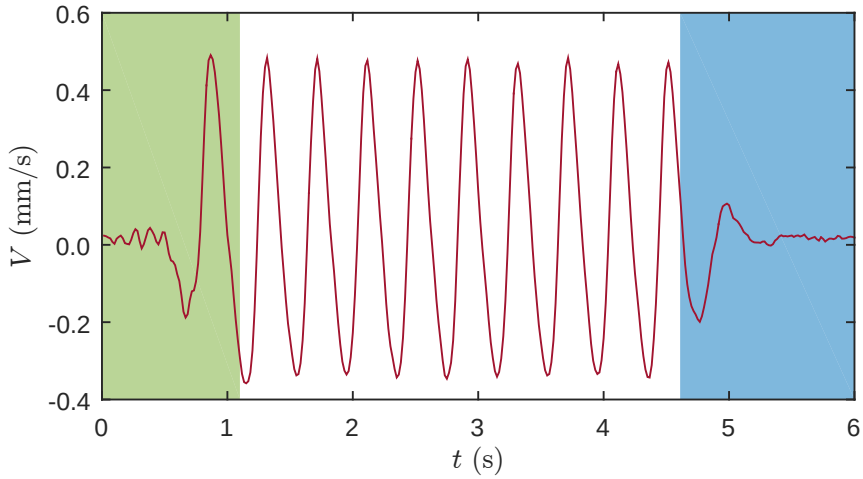

Fig. 5.7 Instantaneous speed. – The instantaneous speed also displays transient behaviours. Note that the speed is more often positive than negative, leading to a net displacement after one oscillation.

oscillating and oscillating to static, showing the influence of inertia in the transient regime.

It is also possible to see the transient regime in the swimming speed, as shown in Fig. 5.7. One can see that the speed of the centre of mass oscillates slightly after the forcing is stopped. This is where averaging the signal over several experiments becomes crucial. The position as a function of time is averaged, then filtered to further reduce noise before the derivative of the position is calculated. At the start of the oscillation, it takes about half a period for the speed to reach its equilibrium behaviour. In some cases, especially for higher amplitudes, an overshoot in the speed can also be observed. When the oscillation is stopped, there is a residual stroke for about one period that resembles the exponential decay of an underdamped harmonic oscillator.

During the forcing, one can observe that the speed is on average more positive than negative. Hence, there is a net displacement of the centre of mass over one period. But a strategy that involves moving backwards

during every oscillation might not be the most effective. This “two steps forwards, one step back” strategy is a consequence of the one-dimensional nature of the Najafi-Golestanian model.

5.5 Summary

In this chapter, we demonstrated the possibility for magnetocapillary self-assemblies to beat the scallop theorem and move along the interface. Three particles are placed in a collinear configuration, with one differently-sized external particle. This effectively behaves as a line of two magnetocapillary dimers with different spring constants and resonance frequencies. Because of this, a phase shift appears under an oscillating field. The deformation of the assembly is non-reciprocal and a net motion is observed. This method of locomotion is inspired by the model for a minimal swimmer proposed by Najafi and Golestanian, which had yet to be implemented experimentally. Some well-known theoretical results from this model have been verified, including the proportionality between the speed and the area of the cycle in the plane of the two degrees of freedom. This one-dimensional locomotion strategy is convenient for calculations, but relatively inefficient, partly because of the back-and-forth motion of the centre of mass. A swimmer that would follow a stroke causing it to move in the right direction at every step would be much more effective. This is where the triangular swimmer picks up.

6 Remote Control

In this chapter, we present another three-particle swimmer based on a triangular assembly. While its locomotion mechanism is more complex, it is faster and therefore more suited for potential applications than its collinear counterpart. Controlled trajectories are demonstrated, as well as typical applications such as cargo transport and mixing.

Partially published as

- G. Grosjean, M. Hubert, N. Vandewalle, Adv. Colloid Interface Sci. **255**, 84 (2018)
- G. Grosjean, M. Hubert, Y. Collard, S. Pillitteri, N. Vandewalle, Eur. Phys. J. E (in press)
- G. Grosjean, G. Lagubeau, A. Darras, M. Hubert, G. Lumay, N. Vandewalle, Sci. Rep. **5**, 16035 (2015)

6.1 Triangular Swimmers

6.1.1 Swimming Mechanism

The case of the triangular swimmer is more complex than the previously discussed collinear swimmer, if only because it is two-dimensional. All three particle pairs must be considered. Furthermore, because of the geometry, both radial and orthoradial modes discussed in Chapter 4 will be excited regardless of the orientation of the horizontal field. The lack of simplifying symmetry and the non-linearity of the interactions at play make it difficult to reach any analytical formulation. However, one can understand the origin of non-reciprocal motion when $\omega \ll 1$ by studying the effect of a quasistatic variation of B_x. While a hysteresis cycle was clearly identified in the transition between the triangular and collinear states, as shown in Fig. 3.3 (a), this cycle is not the one used to produce swimmers in the experiment. Indeed, a spontaneous transition from the triangular to the collinear state would only happen near the contact event, where any perturbation leads to the collapse of the swimmer. A more practical way of producing swimmers takes advantage of the coexistence of two isosceles states.

Indeed, several isosceles configurations can coexist, depending on the orientation of the triangle. Because of their similar shape, those states are not distinguished on Fig. 3.3 (a). Using a similar Monte-Carlo study, however, one can exhibit these two states by measuring the internal angles α_i, as shown in Fig. 6.1. One is a flat isosceles, called *platy*, with two angles below $\pi/3$ and one above (see (i) in Fig. 6.1). In this case, two of the three particles are perpendicular to B_x. A second configuration is a pointy isosceles, called *lepto*, with two angles above $\pi/3$ and one below (see (ii) in Fig. 6.1). In that case, two of the three particles are aligned with B_x. During a quasistatic increase of B_x, the assembly stays in the *platy* state up to $B_x/B_z \approx 0.35$, above which it switches to the *lepto* state.

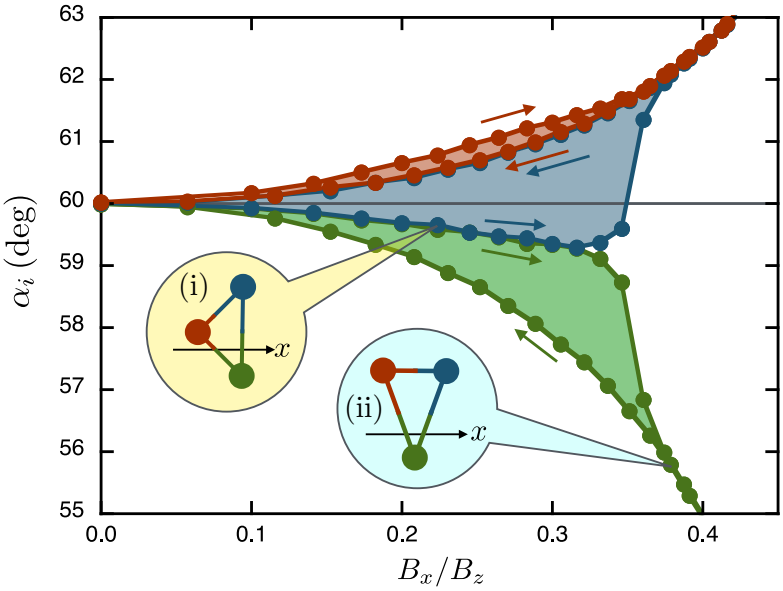

Fig. 6.1 Isosceles configurations. – A Monte-Carlo simulation of a quasistatic increase and decrease of B_x, similar to that of Fig. 3.3, highlights two isosceles states. Internal angles α_i are shown. The *platy* state (i) has two internal angles below $\pi/3$ and one above, while the *lepto* state (ii) has two angle above $\pi/3$ and one below. The switch from one state to the other, here around $B_x/B_x \approx 0.35$, is accompanied by a rotation of the triangle, leading to non-reciprocal motion.

When B_x is decreased back to zero, it remains in the *lepto* state. This hysteresis can therefore be solely attributed to the magnetic interaction. Frustration is inevitable in a triangular configuration, as individual pairs cannot all minimise their interaction energy. One can see from Fig. 6.1 that the transition between those two states must be accompanied by a rotation of the structure. However, deformation and rotation do not happen simultaneously, producing non-reciprocal motion. Note that, in contrast with the collinear swimmer, the triangular one can break time-reversal symmetry with three identical particles.

The motion of a typical triangular swimmer in the experiment is shown frame-by-frame in the bottom right corners of this thesis. Flipping the

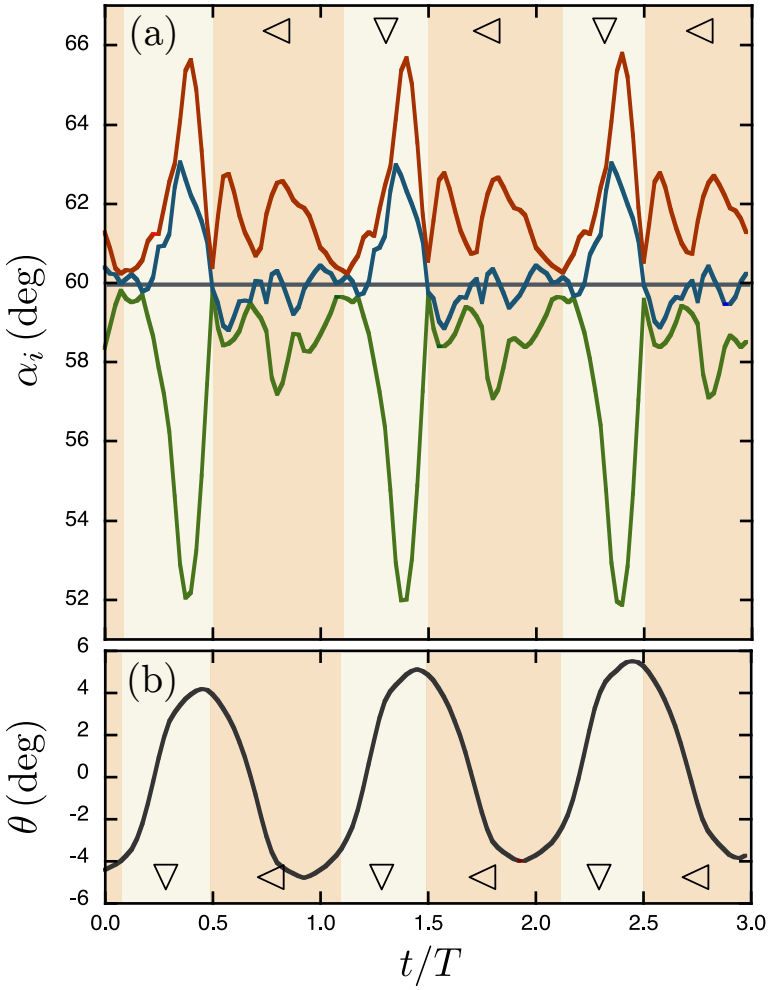

Fig. 6.2 Non-reciprocal motion in the experiment. – **(a)** Three periods T of the angles α_i with the same colour code as in Fig. 6.1, using experimental data. One observes that the blue curve oscillates between the red and green ones in each period. The system switches periodically between *lepto* and *platy* isosceles, respectively denoted $\triangledown$ and $\triangleleft$. **(b)** The angle θ of the whole structure during three periods. Oscillations are seen evidencing the successive switches.

pages at a rate of exactly 10 pages per second would depict the motion in real time. Figure 6.2 shows the evolution of α_i and the orientation θ, defined as the average orientation of the particles in the referential of the centre of mass, as a function of time for this particular swimmer. During roughly half of the oscillation, denoted $\triangledown$, the triangle is approximately a *lepto* isosceles and progressively rotates towards increasing θ. During the other half of the oscillation, denoted $\triangleleft$, the triangle is approximately a *platy* isosceles and rotates towards decreasing θ. Note that the *platy* state is far less pronounced, as the angles remain relatively close to 60°. Between these two phases, the triangle is almost equilateral, which corresponds to when the instant value of B_x approaches zero. This process is non-reciprocal, as the system remains in a given configuration as its change in orientation occurs. An experimental deformation cycle is shown in Fig. 6.3, side by side with a deformation cycle in the collinear case. The two degrees of freedom shown are the internal angle α, corresponding to the apex of the *lepto* triangle, and the orientation of the triangle θ.

However, non-reciprocity is a necessary, but not sufficient condition for swimming. The breaking of time-reversibility must translate into a net displacement. This precise mechanism is presented in Fig. 6.4. Suppose a regular triangle deforms into a *lepto* isosceles, then rotates. This rotation can be attributed to the small residual magnetism in each particle. A centre of rotation CR is defined by the hydrodynamic coupling between the spheres. Indeed, assuming each sphere rotates individually due to the magnetic field, the induced flow field leads to a force on the neighbouring particles. The resulting forces define a rotation centre. In a regular triangle, the centre of mass CM and the centre of rotation CR are identical. In the *lepto* case, CM is closer to the apex than CR. In the case of a *platy* isosceles, CM is further away from the apex than CR. This means that when three particles forming an isosceles triangle rotate, CM is displaced as it is distinct from CR. The effect of each configuration is complementary, as they

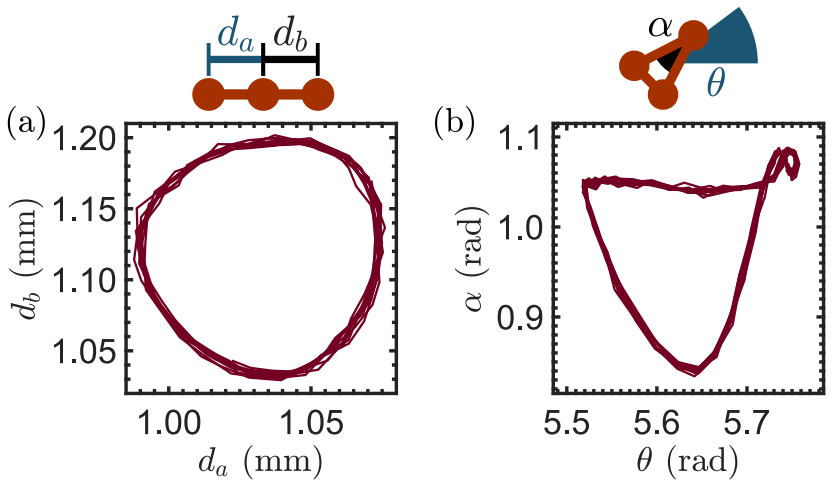

Fig. 6.3 Both three-particle swimmers. – **(a)** Interdistances d_1 and d_2 describe a non-reciprocal cycle for a collinear magnetocapillary swimmer. The experiment was run for ten oscillations at 3 Hz. **(b)** An internal angle α and the orientation of the swimmer θ also describe a non-reciprocal cycle for a triangular swimmer. Orientation θ is defined as the average of the orientations of the three particles in the referential of the centre of mass. Ten oscillations at 0.5 Hz are shown.

rotate in opposite directions. This contrasts with the less efficient "two steps forwards, one step back" motion of the collinear swimmer.

6.1.2 Control

One can wonder what is the direction followed by each swimmer. In the case of the collinear swimmer, the swimmer moves in alignment with the field, in the direction determined by the sign of the phase difference $\Delta\phi$. With triangular swimmers, however, swimming direction is generally at a non-trivial angle δ with the direction of $\vec{B}_x$. If $\vec{B}_x = B_x \sin(\omega t)\vec{e}_x$, and granted that there is a unique δ between 0 and $\pi/2$, by symmetry, we can expect at least four swimming directions depending on the initial orientation of the assembly, namely δ, $-\delta$, $\pi+\delta$ and $\pi-\delta$. This is usually the case with the triangular swimmer. Nonetheless, the trajectory of a

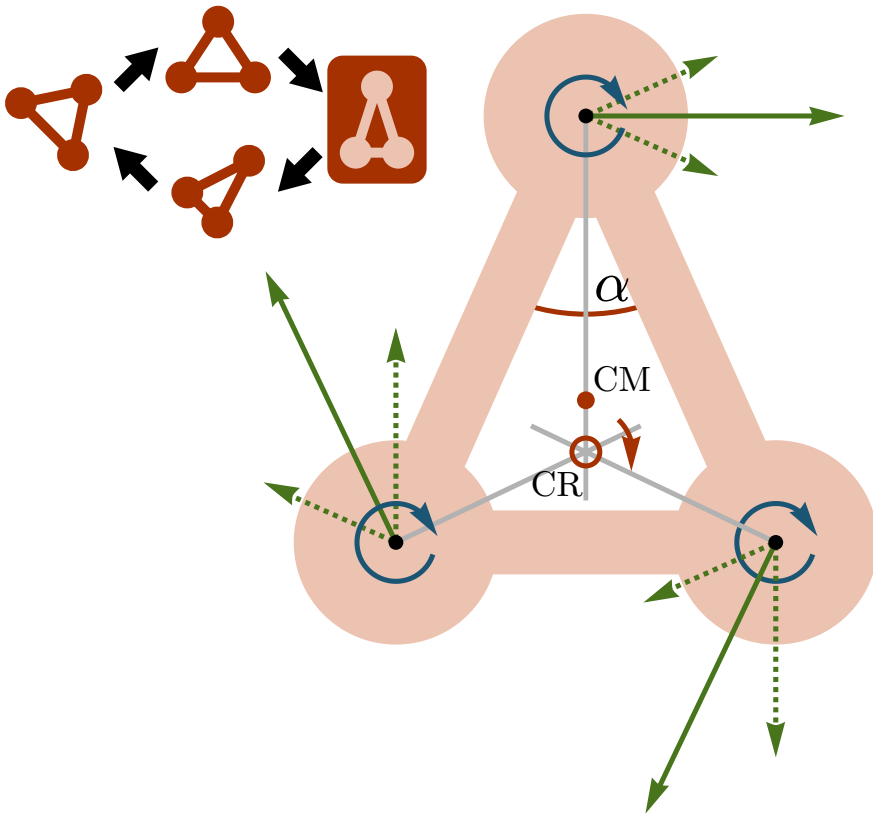

Fig. 6.4 Principle of the triangular swimmer. – The rotation-translation hydrodynamic coupling (dotted lines), caused by the individual rotation of the spheres, defines a rotation centre CR (red circle) that, in an isosceles of apex angle α, is distinct from the centre of mass CM (red dot). Therefore, the rotation leads to a displacement of CM that is preserved if the return rotation happens when the triangle is equilateral. CR moves closer or further away from the apex depending if $\alpha > \pi/3$ (*platy*) or $\alpha < \pi/3$ (*lepto*), respectively. In the experiment, the swimmer deforms into a *platy* isosceles during the return rotation, further increasing the effect.

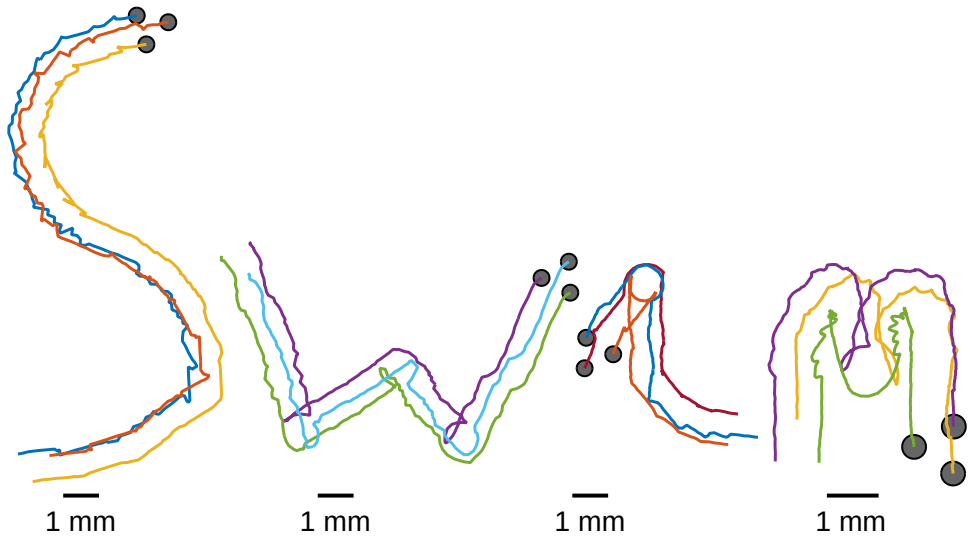

Fig. 6.5 Remote-control of a three-sphere swimmer. – The orientation of B_x is adjusted to change the swimming direction. Four trajectories, representing the letters “Swim", are shown to illustrate the level of control achieved. The letter “S" shows a smooth, curved trajectory. The “w" illustrates a succession of straight lines and sharp turns. The cursive “i" is a combination of a smooth turn and a sharp reorientation. Finally, the “m" shows all of the aforementioned movements in a small region of space.

triangular swimmer can be remote-controlled rather precisely, as shown on Fig. 6.5. Indeed, once a swimming direction δ is observed, changing the orientation of $\vec{B}_x$ by an angle ϵ changes the swimming direction to $\delta + \epsilon$.

In order to facilitate the control, an offset $B_{x,0}$ is added to $\vec{B}_x$ so that it does not oscillate around zero any more. A small offset of $1/10^{\text{th}}$ of the oscillation amplitude is enough to create a preferential orientation for the assembly on average, which helps keeping the swimmer in a well-defined swimming mode [28]. Figure 6.6 compares the probability distribution function of the speeds of a swimmer with and without the offset field, for a total of 55 experimental runs. One can see that without the offset, the speeds are more widely distributed, with the coexistence of several

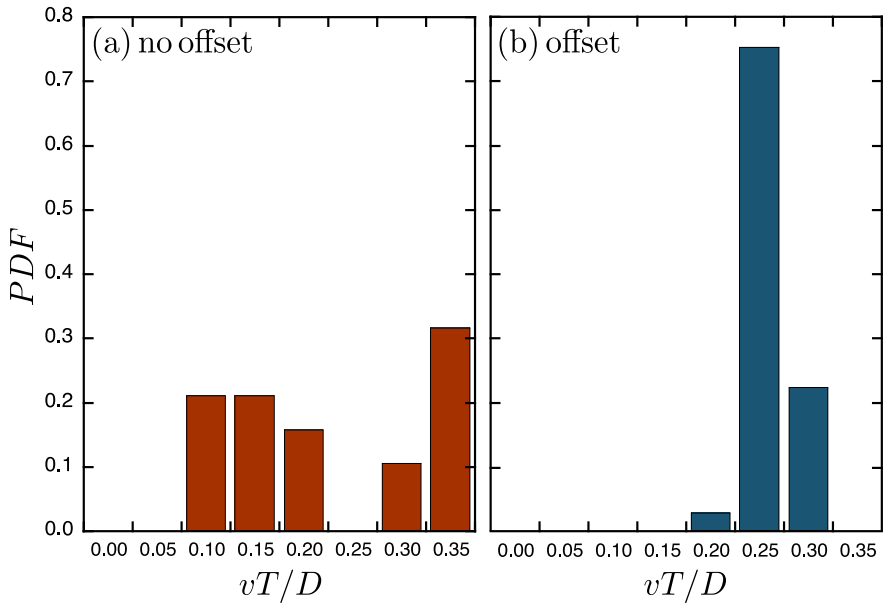

Fig. 6.6 Selection of swimming modes. – Probability distribution function (PDF) of normalised speeds obtained in similar experimental conditions, with $B_z = 3$ mT, $B_x = 0.75$ mT and $f = 0.5$ Hz, but **(a) without an offset** and **(b) with an offset** $B_{x,0} = 0.075$ mT. The speeds are obtained from 55 independent realisations.

modes for the same conditions. Compared to the collinear swimmer, higher speeds usually around 0.3 D/T are reached. The fastest triangular magnetocapillary swimmers in terms of dimensionless speed move at about 0.7 D/T, typically attained for parameters close to those in Fig. 6.6 but for amplitudes of $B_x \approx 1$ mT or higher. In terms of dimensional speed, the faster swimmers typically reach 600 µm s^{-1}, usually at higher frequencies $f \approx 3$ Hz. This relatively high speed explains why the triangular swimmer is used in remote-control experiments, despite the increased complexity. For comparison, the early example of artificial microswimmer in [24], which uses a magnetic filament for propulsion as depicted in Fig. 2.1 (vi), achieved a comparable top speed of around 0.1 L/T, where L is the length of the filament. Using the same definition for L, the speed of biological flagellates is typically quite low, of the order of 0.01 L/T [122]. This is explained by

the very fast rotation of the flagellum and the prevalence of absolute speed over energy efficiency in this case [4].

It is important to note that, while the quasistatic approach offers an intuitive explanation of the origin of reciprocal motion in the triangular case, it is not a definitive approach to characterise the swimmers. Indeed, dynamical effects play an important role in the deformation of the assemblies. For instance, no hysteresis loop is observed in the quasistatic deformation of a 4-particle swimmer, as was shown in Fig. 3.3. However, although initially thought to be poor swimmers [10], the 4-particle swimmers can reach similar speeds to the triangular swimmer, about 0.3 D/T. This shows the limit of the quasistatic approach and the necessity of studying the interaction dynamics in more detail.

6.2 Applications

Magnetocapillary swimmers have some unique characteristics that set them apart from other artificial microswimmers, which could be beneficial from the points of view of both fundamental and applied research. Notably, they are bound to an interface, self-assembled from simple components, chemically inert and fuelless, while being relatively fast and controllable. Naturally, many challenges remain to be addressed before any actual technological application can be considered for microswimmers in general, and magnetocapillary self-assemblies in particular. Nonetheless, performing some simple tasks with the swimmer can serve as a proof of concept for future applications as well as a basis for further studies. Several applications are commonly cited for microswimmers, notably concerning the manipulation and transport of micro-objects [13, 24, 91, 123–130] and the mixing and pumping of fluids [13, 22, 131–134]. Other applications could make use of the magnetic properties of the spheres. For example, it is possible to produce targeted heating in a fluid using magnetic particles

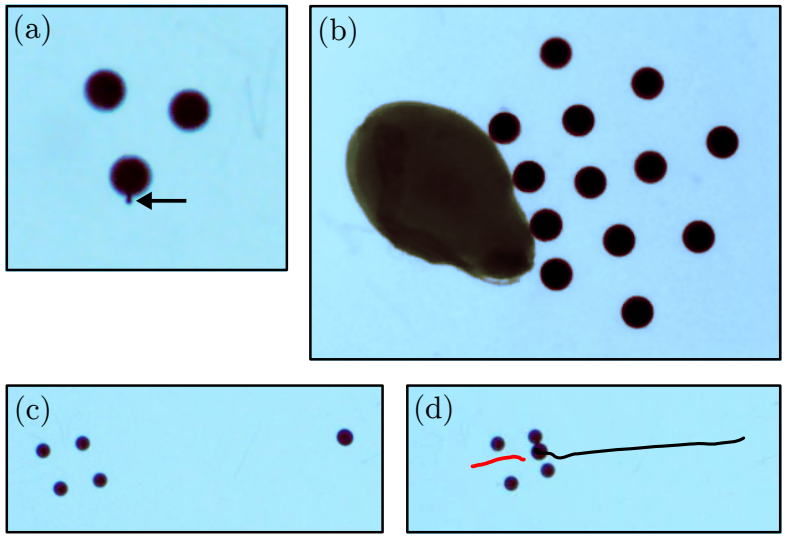

Fig. 6.7 Capture by Cheerios effect. – Objects of various sizes can be captured, such as a polyethylene sphere of 80 µm **(a)** or a sesame seed of 3.7 mm **(b)**. **(c)** A 4-particle swimmer is brought in the proximity of a polyethylene sphere of about 600 µm. **(d)** After about 15 s, the sphere is captured by the swimmer through capillary attraction. Lines show the motions of their centre of mass.

under high frequency oscillating fields, which has long been studied for cancer treatment [135]. The heating of a floating particle, in this case by a laser, has also been used to manipulate objects on a water surface by locally changing surface tension [63]. This technique could be applied to magnetocapillary assemblies to provide greater control. In this section, two experiments are performed and discussed in order to illustrate how magnetocapillary swimmers could perform two simple tasks : the transport of an object and the local mixing of fluids.

One of the main tasks proposed for microswimmers is the transport and delivery of a cargo [13, 91, 123–130]. Indeed, the controlled transport of a micro-object could potentially be used in microfabrication, manipulation of biological components or targeted drug delivery [125, 128–130, 136]. The

transport process can be divided into three steps: the capture, the towing and the release of the cargo.

The capture of a floating object by a magnetocapillary swimmer can be relatively straightforward by using capillary forces, granted that the swimmer and the object possess capillary charges of the same sign. In other words, in the proximity of the swimmer, the metallic spheres naturally attract objects that produce a concave meniscus, which is the case for most heavier than water objects. The capture of several floating objects by swimmers made of 500 µm particles is shown on Fig. 6.7. This capture process has been successfully tested on various particles sizes, including a polyethylene sphere of about 80 µm (see Fig. 6.7 (a)) and a sesame seed about 3.7 mm long (see Fig. 6.7 (b)). Finally, the capture of a polyethylene sphere of 600 µm is shown in Figs 6.7 (c) and (d). Note that a particle having a capillary charge of the opposite sign as the swimmer would experience a repulsion and be pushed away from the swimmer in a way that would be difficult to precisely control. Nonetheless, capture could still be achieved. For example, the swimmer could capture an intermediate, amphiphilic particle, possessing both negative and positive capillary poles [7, 101]. Capillary gripping has been proven to work in other systems using bubbles [137] or droplets [138] as intermediary, although this does not rely on the Cheerios effect. Furthermore, by introducing defects in the contact line of the spheres, one could produce a directed capture at a specific site on the object [139]. Finally, it might be possible to change the sign of the capillary charge of the swimmer by using another body force opposing gravity, for example with a vertical magnetic gradient [106, 140].

The main drawback of the capillary interaction as a capture method is its lack of selectivity. Any particle possessing a capillary charge of the same sign as the swimmer will be attracted when it comes in proximity with the swimmer. This does not present a problem, though, if the intended goal is to collect as many floating particle as possible, for example in pollution

removal applications [141]. A possible strategy to obtain a selective capture by capillary interaction would be to code a specific succession of capillary poles on the particles, by forming an undulated contact line or using non-spherical particles [100, 142–144], matching the code of the target particle. However, most applications requiring the selective capture of a target or the capture of objects possessing capillary charges close to zero would necessitate other methods. It has been shown that a cargo can be kept close to the swimmer during transport by hydrodynamic interaction alone [145]. Note that because magnetocapillary swimmers are chemically inert, and their locomotion is not based on a chemical interaction with their environment, coating the particles to obtain desired properties [146] is an option. For example, targeted delivery of genes using magnetic swimmers coated with a reagent has already shown promising results in the case of artificial bacterial flagella [147].

The second step of the transport process is the cargo towing itself. Depending on the size of the load relative to the swimmer, this can vary from a trivial matter to a very complex problem. If L denotes the typical length of the cargo, an object such that $L \ll D$, as in Fig. 6.7 (a), will have little influence on the deformation of the swimmer and the resulting fluid flow. On the other hand, the case of a cargo much larger than the particles, *i.e.* $L \gg D$, is significantly more complex. The motion of several particles can be impeded by the cargo, which means that a larger number of particles is needed to produce non-reciprocal deformations. For example, in Fig. 6.7 (b), 13 particles have been used to capture a 3.7 mm long sesame seed. Finding efficient swimming regimes in assemblies with a large number of particles remains an open question. Indeed, each subgroup of particles in the assembly would need to work in synergy, generating a net flow in the same global direction, in order to overcome the increased drag. This is usually not the case in the experiment. With the sesame seed of Fig. 6.7 (b), only low speeds of the order of $10^{-2}\ D/T$ were observed.

The case of large cargoes should be further investigated, in particular to determine what the optimal number of particles is, depending on L and D.

When $L \approx D$ (as in Figs 6.7 (c) and (d)) the cargo can more or less influence the motion of the particles depending on the situation. Figure 6.8 (a) shows the towing by a 4-particle swimmer of a 600 µm polyethylene sphere over one period of the oscillating field at 0.5 Hz. The deformation of the swimmer is superimposed to the initial configuration at $t = 0$, in order to highlight the displacement of each particle after each time step of $T/5$. The load is in contact with a single magnetic particle. Its motion evidences a rotation of the particle in question, showing that its movement is relatively unhampered by the presence of the cargo, in spite of the added mass and viscous drag. It is not impossible that the presence of the cargo may actually improve propulsion, as evidenced by the relatively large swimming speed of about 0.5 D/T. This might be an effect of the large amplitude of motion of the cargo. Furthermore, it is has been shown numerically that an arbitrary swimmer loaded with a cargo can move faster than an unloaded one in some conditions [124]. Namely, an optimal size ratio between a swimmer and a cargo can exist where swimming efficiency is significantly improved, granted that the cargo be sufficiently close to the swimmer.

Figure 6.8 (b) shows the towing of a similar polyethylene sphere, following the capture which was shown in Figs 6.7 (c) and (d). In this case, the sphere is in contact with two particles of the assembly. This has the effect of creating a solid link between those particles, restricting their motion. However, non-reciprocal motion is still observed, leading to a swimming speed of about 0.25 D/T. In both situations, swimming trajectory is controllable. Figure 6.8 (c) shows the transport of the cargo on a small loop. Every turn corresponds to a change in the direction of the oscillating field $\vec{B}_x$, with the exception of a small notch in the trajectory (*). This notch corresponds to the moment the cargo detached from a particle and came into contact

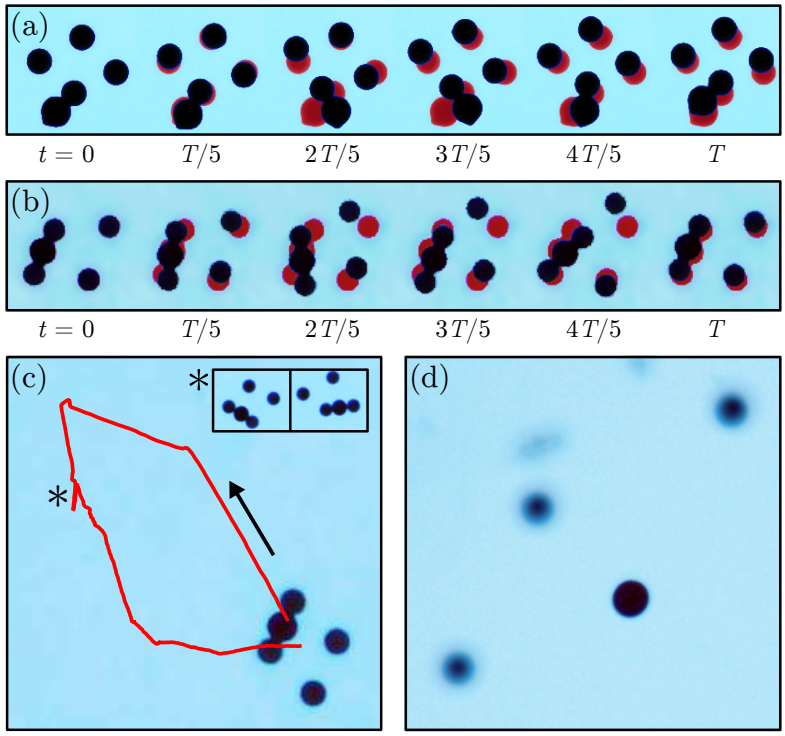

Fig. 6.8 Transport. – Towing and release of a floating particle. **(a)** Under a sinusoidal field $B_x(t)$, the assembly and cargo swim. Non-reciprocal deformations are shown over one period of the oscillating field $T = 2$ s. **(b)** Same as in (a), following the capture shown in Fig. 6.7. In this case, the cargo is stuck between two particles. **(c)** Nonetheless, swimming direction is controllable. Here, the cargo is moved then brought back to its initial position. A notch in the trajectory (*) happened when the cargo jumped from one particle pair to another, as shown on the insert. **(d)** The non-magnetic cargo is released by sinking the metallic spheres using a non-uniform magnetic field, *i.e.* by approaching a neodymium magnet.

with another one. Despite this perturbation, the swimmer was successfully brought back to its starting position.

The last step of a transport experiment is the release of the load. If the cargo possesses a sufficiently large magnetic susceptibility, a strong vertical magnetic field will move the particles and cargo away from each other, freeing the load. On the other hand, if the magnetic susceptibility of the cargo is small compared to that of the particles, as is the case with the polyethylene sphere, a strong vertical magnetic gradient can sink the metallic spheres while the cargo stays afloat. This was done in Fig. 6.8 (d) by approaching a neodymium magnet from below the bath. The sphere in the foreground is the polyethylene cargo, while three of the four particles constituting the swimmer can be seen in the background, out of focus.

Another commonly cited application of microswimmers is mixing at the microscale [13, 22, 131–134]. For instance, swarms of microswimmers can enhance the diffusion of constituents in a fluid [131] or the mixing of several fluids in microfluidic devices [132, 133]. In general, a microswimmer generates fluid motion over a long range, producing stirring. This stirring effect is most pronounced if swimming direction is frequently changed in a random way, in a so-called run and tumble motion [22, 148]. In the case of a remote-controlled artificial microswimmer like the magnetocapillary swimmer, parameters such as the typical run length between reorientations, the distribution of run lengths and the smoothness of the turns can be varied at will.

Another possibility is to generate local stirring by rotational motion or motion on a closed loop [134]. This could prove useful in confined environments, such as small droplets or microfluidic devices, where stirring by run and tumble motion loses efficiency [149]. Furthermore, assembling an array of rotating objects has been shown to be a viable strategy for mixing in microfluidic devices [150]. Indeed, like the Reynolds number, the relative importance of advection and diffusion in a fluid, called the Péclet

number, is proportional to the typical length scale and velocity of the flow. Therefore, at the microscale, molecular diffusion becomes the preferred mixing mechanism over advection. In this case, the volume of fluid mixed can be defined as

$$V = \mathscr{A}\sqrt{Dt} \tag{6.1}$$

where D is the mass diffusion coefficient and $\mathscr{A}$ the contact area between the fluids to mix [150]. Maximising contact area $\mathscr{A}$ is therefore a possible mixing strategy. With this aim in mind, an investigation of the rotational regimes of magnetocapillary swimmers and their possible use as a micromixing device could prove useful. The simplest way to produce rotational motion in a magnetocapillary swimmer is to submit it to a strong magnetic field rotating in the horizontal plane, causing the particles to come into contact and rotate. In Fig. 6.9, a triangular swimmer has been brought to the intersection of three fluids, each being the same mixture of water and glycerol with the addition of a red, a yellow and a blue dye. A strong horizontal field B_x causes the particles to come into contact and form a line. This magnetic rod follows the orientation of the horizontal field in the manner of a compass needle. We can therefore use a magnetic field rotating in the plane of the interface

$$\vec{B}_{\text{rot}} = B_x \cos(\omega t)\,\vec{e}_x + B_y \sin(\omega t)\,\vec{e}_y, \tag{6.2}$$

where we choose $B_x = B_y$, to rotate the rod. After about 8 clockwise turns ($\omega < 0$) of the magnetic field, fluid close to the swimmer has been entrained, forming a spiral. Contact area $\mathscr{A}$ has increased, as thin layers of each colour were intertwined (see white arrow on panel (c)). The direction of rotation of $\vec{B}_{\text{rot}}$ is then inverted ($\omega > 0$) to rotate the rod about 8 turns counter-clockwise. On a circle of roughly the size of the swimmer, mixing by molecular diffusion has occurred, as evidenced by the grey area around the particles (see white arrow on panel (d)). Further away from the swimmer,

the fluid is back to its initial position due to the reversibility of laminar flows (see black arrows). This simple mixing device illustrates the potential of artificial microswimmers to produce mixing at specific locations.

6.3 Summary

A much faster swimmer, compared to the collinear one, moves by going back and forth between two isosceles configurations while rotating. This stroke is efficient, as the whole deformation sequence contributes to moving in the same direction. Once a stable and fast swimming mode is found, controlling the trajectory becomes rather easy. The orientation of the oscillating field is simply varied, allowing to move the swimmer in any direction. Precise control is an important step towards potential applications. The feasibility of two often-cited applications for microswimmers has been demonstrated. The first is cargo transport. Floating objects can be captured by Cheerios effect and moved along the interface, then finally released by selectively sinking the magnetic particles. To adapt this method to larger cargoes, however, would require to understand and master the motion of many-particle assemblies. The second application discussed is micromixing. Microswimmers have the potential to efficiently mix tiny quantities of fluid, in a regime where advection and turbulence cannot be used. This was demonstrated by forming a simple rotating rod from a triangular assembly. However, mixing fluids without causing the spheres to come into irreversible contact could be a more effective strategy, as fluid would be entrained between the particles. One can wonder if, similarly to the swimming regimes, a rotational motion could also be obtained from the non-reciprocal motion of the particle.

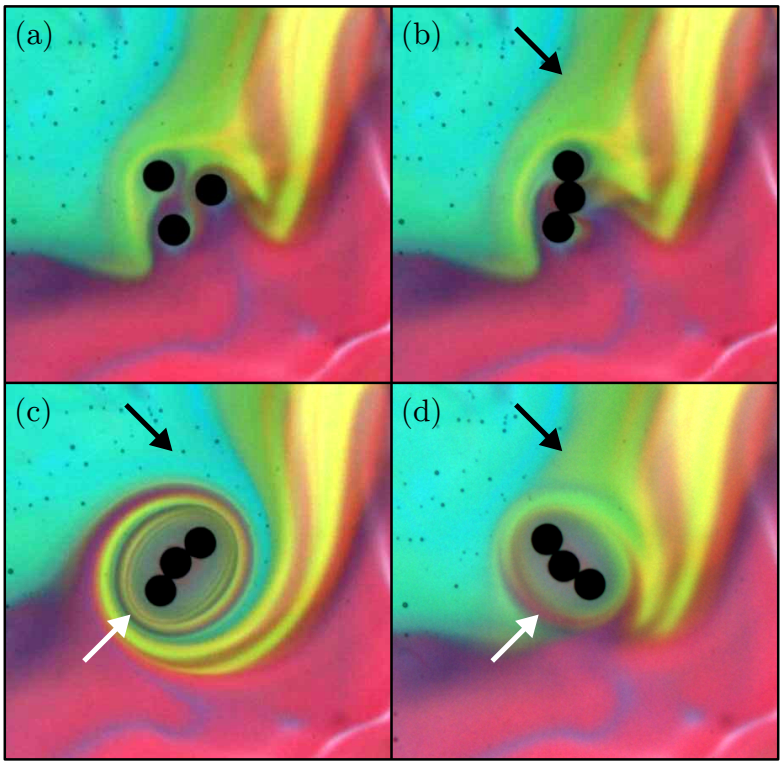

Fig. 6.9 Simple mixing device. – **(a)** A triangular swimmer is moved to the intersection of three fluids, each a glycerol-water mixture with a red, yellow or blue dye. **(b)** A large B_x is used so that the particles collapse in a line. **(c)** $\vec{B}_{\text{rot}}$ is rotated for about 8 turns clockwise. Fluid is entrained as the line follows the rotation of $\vec{B}_{\text{rot}}$. **(d)** $\vec{B}_{\text{rot}}$ is rotated for about 8 turns counter-clockwise. Far from the particles, the flow is reversible (black arrow). Close to the particles, however, mixing has occurred due to molecular diffusion (white arrow).

7 ROTATIONS

In this chapter, we study the influence of a rotating magnetic field on magnetocapillary assemblies. This could improve our understanding of the dynamics of magnetocapillary swimmers, as well as lead to more efficient micromixers. Various rotational regimes are identified, with different underlying mechanisms. Indeed, the rotation can be powered by the individual rotations of the particles, the pairwise alignment of the dipoles with regards to the external field, or the deformations of the assembly.

Partially published as

- G. Grosjean, Y. Collard, M. Hubert, A. Sukhov, J. Harting, A.S. Smith, N. Vandewalle, *Capillary assemblies in a rotating magnetic field*, in preparation (2018)

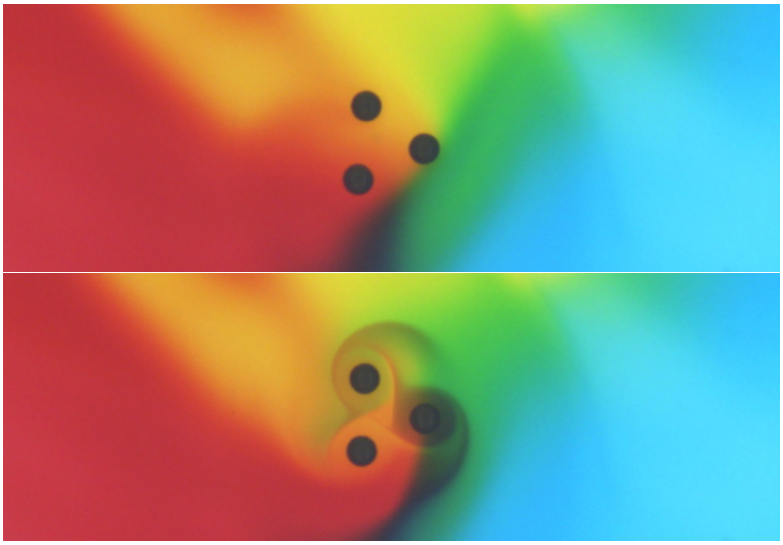

Fig. 7.1 Rotation of a triangular assembly. – A triangular assembly of 500 µm particles is submitted to a horizontal field rotating at 1 Hz. After 8.8 s, the assembly has rotated of about $2\pi/3$ (bottom picture). Dyes allow to see the fluid motion due to both the rotation of the whole assembly and the individual rotations of the particles. Credits: Ylona Collard.

7.1 Dynamics of a Triangular Assembly

Studying the influence of a rotating magnetic field on magnetocapillary assemblies could bring some valuable information. For instance, the stroke of the triangular swimmer discussed in Chapter 6 relies on a spontaneous rotation of the triangle. However, why the assembly would rotate in the first place has yet to be discussed. Furthermore, the existence of rotational modes could allow to mix fluids in a localised space more efficiently than a simple rotating rod such as the one from Fig. 6.9. Figure 7.1 shows a triangular assembly submitted to a magnetic field rotating in the horizontal plane at a frequency of 1 Hz. Some dye has been added to the liquid to visualise the flow. One can see that fluid is entrained around each particle, evidencing a rotation of the individual spheres additional to the rotation of

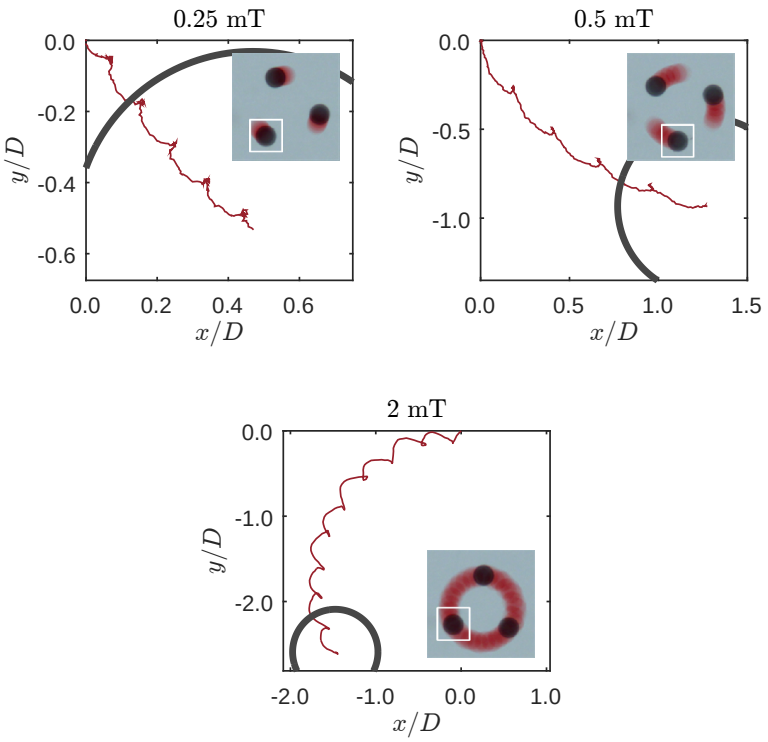

Fig. 7.2 Rotation trajectories. – Trajectories, over 5 s, of a particle of diameter $D = 500\,\mu\text{m}$ in an assembly submitted to a vertical field $B_z = 4.9\,\text{mT}$ and a horizontal field B_x rotating at a frequency $f = 1\,\text{Hz}$, for three values of the amplitude B_x. The insets show the trajectory for the whole assembly, with the corresponding particle in a white box.

the whole assembly. Not only does this cause the dye to swirl around the particles, further stirring the fluid, but it also demonstrates a mechanism that is not explained by considering that the particles possess a simple induced magnetic dipole proportional to the external field. Studying the motion of magnetocapillary assemblies under a rotating field might therefore prove crucial for both the development of possible applications and our fundamental understanding of these systems.

When submitted to a horizontal rotating field

$$\vec{B}_{\text{rot}} = B_x \left(\cos(\omega t)\, \vec{e}_x + \sin(\omega t)\, \vec{e}_y \right), \tag{7.1}$$

a triangular assembly proceeds to rotate. The angular frequency of the field $\omega = 2\pi f$ is chosen to be positive. If we denote the average rotation speed of the assembly Ω, in general we have $0 < \Omega < \omega$. Figure 7.2 shows the overall motion of the assembly over 5 s, as well as the trajectory of one of the three particles in more detail. Three values of the horizontal amplitude B_x are shown: 0.25 mT, 0.5 mT and 2 mT. It can be seen that an increase in B_x leads to an increase in the rotation speed. The trajectory of each particle resembles an epicycloid, globally following a circle but punctuated by periodical cusps corresponding to each passing of the field. For larger values of B_x, the frequency of the cusps is doubled. This suggests the existence of various regimes.

These changes in regime should have consequences on the rotation speed. Let us sweep through the control parameters. First, Fig. 7.3 shows the dimensionless rotation speed $\Omega/2\pi f$ as a function of the excitation frequency f. At very low frequencies, we have $\Omega/2\pi f = 1$, meaning that the rotational motion of the assembly simply follows the external field. The assembly essentially behaves like a solid structure that keeps its orientation with regards to the field. For frequencies of 0.05 Hz and above, we always have $\Omega/2\pi f < 1$. While the external field powers the rotational motion, the assembly no longer simply follows it. We can further distinguish between two regimes. Between 0.05 Hz and 1.5 Hz, we have an increase of Ω with f that follows a power law of one third, or $\Omega/2\pi f \propto f^{-2/3}$. After reaching a maximum at roughly 1.5 Hz, Ω then decreases quadratically, corresponding to $\Omega/2\pi f \propto f^{-3}$.

As in Fig. 7.2, we can expect to observe various rotational modes depending on the amplitude of the forcing. Figure 7.4 shows the rotational speed Ω, now in its dimensional form, as a function of the amplitude B_x.

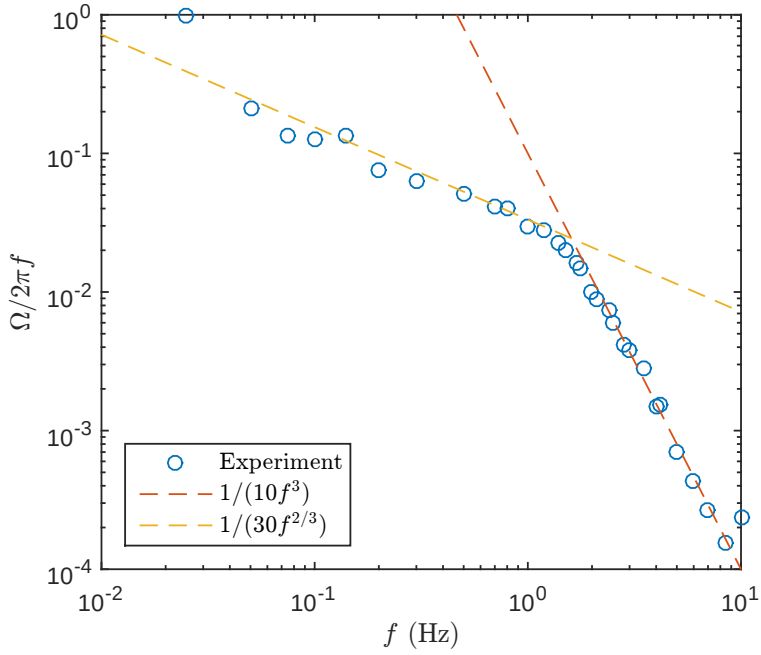

Fig. 7.3 Influence of the frequency. – Dimensionless rotation speed of the assembly $\Omega/2\pi f$ as a function of the forcing frequency f. At the lowest frequency $f = 0.025$ Hz, the assembly follows the external field. Two power laws are shown. We have $\Omega/2\pi f \propto f^{-2/3}$ and $\Omega/2\pi f \propto f^{-3}$, respectively below and above $f \approx 1.5$ Hz.

The experiment was performed for three values of f. One can see that at low amplitudes ($B_x < 0.5$ mT), the rotational speed is roughly proportional to B_x, with very little influence of the excitation frequency. Higher amplitudes lead to a much more nonlinear behaviour, with local maxima and a much more pronounced dependence on the applied frequency. The results from Fig. 7.3 lie in this regime, with an amplitude of 0.7 mT.

While the study of the fine interplay of B_x and f would require a more thorough exploration of the parameter space, a regime already stands out that leads to much higher values of Ω. Indeed, for the highest values of B_x and f, the rotation speed dramatically increases, as shown in the inset of Fig. 7.4. This regime is discussed in Fig. 7.5. It is characterised by much

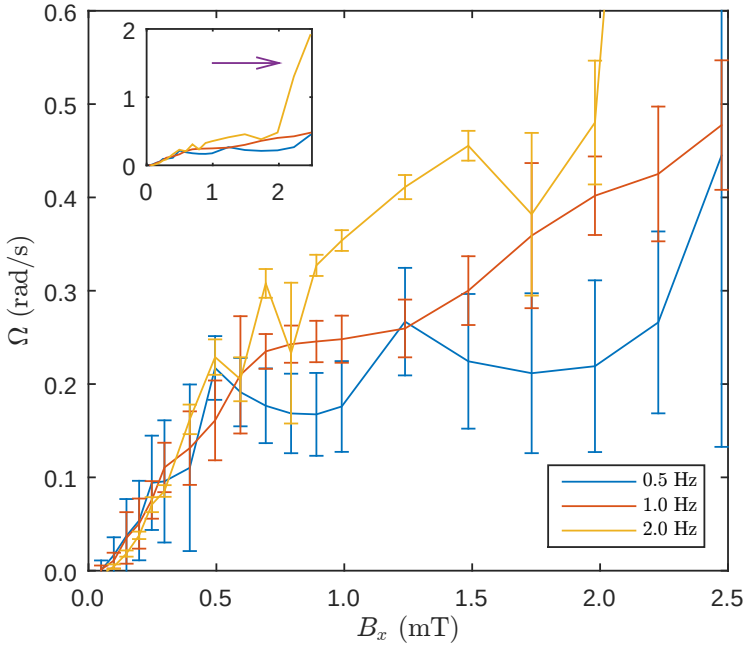

Fig. 7.4 Influence of the amplitude. – Rotation speed Ω as a function of the amplitude B_x, for three values of f. The inset shows the same plot with an extended y-axis. One can see that the high-frequency, high-amplitude regime (see arrow) leads to significantly higher rotation speeds.

larger deformations, somewhat resembling a juggling pattern. Typically, the particles oscillate sinusoidally, each separated by a phase of $2\pi/3$, as seen in the temporal evolutions of r and θ. The radial and angular components are roughly in phase quadrature, so that the particles follow open cycles in the (r,θ) plane.

Let us now perform once again the study of Fig. 7.4, this time focusing more closely on this "juggling" mode. In Fig. 7.6, the dimensionless rotational speed is measured in the high-amplitude, high-frequency regime. At lower amplitudes, we have roughly $\Omega/2\pi f \approx 0.2$. Right before the particles come into contact, the speed drastically increases. This is accompanied by much larger deformations like those shown in Fig. 7.5. The theoretical

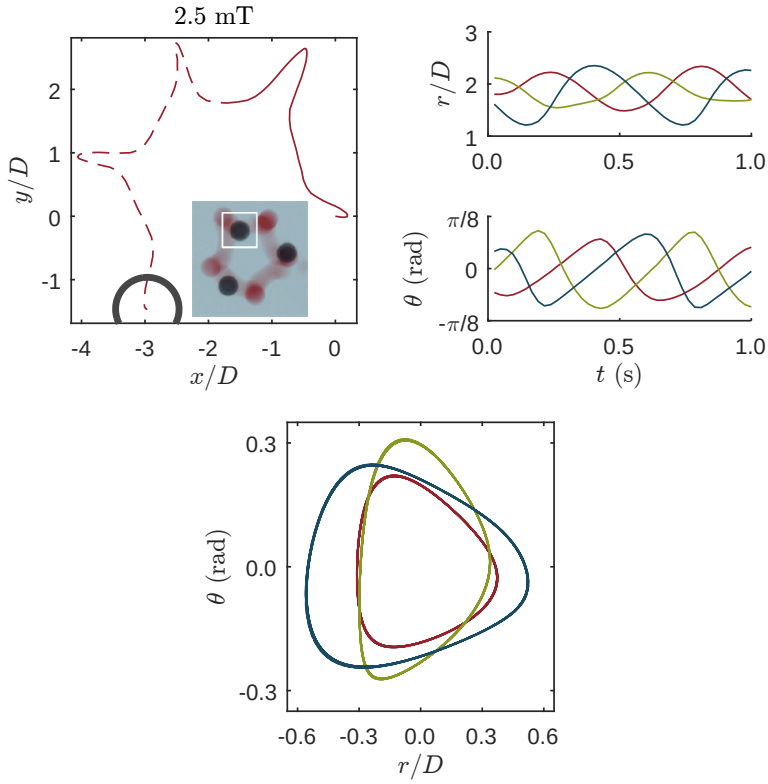

Fig. 7.5 High-deformation "juggling" regime. – In the upper left, trajectory over 2.5 s of a particle submitted to a field of amplitude $B_x = 2.5$ mT and frequency $f = 2$ Hz. The inset shows the trajectory of the whole assembly for only the first second, corresponding to the solid line in the plot. In the upper right, positions of the three particles in the assembly in polar coordinates over 1 s. In the bottom, cycles in the plane defined by the polar coordinates for the three particles over 20 s.

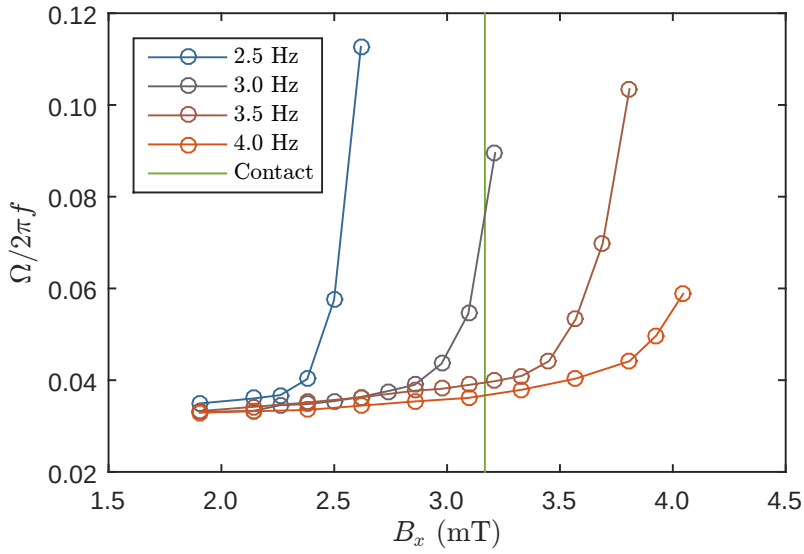

Fig. 7.6 Rotational speed of the "juggling" mode. – The rotational speed increases dramatically in the high-deformation regime, right before the particles come into contact. The green line shows the theoretical contact threshold as calculated from Eq. (3.13).

value for the collapse of the assembly is also shown. One can see that, for excitation frequencies larger than 3 Hz, the "juggling" mode can persist above the theoretical collapse. Indeed, a static B_x field of more than 3.2 mT would cause the particles to come into contact. This indicates that the particles are not at equilibrium, and thus that the inertia of the particles might play a role.

7.2 Discussion

7.2.1 Individual Rotations

Three mechanisms should be accounted for in order to explain the rotation of the assembly. First, the rotation can be driven by the individual rotations

of the particles. These particles exhibit very little remanent magnetisation, of the order of $100\,\mathrm{A\,m^{-1}}$ as measured in Fig. 4.2 (a). This is small compared to the magnetisation induced by the external field, which is one or two orders of magnitude larger. However, this anisotropy in the magnetic properties of the material is enough to lead to a reorientation of the particle in a variable external field.

Evidence of this individual rotation can be found by tracing a mark on a particle with a marker pen. By correlation, we can then calculate the angle θ of the bead at any time. If we consider that we are in the Stokes regime, then the magnetic torque

$$\tau_m = |\vec{m} \times \vec{B}|, \tag{7.2}$$

where $\vec{m}$ is the magnetic moment of the particle, must be equal at all times with the viscous torque, which for a fully immersed sphere rotating at a constant speed Ω reads

$$\tau_\eta = 8\pi\eta R^3\Omega. \tag{7.3}$$

We can therefore expect a direct proportionality between τ_m and Ω.

In Fig. 7.7, a single sphere is submitted to a horizontal constant field B_x that changes sign abruptly, leading the particle to rotate a half turn. The maximal rotation speed $\Omega_{\max}$ is measured for several values of B_x. Two possible evolutions of $\Omega_{\max}$ with B_x can be expected. If the magnetic moment $\vec{m}$ responsible for the rotation is permanent and of magnitude m_{perm}, we have

$$\Omega_{\max} \propto \tau_{m,\,\max} = m_{\mathrm{perm}} B_x \propto B_x. \tag{7.4}$$

On the other hand, if the moment responsible is an induced moment of magnitude $m_{\mathrm{ind}} = \chi V B_x/\mu_0$, then we have

$$\Omega_{\max} \propto \tau_{m,\,\max} = m_{\mathrm{ind}} B_x \propto B_x^2. \tag{7.5}$$

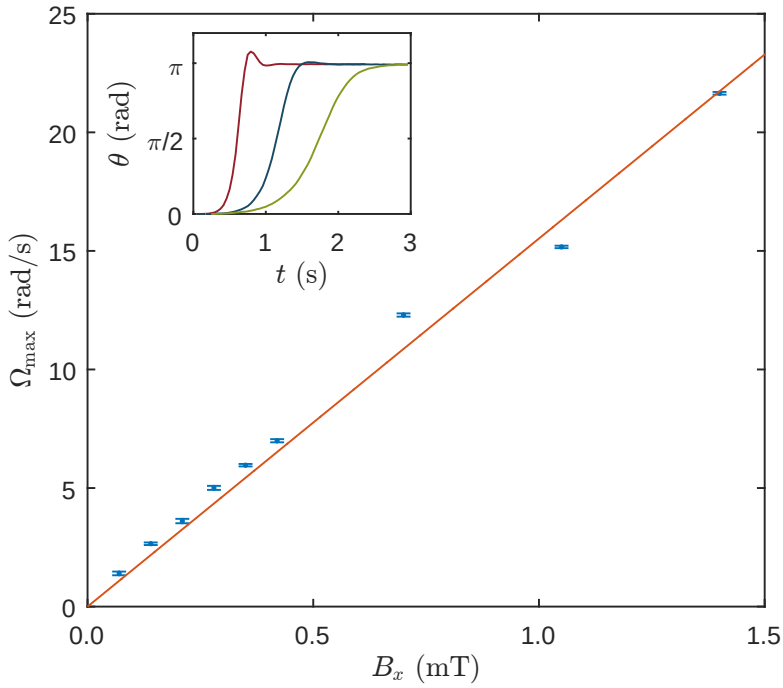

Fig. 7.7 Single particle. – Maximal rotation speed $\Omega_{\max}$ of a single particle, as a function of the amplitude of a horizontal field B_x that changes sign at $t = 0$. The inset shows the angle θ as a function of time for three values of B_x.

As can be seen in Fig. 7.7, the evolution of $\Omega_{\max}$ with regards to B_x is linear, suggesting that the rotation of the individual particles is indeed an effect of a small remanent magnetisation. One possible explanation comes from the fact that the spheres are formed by cutting steel wire into small cylinders, which are then pressed into rough spheres and finally rounded. The process of pressing the cylinders into a die might create some anisotropy in the spheres, which could be at the origin the permanent component of the magnetisation. The inset of Fig. 7.7 shows the angle θ as a function of time during the inversion. One can see that a stronger field leads to a faster rotation. For higher values of B_x, there is a slight overshoot due to inertia. This is not surprising considering that, in order to facilitate

the measurement, a larger particle of 1 mm in diameter was used. It was observed that the axis of rotation is always perpendicular to the interface. Out-of-plane rotations might be prevented due to the additional energy cost required to move the contact line.

7.2.2 Dipole-Dipole Alignment

Secondly, the whole structure can reorient in an external field due to the pairwise magnetic dipolar interactions between particles. Let us consider only induced magnetic dipoles, which are always aligned with the external field. From 3.3, the potential energy associated with the horizontal field for a pair of particles can be written

$$U_{m,x}^{\text{pair}} = \frac{\mu_0 m^2}{4\pi d^3}\left(1-3\cos^2\phi\right) = U_0\left(1-3\cos^2\phi\right) \tag{7.6}$$

where U_0 corresponds to the maximum energy for a given d, reached when the pair is oriented perpendicular to the field. The minimum of energy is reached when the pair is aligned with the field and is equal to $-2\,U_0$. This means that under a horizontal field B_x, a pair of particles will experience a torque and tend to align with the field. Let us now consider the case of three particles. For simplicity and because this situation is prevalent in the experiment [28, 78], we will suppose that the particles lay on the vertices of an isosceles triangle. Let α denote the vertex angle of the isosceles, L the length of its legs and ϕ the angle between its base and the external field. Summing the pairwise energy contributions leads to

$$U_{m,x}^{\text{iso}} = U_0\left(3\cos\alpha\cos 2\phi - 1 + \frac{1-3\cos^2\phi}{8\sin^3\frac{\alpha}{2}}\right). \tag{7.7}$$

For two values of α between 0 and π, this expression is independent on ϕ, meaning that all the orientations of the assembly with regard to the field are energetically equivalent. These values are $\alpha = \pi/3$, corresponding to

an equilateral triangle, and $\alpha \approx 1.2605$, which is the value of α such that $\cos\alpha \sin^3(\alpha/2) = 1/16$. In fact, by symmetry, the independence of the total magnetic interaction energy on the orientation of B_x is verified for any regular polygon, with or without a central particle. This means that, for low values of B_x, the dynamics will be driven by the individual rotation of the particles for which the torque is proportional to B_x. On the other hand, we can expect the dipole-dipole interaction, quadratic in B_x, to play a role at high amplitudes, for which the deformation of the triangle is significant.

7.2.3 Deformations

As can be seen from Eq. (7.7), most magnetocapillary self-assemblies have a preferred orientation with the horizontal field only when deformed. However, both this effect and the effect of the individual rotations of the particles should become inefficient at high frequencies, as the dipoles struggle to follow the external field. For instance, equating the magnetic torque from Eq. (7.2) to the viscous torque from Eq. (7.3) and neglecting inertia, we find

$$\sin\theta = \frac{8\pi\eta R^3}{mB_x}\dot{\theta} = \tau\dot{\theta} \tag{7.8}$$

who has a solution of the type

$$\theta = 2\cot^{-1}\left(e^{-t/\tau+C_0}\right) \tag{7.9}$$

where C_0 is an integration constant. This means that there is a typical reaction time τ needed for a dipole to align with an external field. In fact, looking at Eq. (7.9), we can see that it takes about 5τ to cover 95 % of the half-turn. We can therefore define a typical cut-off frequency

$$f_{\text{cut}} = \frac{1}{\tau} = \frac{mB_x}{8\pi\eta R^3}. \tag{7.10}$$

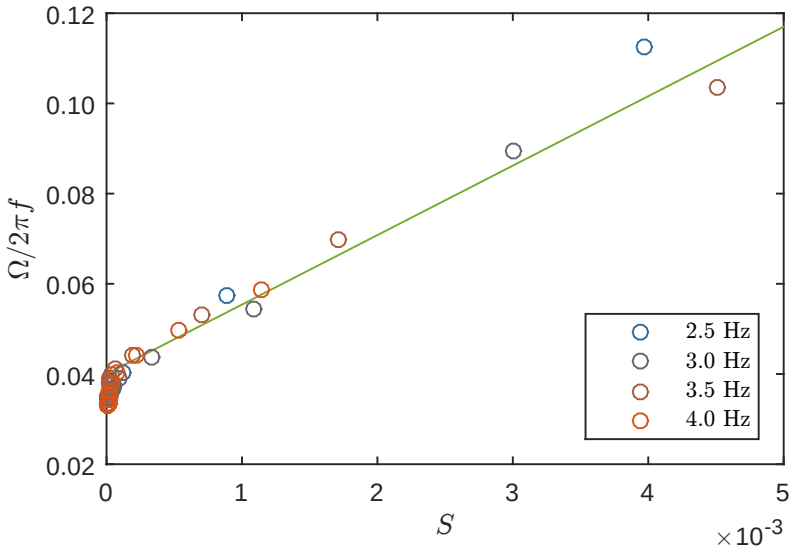

Fig. 7.8 Surface of the cycles. – The rotational speed from Fig. 7.6 is shown as a function of the surface of the cycles in the (d,θ) plane. The straight line in green is a guide for the eye.

which is equal to 10 Hz for a field of about 0.6 mT. This would mean that there is an observable decrease in the oscillation amplitude as early as 2 Hz. Dipole-dipole interactions are usually weaker than dipole-field interactions in magnetocapillary assemblies, as the field generated from a particle is given by $\mu_0 m/4\pi d^3$, which for an induced dipole is smaller than the external field by a factor $R^3/d^3 \approx 1/64$ for particles at a typical distance $2D$. This means that we can expect an even more drastic cut-off in the case of the dipole-dipole alignment. This is consistent with the extremely low excitation frequency needed to observe a rotation of the whole assembly locked with the external field, as shown in Fig. 7.3.

This means that both previously discussed mechanisms cannot explain the sudden increase in rotational speed at combined high frequency and high amplitude described in Figs. 7.5 and 7.6. As deformations are high in this regime, one could wonder if an angular equivalent of Eq. (5.1) might

exist. In other words, the non-reciprocal cycles shown in Fig. 7.5 could power the rotational motion, similarly to the translational motion of the Najafi-Golestanian swimmer. Let us assume that each particle, represented by its polar coordinates d_i/D and θ_i, oscillates harmonically both radially and angularly at a frequency f. We denote the corresponding dimensionless amplitudes $A_{d,i}$ and $A_{\theta,i}$ and the phase between both signals ϕ_i. By analogy with Eq. (5.1), we construct the ansatz of an expression for the rotational speed

$$\Omega \propto \sum_{i=1}^{N} 2\pi f A_{d,i} A_{\theta,i} \sin\left(\phi_i\right) \tag{7.11}$$

where we considered each particle to act as an independent motor whose contributions can be summed. As the trajectories in the (d,θ) plane are not necessarily ellipses, we can assume a more general expression

$$\Omega \propto \sum_{i=1}^{N} 2\pi f S_i = 2\pi f S \tag{7.12}$$

where S_i is the dimensionless surface enclosed by the trajectory of particle i. Indeed, as demonstrated in Appendix B, the expressions from Eq. (7.11) and Eq. (7.12) are equivalent in the case of an ellipse. Figure 7.8 compares the rotational speed and the dimensionless surface of the cycles for the data of Fig. 7.6. Most of the points are concentrated around $\Omega/2\pi f \approx 0.04$ and $S \approx 0$, corresponding to the plateau in Fig. 7.6, where deformations are small and the rotation is explained by the two previously discussed mechanisms. However, for fast rotations $\Omega/2\pi f > 0.04$ we see a linear relationship between the combined dimensionless area S and the dimensionless rotational speed $\Omega/2\pi f$, confirming our hypothesis that these fast rotations are powered by non-reciprocal deformations.

7.3 Summary

To conclude, rotating fields cause magnetocapillary assemblies to rotate thanks to three distinct mechanisms. First, individual particles rotate, similarly to a compass needle in a magnetic induction field. This effect can be attributed to a permanent component in the magnetisation of the spheres, probably linked to their fabrication process. Secondly, dipole-dipole interactions can contribute to a reorientation. This effect is expected to dominate at vanishing excitation frequency, where the rotation of the assembly is locked with the external field. Furthermore, dipoles on a regular polygon have no reason to rotate as their interaction energy is independent on the orientation with regards to the field. This means that this effect requires a deformation of the assembly. Under high frequency and high amplitude, a very fast rotation is observed that cannot be explained by the previous two mechanisms. A linear relationship between the rotation speed and the area of the deformation cycles has been evidenced. This demonstrates that non-reciprocal deformations are the key mechanism behind this regime characterised by high deformations, similarly to the swimming modes discussed in previous chapters.

8 Conclusion and Perspectives

8.1 Hindsight

In this work, the statics and dynamics of magnetocapillary self-assemblies were studied experimentally and theoretically. When soft-ferromagnetic particles floating on water are submitted to magnetic induction fields, a wide variety of configurations can be observed depending on the number of particles and the orientation and strength of the field. After reviewing the properties of interfacial swimmers, we presented the general framework of magnetocapillary self-assemblies under static fields. From the relevant forces and dimensionless numbers, we can extract information on the equilibrium distances, on the parameters that will cause the particles to irreversibly collide and the multiple geometries that can be attained. The remaining chapters of this thesis focused on low-particle count under time-dependent field, which allows to improve our fundamental understanding of these systems and corresponds to the ideal case to generate locomotion.

First, we studied the vibrational dynamics of a pair of particles. This dimer is the fundamental building block for magnetocapillary systems. Two eigenmodes have been identified, each behaving like a forced, damped harmonic oscillator with distinct spring constants and natural frequencies. One is radial and due to a preferred distance between the particles, and

the other is angular and due to a preferred orientation with the imposed horizontal field.

These simple building blocks can be assembled to form magnetocapillary swimmers moving along the interface. A minimum of three particles is necessary to produce the required breaking of symmetry. The simplest triplet uses particles in a collinear configuration. The outer spheres differ in size, which causes a phase shift between their oscillations. The resulting stroke resembles the kinematic swimmer theorised by Najafi and Golestanian [23]. This one-dimensional model has produced plenty of theoretical results that can now be analysed experimentally.

A second, faster swimmer can be made using three particles in a triangular configuration. The combined deformation and rotation of this assembly causes a net motion in a straight line. It is possible to steer this swimmer by changing the direction of the oscillating field, allowing for a rather precise control of the trajectories. These swimmers can be made to perform some simple tasks such as the capture, transport and release of a cargo and the mixing of fluids.

As rotational motions are key to both locomotion and potential mixing applications of this swimmer, the last chapter of this thesis presents a study of the rotational modes of triangular assemblies. Several ingredients have been identified that can each cause the assembly to rotate. A magnetic anisotropy in the particles could explain that the individual particles follow the external field like a compass needle. The assembly can also reorient because of dipole-dipole interactions, an effect that by symmetry is non-existent on a regular polygon. Finally, a regime where non-reciprocal deformations power the rotation of the assembly similarly to translational swimmers has been evidenced.

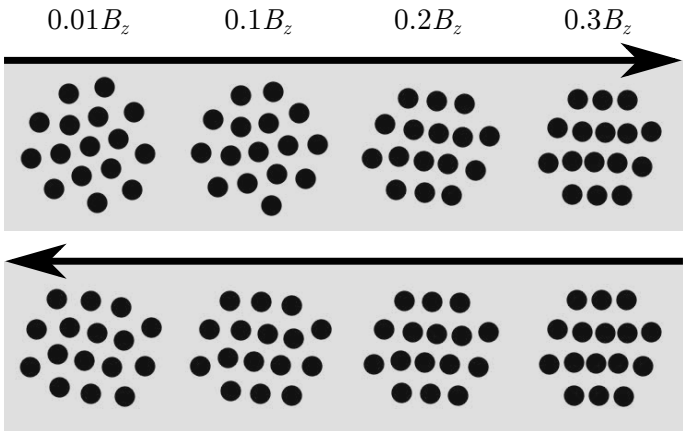

Fig. 8.1 Rearrangement in a large assembly. – A quasistatic variation of B_x/B_z evidences some rearrangements in a 16-particle assembly. The positions are obtained by a Monte-Carlo simulation. The particles tend to form lines in the direction of the field. When the field is decreased, hysteresis is observed as the particles stay in the rearranged configuration.

8.2 Foresight

8.2.1 Large Assemblies

Several questions remain unanswered in magnetocapillary systems. Most notably, this thesis focused mostly on low particle count. However, larger assemblies might be useful in some situations, such as the transport of bigger cargoes. Furthermore, large structures might possess many equilibrium positions and experience some rearrangements under time-dependent fields. For instance, in Fig. 8.1, 16 particles are submitted to a quasistatic increase, then decrease of B_x in a Monte-Carlo simulation. The particles tend to rearrange to form lines in the direction of B_x, minimising their interaction energy. When the field is decreased back to $B_x/B_z \approx 0$, the particles stay in the newly obtained configuration. This kind of reorganisation and hysteresis, as well as the coexistence of several states stable even in the absence of a horizontal field, are also observed in the experiment.

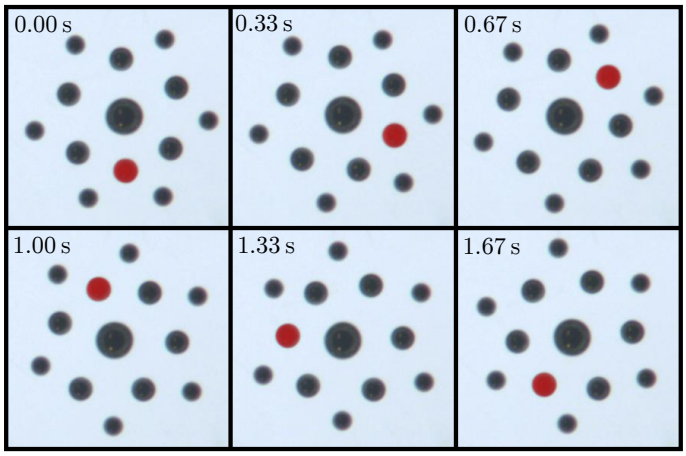

Fig. 8.2 Large polydisperse assembly rotating. – A large assembly composed of one 793 µm, six 500 µm and six 397 µm spheres is submitted to a horizontal field rotating at 2 Hz. A wave of perturbation follows the field, as evidenced by highlighting in red the bead closest to the central one at a given time.

Due to the exponentially larger number of degrees of freedom, it might be more efficient to describe the deformations of larger assemblies in terms of waves of perturbations. Indeed, as shown in Fig. 7.5 in the case of three particles submitted to a rotating field, the complex motion of the assembly can sometimes be understood as succession of out-of-phase, but otherwise similar oscillations. This kind of approach would greatly simplify the study of the deformations of large assemblies. As an example, Fig. 8.2 shows a flower-like assembly composed of 13 particles. A larger central particle of 793 µm can confine many smaller particles on its periphery due a stronger Cheerios effect. Here, six 500 µm and six 397 µm particles are placed in a staggered pattern. While this highly symmetric structure is not the only possible one obtainable with these particles, large spheres tend to move to the centre of these assemblies due to gravity.

When such a structure is submitted to a rotating field, a rotating wave of perturbation appears that follows the field. This causes the assembly to rotate at an angular speed smaller than that of the field. The field rotates

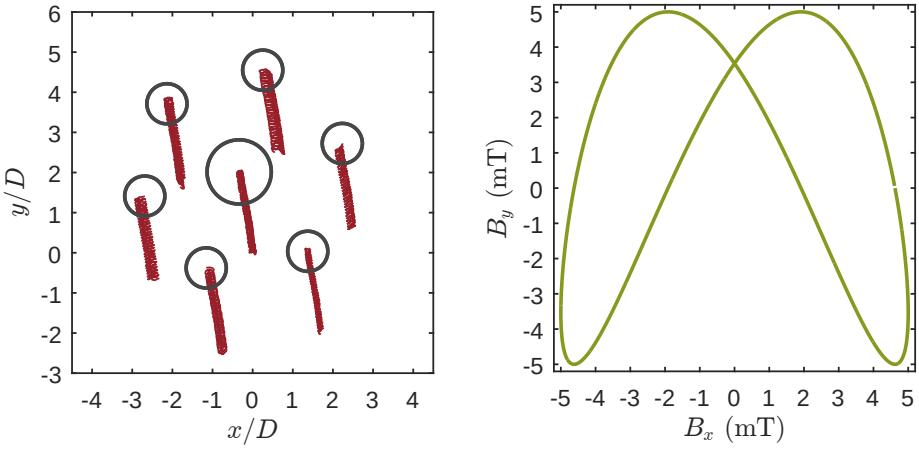

Fig. 8.3 Large assembly swimming. – On the left, trajectory of a seven-particle assembly over 20 periods of the external field, with six particles of diameter $D = 500\,\mu\text{m}$ and a central particle of 793 µm. On the right, the magnetic field used. It follows Eq. (8.1) with the parameters $B_x = 5\,\text{mT}$, $\omega/2\pi = 1.5\,\text{Hz}$ and $\delta = \pi/8$.

with a period of 2 s, over which the assembly has rotated by about 25°. One can see that the peripheral beads successively get closer to the central one, following the direction of the horizontal field. The intermediate-sized bead in the direction of the field is coloured red for emphasis. One could wonder why the wave of deformation is only observed in the direction of the field, and not in the direction opposite, as the dipole-dipole interaction is a function of B_x^2 and should therefore be symmetrical. This can be understood by picturing the three-dimensional disposition of the particles. The centre of the inner sphere is much lower than the centres of the peripheral particles, due to both its larger size and the curvature of the interface caused by the combined weight of the assembly. The angle between dipoles is therefore different whether the field is in the direction of the particle, or in the direction opposite.

This asymmetry is important, because it means one could generate waves independently on each side of the assembly. Starting from Eq. (7.1),

we can double the frequency along the y-axis to obtain

$$\vec{B}_{\text{wave}} = B_x \left(\cos(\omega t + \delta)\, \vec{e}_x + \sin(2\omega t)\, \vec{e}_y \right). \tag{8.1}$$

This is a Lissajous curve of ratio 1 : 2. A phase shift δ might be used to break the mirror symmetry about the x-axis. Figure 8.3 shows one such curve applied to a large assembly. Each lobe of the Lissajous curve generates a wave on each side of the assembly. Both waves move towards the same direction. A net motion is observed in the direction opposite to the waves at about 0.1 D/T. This approach is similar to the swimming mechanisms of ciliates, bacteria that swim by propagating waves through arrays of hair-like organelles called cilia. The swimming strategy of ciliates is often approximated by a spherical body, called a squirmer, with an axisymmetric slip velocity on its surface caused by the wave of beating cilia [152, 153]. In more refined models, the complex motion of a single cilium is sometimes modelled by solid spheres moving on elliptical trajectories [154, 155]. The motion from Fig. 8.3 could therefore be seen as a two-dimensional analogue to ciliary propulsion. Further studies should aim at optimising the various waveform parameters and the geometry of the assembly for speed, as well as analyse the complex waves propagating through the assembly to discuss the resemblance with ciliates.

8.2.2 Complex Interfaces

As discussed in Sections 3.1.2 and 5.3, the lower bound on the particle sizes usable for magnetocapillary assemblies is given by the capillary attraction. As the deformation of the interface producing the Cheerios effect is powered by the weight of the spheres, we can expect it to vanish for truly micrometric particles. Comparing the Cheerios effect with thermal agitation, we find a diameter of 3.4 µm below which this attractive force is ineffective and a magnetocapillary dimer would not form. One could slightly lower

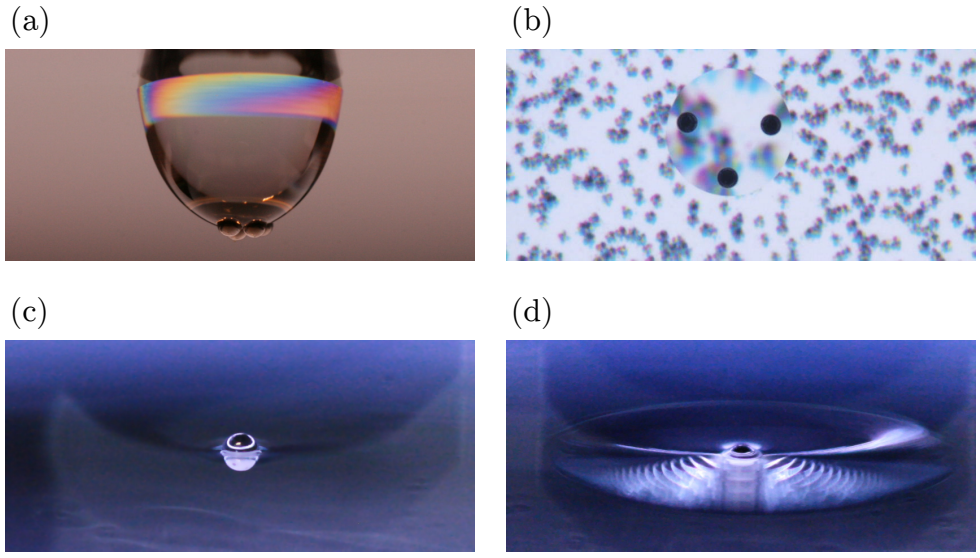

Fig. 8.4 Various complex geometries. – **(a) Pending droplet.** A drop of water containing 4 particles is deposited on a substrate that is then flipped. **(b) Oil lens.** A drop of paraffin oil forms a liquid lens when placed on water. Particles can get trapped at different locations. A random pattern is placed below the water to visualise the lens. **(c) Soap film.** A single particle has been placed on a soap film. **(d) Soap film with added water.** The same particle after the addition of water. The intricate reflections are a consequence of the complex curvature of the interface.

this bound by increasing the density of the particles or adding a body force other than gravity, such as from a vertical magnetic gradient. However, geometry can also play an important role in the Cheerios effect [99–101]. For instance, particles on a curved surface can feel an extra confinement. Particles embedded in a thin film can be surrounded by a meniscus, causing a Cheerios effect that is not dependent on gravity. In fact, this effect is known to cause macromolecules embedded in a biological membrane to interact at the nanoscale [99].

In Fig. 8.4, we present several preliminary experiments where 500 µm particles were placed in geometries more complex than a flat surface. First, particles in a pending droplet experience an additional confinement, caus-

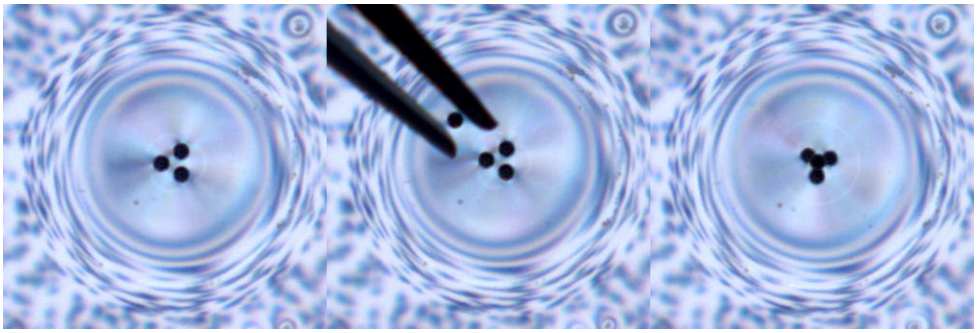

Fig. 8.5 Assembly of a tetrahedron. – Three spheres are trapped below a soap film locally thickened by the addition of water. When a fourth particle is dropped, it stays on the upper surface and forms a tetrahedron with the other three.

ing them to sediment at the bottom (Fig. 8.4 (a)). While similar to the Cheerios effect, this force is driven by the resultant weight of a single particle and therefore proportional to its volume, or D^3, as opposed to the pairwise interaction that is proportional to q^2 and therefore D^6 [156, 157].

Secondly, particles can be embedded in a thin soap film (Fig. 8.4 (c)). This means that the presence of a disjoining pressure Π must be taken into account in the Young-Laplace equation [97]. Another way to express this is to define a modified capillary length

$$l_c^* = \sqrt{\frac{\gamma}{\rho g - \Pi'}} \tag{8.2}$$

where Π' is the derivative of the disjoining pressure with respect to the thickness of the film [158]. This geometry also changes the expression of the capillary charge, leading to a much slower decrease of the capillary interaction force with size, namely $F \propto D^2$ as opposed to $F \propto D^6$, leading to an observable Cheerios effect at the nanoscale [97, 99, 159].

Finally, it is possible to combine these effects in even more exotic configurations. A thin soap film can be locally thickened by the addition of liquid, creating a relatively well-defined pending droplet (Fig. 8.4 (d)). Par-

ticles can be trapped at the liquid-air interfaces below or above the drop, or both if the particle is large enough compared to the drop's thickness. Some fluids, such as paraffin oil, form liquid lenses when deposited on water (Fig. 8.4 (b)). Particles can similarly get trapped at multiple locations, above, below or through the lens, with the added possibility of a particle laying at the triple line, on the edge of the lens.

These complex interfaces open up many new possibilities for magnetocapillary microswimmers. Not only could they allow produce self-assemblies at the submicrometer scale, but they offer a way to generate three-dimensional structures. Figure 8.5 shows the formation of a multi-level assembly. A regular triangle floats below a soap film previously thickened by adding a drop of water with a micropipette. A fourth particle is dropped on the film and drifts towards the centre, forming a tetrahedron with the three particles below. These types of multi-level arrangements could be a first step towards three-dimensional structures and assemblies in the bulk. This would first necessitate to improve our understanding of the Cheerios effect in these complex geometries through a systematic experimental and theoretical study. Taking inspiration from liquid marbles and colloidal capsules [160–164], it might be possible to generate self-assemblies on microdoplets and emulsions, creating a new generation of magnetocapillary swimmers able to move freely in the bulk, greatly expanding their scope and depth.

List of Publications

- G. Grosjean, G. Lagubeau, A. Darras, M. Hubert, G. Lumay, N. Vandewalle, *Remote control of self-assembled microswimmers*, Sci. Rep. **5**, 16035 (2015)
- G. Lagubeau, G. Grosjean, A. Darras, G. Lumay, M. Hubert, N. Vandewalle, *Statics and dynamics of magnetocapillary bonds*, Phys. Rev. E **93**, 053117 (2016)
- G. Grosjean, M. Hubert, G. Lagubeau, N. Vandewalle, *Realization of the Najafi-Golestanian microswimmer*, Phys. Rev. E **94**, 021101 (2016)
- M. Poty, F. Weyer, G. Grosjean, G. Lumay, N. Vandewalle, *Magnetoelastic instability in soft thin films*, Eur. Phys. J. E **40**, 29 (2017)
- G. Grosjean, M. Hubert, N. Vandewalle, *Magnetocapillary self-assemblies: Locomotion and micromanipulation along a liquid interface*, Adv. Colloid Interface Sci. **255**, 84 (2018)
- G. Grosjean, M. Hubert, Y. Collard, S. Pillitteri, N. Vandewalle, *Surface swimmers, harnessing the interface to self-propel*, Eur. Phys. J. E (in press)
- G. Grosjean, Y. Collard, M. Hubert, A. Sukhov, J. Harting, A.S. Smith, N. Vandewalle, *Capillary assemblies in a rotating magnetic field*, in preparation (2018)

REFERENCES

[1] R.F. Bruinsma, W.M. Gelbart, D. Reguera, J. Rudnick, R. Zandi, Phys. Rev. Lett. **90**, 248101 (2003)

[2] J.D. Perlmutter, C. Qiao, M.F. Hagan, Elife **2**, e00632 (2013)

[3] A. Railliet, *Traité de zoologie médicale agricole* (Asselin et Houzeau, 1895)

[4] E.M. Purcell, Am. J. Phys. **45**, 3 (1977)

[5] M. Khursheed, *Ramzan Ahmed, 70, stitches a soccer ball at a factory in Sialkot* (2011), Reuters

[6] G.M. Whitesides, B. Grzybowski, Science **295**, 2418 (2002)

[7] D. Vella, L. Mahadevan, Am. J. Phys. **73**, 817 (2005)

[8] N. Vandewalle, L. Clermont, D. Terwagne, S. Dorbolo, E. Mersch, G. Lumay, Phys. Rev. E **85**, 041402 (2012)

[9] N. Vandewalle, N. Obara, G. Lumay, Eur. Phys. J. E **36**, 1 (2013)

[10] G. Lumay, N. Obara, F. Weyer, N. Vandewalle, Soft Matter **9**, 2420 (2013)

[11] G. Grosjean, M. Hubert, Y. Collard, S. Pillitteri, N. Vandewalle, Eur. Phys. J. E (in press)

[12] G.I. Taylor, Proc. R. Soc. Lond. A **209**, 447 (1951)

[13] E. Lauga, T.R. Powers, Rep. Prog. Phys. **72**, 096601 (2009)

[14] C. Navier, Mem. Acad. R. Sci. France **6**, 389 (1823)

[15] G.G. Stokes, Trans. Cambridge Philos. Soc. **8**, 287 (1845)

[16] G.G. Stokes, Trans. Cambridge Philos. Soc. **9**, 8 (1851)

[17] O. Reynolds, Philos. Trans. R. Soc. **174**, 935 (1884)

[18] D. Klotsa, K.A. Baldwin, R.J.A. Hill, R.M. Bowley, M.R. Swift, Phys. Rev. Lett. **115**, 248102 (2015)

[19] S. Alben, M. Shelley, Proc. Natl. Acad. Sci. U.S.A. **102**, 11163 (2005)

[20] E. Lauga, Phys. Fluids **19**, 061703 (2007)

[21] R. Trouilloud, S.Y. Tony, A. Hosoi, E. Lauga, Phys. Rev. Lett. **101**, 048102 (2008)

[22] D.O. Pushkin, J.M. Yeomans, Phys. Rev. Lett. **111**, 188101 (2013)

[23] A. Najafi, R. Golestanian, Phys. Rev. E **69**, 062901 (2004)

[24] R. Dreyfus, J. Baudry, M.L. Roper, M. Fermigier, H.A. Stone, J. Bibette, Nature **437**, 862 (2005)

[25] P. Tierno, R. Golestanian, I. Pagonabarraga, F. Sagués, J. Phys. Chem. B **112**, 16525 (2008)

[26] F. Martinez-Pedrero, P. Tierno, Phys. Rev. Applied **3**, 051003 (2015)

[27] P. Tierno, R. Golestanian, I. Pagonabarraga, F. Sagués, Phys. Rev. Lett. **101**, 218304 (2008)

[28] G. Grosjean, G. Lagubeau, A. Darras, M. Hubert, G. Lumay, N. Vandewalle, Sci. Rep. **5**, 16035 (2015)

[29] A. Farutin, S. Rafaï, D.K. Dysthe, A. Duperray, P. Peyla, C. Misbah, Phys. Rev. Lett. **111**, 228102 (2013)

[30] R. Golestanian, A. Ajdari, Phys. Rev. E **77**, 036308 (2008)

[31] R. Zargar, A. Najafi, M. Miri, Phys. Rev. E **80**, 026308 (2009)

[32] K. Pickl, J. Götz, K. Iglberger, J. Pande, K. Mecke, A.S. Smith, U. Rüde, J. Comput. Sci. **3**, 374 (2012)

[33] J. Pande, A.S. Smith, Soft Matter **11**, 2364 (2015)

[34] J. Pande, L. Merchant, T. Krüger, J. Harting, A.S. Smith, New J. Phys. **19**, 053024 (2017)

[35] E. Lauga, EPL **86**, 64001 (2009)

[36] T. Qiu, T.C. Lee, A.G. Mark, K.I. Morozov, R. Münster, O. Mierka, S. Turek, A.M. Leshansky, P. Fischer, Nat. Commun. **5** (2014)

[37] E. Lauga, D. Bartolo, Phys. Rev. E **78**, 030901 (2008)

[38] P. Tierno, O. Güell, F. Sagués, R. Golestanian, I. Pagonabarraga, Phys. Rev. E **81**, 011402 (2010)

[39] S. Nakata, M. Hata, Y.S. Ikura, E. Heisler, A. Awazu, H. Kitahata, H. Nishimori, J. Phys. Chem. C **117**, 24490 (2013)

[40] N. Bassik, B.T. Abebe, D.H. Gracias, Langmuir **24**, 12158 (2008)

[41] E. Bormashenko, Y. Bormashenko, R. Grynyov, H. Aharoni, G. Whyman, B.P. Binks, J. Phys. Chem. C **119**, 9910 (2015)

[42] D. Okawa, S.J. Pastine, A. Zettl, J.M. Fréchet, J. Am. Chem. Soc. **131**, 5396 (2009)

[43] H. Ebata, M. Sano, Sci. Rep. **5** (2015)

[44] A. Snezhko, I.S. Aranson, W.K. Kwok, Phys. Rev. E **73**, 041306 (2006)

[45] A. Snezhko, I.S. Aranson, Nat. mater. **10**, 698 (2011)

[46] R. Golestanian, T.B. Liverpool, A. Ajdari, New J. Phys. **9**, 126 (2007)

[47] J.R. Howse, R.A.L. Jones, A.J. Ryan, T. Gough, R. Vafabakhsh, R. Golestanian, Phys. Rev. Lett. **99**, 048102 (2007)

[48] M.N. Popescu, W.E. Uspal, S. Dietrich, Eur. Phys. J. Spec. Top. **225**, 2189 (2016)

[49] S. Michelin, E. Lauga, D. Bartolo, Phys. Fluids **25**, 061701 (2013)

[50] H.R. Jiang, N. Yoshinaga, M. Sano, Phys. Rev. Lett. **105**, 268302 (2010)

[51] M. Pumera, Nanoscale **2**, 1643 (2010)

[52] X. Wang, M. In, C. Blanc, M. Nobili, A. Stocco, Soft Matter **11**, 7376 (2015)

[53] X. Wang, M. In, C. Blanc, A. Würger, M. Nobili, A. Stocco, Langmuir **33**, 13766 (2017)

[54] K. Dietrich, D. Renggli, M. Zanini, G. Volpe, I. Buttinoni, L. Isa, New J. Phys. **19**, 065008 (2017)

[55] K. Dietrich, G. Volpe, M.N. Sulaiman, D. Renggli, I. Buttinoni, L. Isa, Phys. Rev. Lett. **120**, 268004 (2018)

[56] P. Malgaretti, M. Popescu, S. Dietrich, Soft matter **14**, 1375 (2018)

[57] A. Domínguez, P. Malgaretti, M. Popescu, S. Dietrich, Soft matter **12**, 8398 (2016)

[58] A. Domínguez, P. Malgaretti, M.N. Popescu, S. Dietrich, Phys. Rev. Lett. **116**, 078301 (2016)

[59] Y. Karasawa, S. Oshima, T. Nomoto, T. Toyota, M. Fujinami, Chem. Lett. **43**, 1002 (2014)

[60] T. Mitsumata, J.P. Gong, Y. Osada, Polymer. Adv. Tech. **12**, 136 (2001)

[61] S. Nakata, S. ichi Hiromatsu, Chem. Phys. Lett. **405**, 39 (2005)

[62] Z. Izri, M.N. Van Der Linden, S. Michelin, O. Dauchot, Phys. Rev. Lett. **113**, 248302 (2014)

[63] R.T. Mallea, A. Bolopion, J.C. Beugnot, P. Lambert, M. Gauthier, IEEE/ASME Trans. Mechatronics **22**, 693 (2017)

[64] A.S. Basu, S.Y. Yee, Y.B. Gianchandani, *Virtual components for droplet control using marangoni flows: size-selective filters, traps, channels, and pumps*, in *2007 IEEE 20th International Conference on Micro Electro Mechanical Systems (MEMS)* (IEEE, 2007), pp. 401–404

[65] Y. Couder, S. Protiere, E. Fort, A. Boudaoud, Nature **437**, 208 (2005)

[66] O.S. Pak, E. Lauga, J. Eng. Math. **88**, 1 (2014)

[67] D.L. Hu, B. Chan, J.W. Bush, Nature **424**, 663 (2003)

[68] D.L. Hu, J.W. Bush, Nature **437**, 733 (2005)

[69] S. Gart, D. Vella, S. Jung, Soft Matter **7**, 2444 (2011)

[70] R. Suter, O. Rosenberg, S. Loeb, H. Wildman, J. Long, J. Exp. Biol. **200**, 2523 (1997)

[71] X.Q. Feng, X. Gao, Z. Wu, L. Jiang, Q.S. Zheng, Langmuir **23**, 4892 (2007)

[72] J.W. Bush, D.L. Hu, M. Prakash, Adv. In Insect Phys. **34**, 117 (2007)

[73] Y.S. Song, M. Sitti, IEEE Trans. Robot **23**, 578 (2007)

[74] X. Zhang, J. Zhao, Q. Zhu, N. Chen, M. Zhang, Q. Pan, ACS Appl. Mater. Interfaces **3**, 2630 (2011)

[75] G.K. Batchelor, *An introduction to fluid dynamics* (Cambridge university press, 2000)

[76] G.K. Taylor, R.L. Nudds, A.L. Thomas, Nature **425**, 707 (2003)

[77] C. Eloy, J. Fluids Struct. **30**, 205 (2012)

[78] G. Grosjean, M. Hubert, N. Vandewalle, Adv. Colloid Interface Sci. **255**, 84 (2018)

[79] G. Whitesides, J. Mathias, C. Seto, Science **254**, 1312 (1991)

[80] W. Han, Z. Lin, Angew. Chem. **51**, 1534 (2012)

[81] A. Klug, Philos. Trans. Royal Soc. B **354**, 531 (1999)

[82] G.M. Whitesides, M. Boncheva, Proc. Natl. Acad. Sci. USA **99**, 4769 (2002)

[83] J. Zhang, Z. Sun, B. Yang, Curr. Opin. Colloid Interface Sci. **14**, 103 (2009)

[84] K. Thorkelsson, P. Bai, T. Xu, Nano Today **10**, 48 (2015)

[85] M.A. Boles, M. Engel, D.V. Talapin, Chem. Rev. **116**, 11220 (2016)

[86] Y. Dou, B. Wang, M. Jin, Y. Yu, G. Zhou, L. Shui, J. Micromechanics Microengineering **27**, 113002 (2017)

[87] A. Rida, M.A.M. Gijs, Anal. Chem. **76**, 6239 (2004)

[88] F.S. Majedi, M.M. Hasani-Sadrabadi, S. Hojjati Emami, M.A. Shokrgozar, J.J. VanDersarl, E. Dashtimoghadam, A. Bertsch, P. Renaud, Lab Chip **13**, 204 (2013)

[89] L.Y. Wu, D. Di Carlo, L.P. Lee, Biomed. Microdevices **10**, 197 (2008)

[90] S.E. Chung, W. Park, S. Shin, S.A. Lee, S. Kwon, Nature mater. **7**, 581 (2008)

[91] L. Baraban, M. Tasinkevych, M.N. Popescu, S. Sanchez, S. Dietrich, O.G. Schmidt, Soft Matter **8**, 48 (2012)

[92] S.H. Kim, S.Y. Lee, S.M. Yang, G.R. Yi, NPG Asia Mater. **3**, 25 (2011)

[93] J.B. Edel, A.A. Kornyshev, M. Urbakh, ACS Nano **7**, 9526 (2013)

[94] M. Golosovsky, Y. Saado, D. Davidov, Appl. Phys. Lett. **75**, 4168 (1999)

[95] W. Wen, L. Zhang, P. Sheng, Phys. Rev. Lett. **85**, 5464 (2000)

[96] M. Golosovsky, Y. Saado, D. Davidov, Phys. Rev. E **65**, 061405 (2002)

[97] P.A. Kralchevsky, K. Nagayama, Langmuir **10**, 23 (1994)

[98] M.M. Nicolson, Math. Proc. Cambridge Philos. Soc. **45**, 288 (1949)

[99] P.A. Kralchevsky, K. Nagayama, Adv. Colloid Interface Sci. **85**, 145 (2000)

[100] K.D. Danov, P.A. Kralchevsky, Adv. Colloid Interface Sci. **154**, 91 (2010)

[101] M. Poty, G. Lumay, N. Vandewalle, New J. Phys. **16**, 023013 (2014)

[102] G. Lagubeau, G. Grosjean, A. Darras, G. Lumay, M. Hubert, N. Vandewalle, Phys. Rev. E **93**, 053117 (2016)

[103] J.A. Osborn, Phys. Rev. **67**, 351 (1945)

[104] B.A. Grzybowski, H.A. Stone, G.M. Whitesides, Nature **405**, 1033 (2000)

[105] R. Messina, S. Aljawhari, L. Bécu, J. Schockmel, G. Lumay, N. Vandewalle, Sci. Rep. **5**, 10348 (2015)

[106] D. Vella, Annu. Rev. Fluid Mech. **47**, 115 (2015)

[107] D. Ershov, J. Sprakel, J. Appel, M.A.C. Stuart, J. van der Gucht, Proc. Natl. Acad. Sci. USA **110**, 9220 (2013)

[108] R. Chinomona, J. Lajeunesse, W.H. Mitchell, Y. Yao, S.E. Spagnolie, Soft Matter **11**, 1828 (2015)

[109] A. Domínguez, M. Oettel, S. Dietrich, Phys. Rev. E **82**, 011402 (2010)

[110] D.G. Lee, P. Cicuta, D. Vella, Soft matter **13**, 212 (2017)

[111] J.T. Petkov, N.D. Denkov, K.D. Danov, O.D. Velev, R. Aust, F. Durst, J. Colloid Interface Sci. **172**, 147 (1995)

[112] K.D. Danov, R. Dimova, B. Pouligny, Phys. Fluids **12**, 2711 (2000)

[113] D. Blažek, M. Neslušan, D. Hrabovskỳ, *Surface magnetic domains dynamic in machined steel*, in *EPJ Web Conf.* (EDP Sciences, 2014), Vol. 75, p. 02003

[114] J.D. Jackson, *Classical electrodynamics*, third edition edn. (John Wiley & Sons, Inc., New York, 1999)

[115] A. He, K. Nguyen, S. Mandre, EPL **102**, 38001 (2013)

[116] G. Grosjean, M. Hubert, G. Lagubeau, N. Vandewalle, Phys. Rev. E **94**, 021101 (2016)

[117] L. Zhang, J.J. Abbott, L. Dong, B.E. Kratochvil, D. Bell, B.J. Nelson, Appl. Phys. Lett. **94**, 064107 (2009)

[118] D. Tam, A.E. Hosoi, Phys. Rev. Lett. **98**, 068105 (2007)

[119] S. Childress, S.E. Spagnolie, T. Tokieda, J. Fluid Mech. **669**, 527 (2011)

[120] M. Leoni, J. Kotar, B. Bassetti, P. Cicuta, M.C. Lagomarsino, Soft Matter **5**, 472 (2009)

[121] S. Babel, H. Löwen, A.M. Menzel, EPL **113**, 58003 (2016)

[122] D.J. DeRosier, Cell **93**, 17 (1998)

[123] J.P. Hernandez-Ortiz, C.G. Stoltz, M.D. Graham, Phys. Rev. Lett. **95**, 204501 (2005)

[124] O. Raz, A.M. Leshansky, Phys. Rev. E **77**, 055305 (2008)

[125] L. Zhang, K.E. Peyer, B.J. Nelson, Lab Chip **10**, 2203 (2010)

[126] S. Tottori, L. Zhang, F. Qiu, K.K. Krawczyk, A. Franco-Obregón, B.J. Nelson, Adv. Mater. **24**, 811 (2012)

[127] S. Sengupta, M.E. Ibele, A. Sen, Angew. Chem. Int. Ed. **51**, 8434 (2012)

[128] U.K. Cheang, K. Lee, A.A. Julius, M.J. Kim, Appl. Phys. Lett. **105**, 083705 (2014)

[129] W. Gao, J. Wang, Nanoscale **6**, 10486 (2014)

[130] Y. Ding, F. Qiu, X. Casadevall i Solvas, F.W.Y. Chiu, B.J. Nelson, A. deMello, Micromachines **7**, 25 (2016)

[131] X.L. Wu, A. Libchaber, Phys. Rev. Lett. **84**, 3017 (2000)

[132] M.J. Kim, K.S. Breuer, Phys. Fluids **16**, L78 (2004)

[133] M.J. Kim, K.S. Breuer, Anal. Chem. **79**, 955 (2007)

[134] M.A. Jalali, A. Khoshnood, M.R. Alam, J. Fluid Mech. **779**, 669–683 (2015)

[135] A.J. Giustini, A.A. Petryk, S.M. Cassim, J.A. Tate, I. Baker, P.J. Hoopes, Nano Life **1**, 17 (2010)

[136] M. Sitti, H. Ceylan, W. Hu, J. Giltinan, M. Turan, S. Yim, E. Diller, Proc. IEEE **103**, 205 (2015)

[137] J. Giltinan, E. Diller, C. Mayda, M. Sitti, *Three-dimensional robotic manipulation and transport of micro-scale objects by a magnetically driven capillary micro-gripper*, in *2014 IEEE International Conference on Robotics and Automation (ICRA)* (2014), pp. 2077–2082, ISSN 1050-4729

[138] P. Lambert, *Capillary forces in microassembly: modeling, simulation, experiments, and case study* (Springer Science & Business Media, 2007)

[139] D. Wong, I.B. Liu, E.B. Steager, K.J. Stebe, V. Kumar, *Directed micro assembly of passive particles at fluid interfaces using magnetic robots*, in *2016 International Conference on Manipulation, Automation and Robotics at Small Scales (MARSS)* (2016), pp. 1–6

[140] S.S. Tsai, J.S. Wexler, J. Wan, H.A. Stone, Lab Chip **13**, 119 (2013)

[141] D. Vilela, J. Parmar, Y. Zeng, Y. Zhao, S. Sánchez, Nano Lett. **16**, 2860 (2016)

[142] J.C. Loudet, A.M. Alsayed, J. Zhang, A.G. Yodh, Phys. Rev. Lett. **94**, 018301 (2005)

[143] J.C. Loudet, A.G. Yodh, B. Pouligny, Phys. Rev. Lett. **97**, 018304 (2006)

[144] G.B. Davies, T. Krüger, P.V. Coveney, J. Harting, F. Bresme, Adv. Mater. **26**, 6715 (2014)

[145] E. Diller, Z. Ye, J. Giltinan, M. Sitti, *Addressing of Micro-robot Teams and Non-contact Micro-manipulation* (Springer Berlin Heidelberg, Berlin, Heidelberg, 2014), pp. 28–38, ISBN 978-3-642-55134-5

[146] M. Gera, V.A. Saharan, M. Kataria, V. Kukkar, Recent Pat. Drug Deliv. Formul. **4**, 58 (2010)

[147] F. Qiu, S. Fujita, R. Mhanna, L. Zhang, B.R. Simona, B.J. Nelson, Adv. Funct. Mater. **25**, 1666 (2015)

[148] Z. Lin, J.L. Thiffeault, S. Childress, J. Fluid Mech. **669**, 167–177 (2011)

[149] D.O. Pushkin, J.M. Yeomans, J. Stat. Mech. Theor. Exp. **2014**, P04030 (2014)

[150] L.H. Lu, K.S. Ryu, C. Liu, J. Microelectromech. Syst. **11**, 462 (2002)

[151] G. Grosjean, Y. Collard, M. Hubert, A. Sukhov, J. Harting, A.S. Smith, N. Vandewalle, *Capillary assemblies in a rotating magnetic field*, in preparation (2018)

[152] M. Lighthill, Commun. Pure Appl. Math. **5**, 109 (1952)

[153] J. Blake, J. Fluid Mech. **46**, 199 (1971)

[154] A. Vilfan, F. Jülicher, Phys. Rev. Lett. **96**, 058102 (2006)

[155] T.J. Pedley, D.R. Brumley, R.E. Goldstein, J. Fluid Mech. **798**, 165 (2016)

[156] D. Chan, J. Henry Jr, L. White, J. Colloid Interface Sci. **79**, 410 (1981)

[157] V. Paunov, P. Kralchevsky, N. Denkov, K. Nagayama, J. Colloid Interface Sci. **157**, 100 (1993)

[158] P. Kralchevsky, V. Paunov, I. Ivanov, K. Nagayama, J. Colloid Interface Sci. **151**, 79 (1992)

[159] P.A. Kralchevsky, V.N. Paunov, N.D. Denkov, K. Nagayama, J. Chem. Soc. Faraday Trans. **91**, 3415 (1995)

[160] P. Aussillous, D. Quéré, Nature **411**, 924 (2001)

[161] A. Dinsmore, M.F. Hsu, M. Nikolaides, M. Marquez, A. Bausch, D. Weitz, Science **298**, 1006 (2002)

[162] L. Maquet, P. Colinet, S. Dorbolo, Soft matter **10**, 4061 (2014)

[163] G. Lagubeau, A. Rescaglio, F. Melo, Phys. Rev. E **90**, 030201 (2014)

[164] G. McHale, M. Newton, Soft Matter **11**, 2530 (2015)

A Experimental Protocol

In this appendix, we describe in detail the experimental setup, as well as the conduct of a typical magnetocapillary swimmer experiment. The goal is to allow to reproduce the experiments described throughout this thesis as easily as possible.

A.1 Particles

The metallic spheres used are made of either stainless steel or similar alloys. The first material used was the low alloy steel UNS G52986 (also known as AISI 52100). It was sometimes changed for the stainless steel UNS G42000 (or AISI 420) which has similar properties, but is less prone to rusting. Austenitic stainless steels, like the common 300 series (e.g. AISI 306), should not be used as they are generally non-magnetic. These spheres

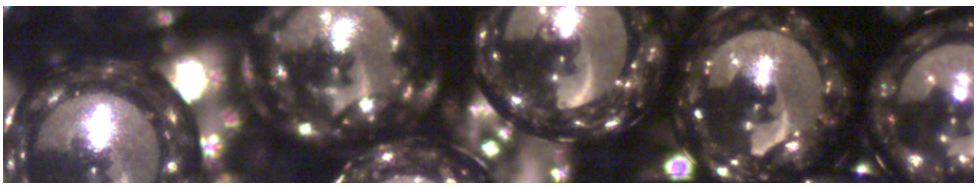

Fig. A.1 Particles. – Microscope view of 500 µm AISI 52100 steel spheres.

are produced industrially and used for example as ball bearings. They are therefore easily available, relatively inexpensive and highly monodisperse. Due to their spherical shape, these particles have a linear magnetisation and an apparent magnetic susceptibility close to 3 (see Fig. 4.2). The standard available diameters are 397 µm (1/64 inch), 500 µm and 793 µm (1/32 inch). Larger particles will simply not float on water.

The particles are manipulated using titanium tweezers, as they are non-magnetic, rigid enough and available with thin tips. However, it can be easier to collect the particles at the end of the experiment using larger tweezers made of plastic or bamboo. With a bit of skill, non-wettable tweezers like these can be used to create a dip on the surface that attracts the particles by Cheerios effect. The opposite effect is also achievable by inclining the tweezers to deflect the interface upwards. This is used to move the particles around on the surface without contact and without perturbing the self-assemblies.

As they are relatively inexpensive, the particles are generally not reused for precision experiments. However, when needed, they can be washed with isopropyl alcohol and then dried on low-lint tissue wipes. An ultrasonic cleaner was also used to remove any sort of contaminant on the surface of the particles. The use of low-lint wipes for any cleaning of the particles, tank and lid is essential, as fibrous residues and dirt floating on the surface tend to aggregate on the assemblies by Cheerios effect.

A.2 Bath

The bath is made of glass and lit from below with an array of LED. It is filled with regular, non-demineralised water. A lid is placed on the bath to prevent any air movement from disturbing the swimmer. The lid is made of glass coated with a transparent conducting oxide to avoid the build up of electric charges.

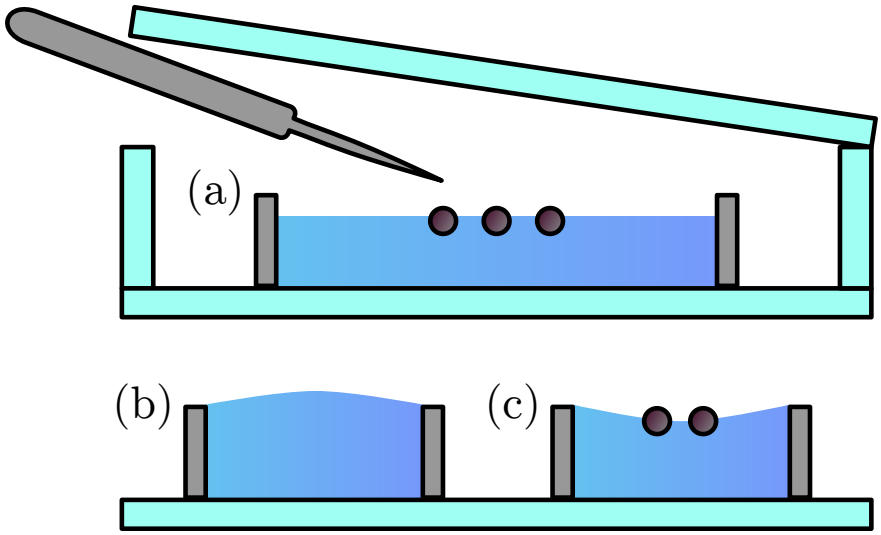

Fig. A.2 Liquid bath. – **(a)** An aluminium ring is placed on a glass plate. A TCO coated glass lid protects the bath. It is removable to allow the manipulation of the particles with titanium tweezers. **(b)** To closely observe the assemblies, a smaller ring is overfilled. **(c)** A bit of water is then removed to create a confining meniscus.

We typically use regular bottled water for the experiments. Not only does it help reduce the effect of electric charges, it also provides a more stable surface tension. Indeed, the surface tension of deionised water is more prone to change with the exposure to contaminants present in the air. Glycerol can be mixed with the water to change the viscosity without affecting much the surface tension, dropping by about 10% for a mixture of 50% water and 50% glycerol in volume. Such mixtures are made a day in advance and continuously stirred on a rotating agitator to assure the mix is homogeneous. Some liquid food dye can also be added for visualisation.

The meniscus of the bath must be as flat as possible, otherwise the particles can drift towards, or away from the sides. To this end, an aluminium ring of about 10 cm in diameter is placed in the bath. The contact angle of water on aluminium is relatively close to 90°, which allows to tune a flat meniscus by carefully filling the bath. The water depth is usually quite

low, typically about 5 mm, to minimise unwanted currents. Figure A.2 (a) illustrates this setup, with the aluminum ring and the glass lid.

A meniscus can also be used to confine the particles. For example, a smaller aluminium ring can be slightly overfilled with water to create a convex meniscus, as shown in Fig. A.2 (b). Some water is then pumped with a syringe to create a concave meniscus as the water stays pinned to the edge of the ring, as shown in Fig. A.2 (c). A similar method can be used between two glass plates, or in a channel that was laser-cut in plexiglass, to create a one-dimensional confinement.

A.3 Coils and Currents

As detailed in Fig. 3.1, three pairs of orthogonal Helmholtz coils are used to generate induction fields in all directions up to 7 mT. The z coils are simply connected to a regulated DC power supply and an ammeter, as the vertical field is usually kept constant in the course of an experiment. The currents in the x and y coils are generated by a dual-channel computer-controlled arbitrary function generator and a pair of amplifiers. The current is monitored with a multi-channel oscilloscope.

The control of the horizontal field is made using a homemade program. The graphical user interface is shown in Fig. A.3. It allows to quickly change the orientation of the oscillation. It is also possible to compensate the influence of the temperature due to the heating of the z coil and frequency response of the system. Some transient behaviours are programmed, such as an oscillation during a finite number of periods, a preparation of the system by temporarily applying a constant field in a given or random direction, and a progressive reorientation of the offset to change the swimming direction. Some useful presets are recorded with typical parameters. The goal of this program is not only to allow some procedures that would be

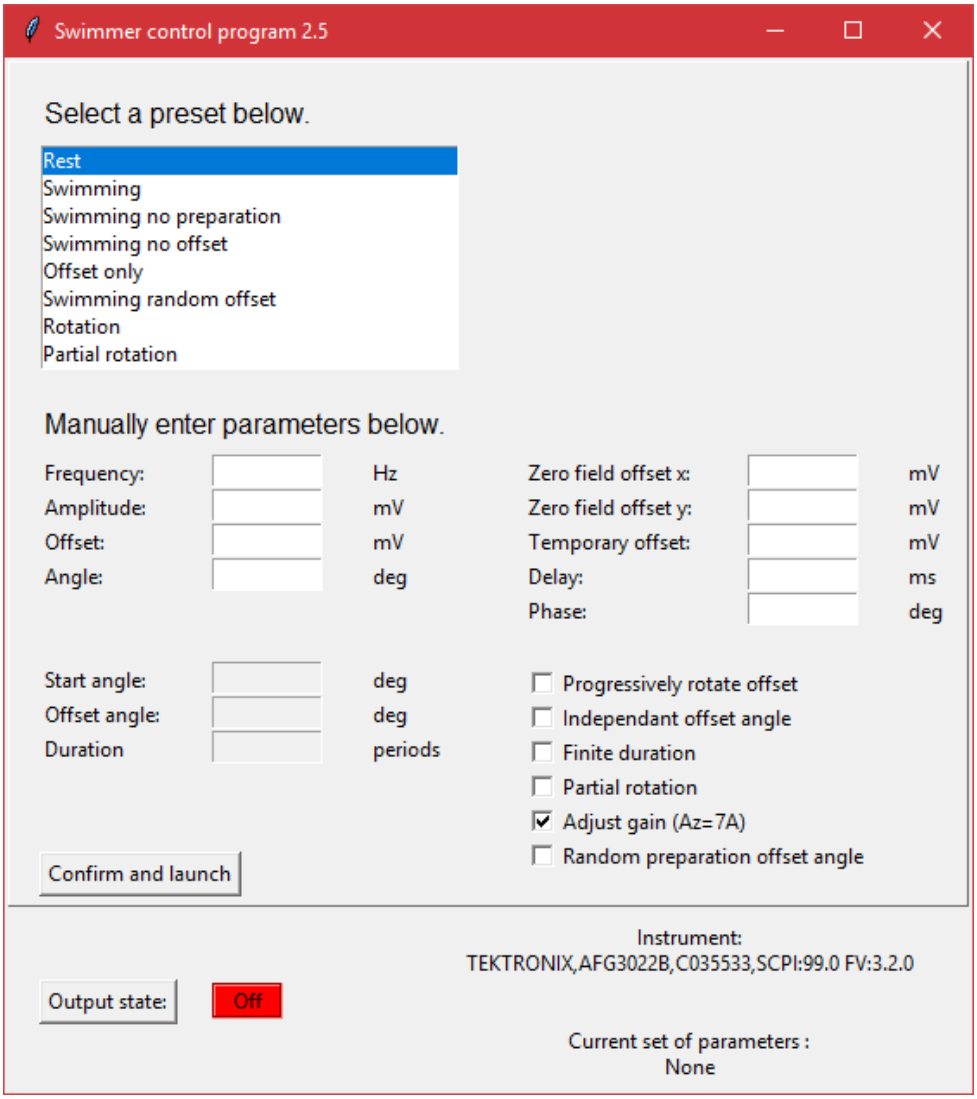

Fig. A.3 Control program. – The graphical user interface of the program that controls the x and y fields.

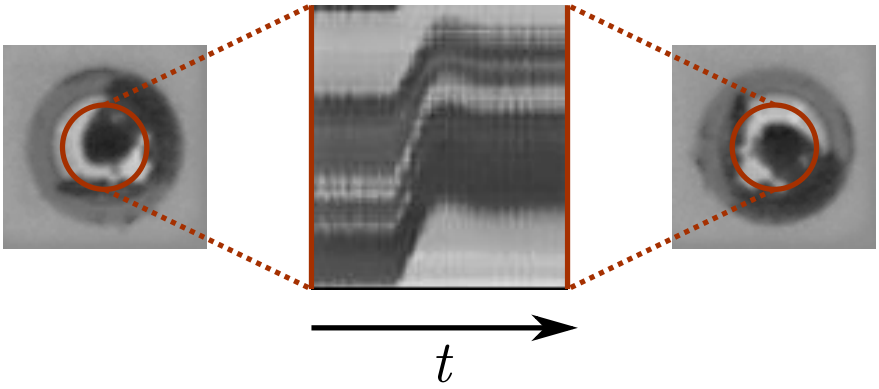

Fig. A.4 Correlation. – The rotation of a single bead is measured by drawing a mark on the particle and following its motion by correlation along several lines of constant radius.

difficult or impossible to perform manually, but to allow students an easy access to the experiment.

A.4 Imaging and Analysis

The particles are filmed from the top with a CCD camera mounted with a close-focusing macro lens (Navitar Zoom 7000). It is a parfocal lens, which stays in focus when the magnification is changed. This allows a lot of flexibility, as the particles can be imaged closely in order to observe the oscillations, or further away to observe the trajectories. The bath is placed on a diffusing sheet above an array of white LEDs. The particles are therefore seen as black on a white background. In regular swimming experiments, however, the particles are tracked using a circle Hough transform, which allows to quite robustly find the position of circular features in an image.

The lighting can of course be changed depending on the situation. For instance, observing the rotation of a single particle, as in Fig. 7.7, requires to carefully light the particles from above. The principle of this measurement is depicted in Fig. A.4. The trajectory of a mark on the particle is followed

by correlation along a family of circles. Therefore, any fixed reflection or spot on the particle could jeopardise the measurement of the rotation.

B Area of a Lissajous Curve

In this appendix, we express the area enclosed in a Lissajous curve of ratio 1 as a function of the amplitudes and the phase shift. This corresponds to a family of ellipses which differ in eccentricity.

Let an elliptical Lissajous curve described by the following system of parametric equations

$$\begin{cases} x' = A_a \sin(\theta) \\ y' = A_b \sin(\theta + \phi) = A_b \left(\sin(\theta)\cos(\phi) + \cos(\theta)\sin(\phi) \right), \end{cases} \tag{B.1}$$

where $\theta = \omega t$ is the parameter, ϕ is the phase difference and A_a, A_b are the amplitudes. We have

$$\begin{cases} \theta = \arcsin\left(\frac{x'}{A_a}\right) \\ y' = A_b \left(\frac{x'}{A_a}\cos(\phi) \pm \sqrt{1 - \left(\frac{x'}{A_a}\right)^2}\ \sin(\phi) \right). \end{cases} \tag{B.2}$$

We will now use the dimensionless variables

$$\begin{cases} x = x' / A_a \\ y = y' / A_b. \end{cases} \tag{B.3}$$

From Eq. (B.2), we have

$$y = x\cos(\phi) \pm \sqrt{1-x^2}\,\sin(\phi), \tag{B.4}$$

which describes two curves in the (x, y) plane. Because the ellipse is unchanged by a rotation of π around the origin, the total enclosed area S is twice the area above the x-axis. Let us consider the case where the foci of the ellipse are in the first and third quadrants. The definite integral of Eq. (B.4) is given by

$$Y_\pm = \int y_\pm \,\mathrm{d}x = \frac{1}{2}\left(\pm\sin(\phi)\left(\sqrt{1-x^2}\,x + \arcsin(x)\right) + x^2\cos(\phi)\right). \tag{B.5}$$

To calculate the area under the curve, we first have to find the roots of Eq. (B.4). One can see that $y = 0$ for $x = -\sin(\phi)$ in the "+" case and for $x = \sin(\phi)$ in the "-" case. Because $\sin(\phi) \leq 1$, with one focus of the ellipse in the first quadrant, we have

$$\begin{aligned} S &= 2\left(\int_{-\sin(\phi)}^{1} y_+ \,\mathrm{d}x - \int_{\sin(\phi)}^{1} y_- \,\mathrm{d}x\right) \\ &= 2\left(Y_+(1) - Y_+(-\sin(\phi)) - Y_-(1) + Y_-(\sin(\phi))\right) \\ &= \frac{\pi}{2}\sin(\phi) + \cos(\phi) + \sin(\phi)\left(\sin(\phi)\cos(\phi) + \phi\right) - \cos(\phi)\sin^2(\phi) \\ &+ \frac{\pi}{2}\sin(\phi) - \cos(\phi) - \sin(\phi)\left(\sin(\phi)\cos(\phi) + \phi\right) + \cos(\phi)\sin^2(\phi) \\ &= \pi\sin(\phi). \end{aligned} \tag{B.6}$$

Finally, in dimensional form, we have

$$S' = \pi A_a A_b \sin(\phi). \tag{B.7}$$